國立臺灣大學生命科學院生化科學研究所

博士論文

Institute of Biochemical Sciences

College of Life Science

National Taiwan University

Doctoral Dissertation

透過金屬離子結合、家族性突變型、以及奈米金粒子瞭解阿茲海默症乙型類澱粉蛋白纖維化的複雜性

Understanding the Complexity of Alzheimer's Disease's Amyloid-β Fibrillization via Metal Ion Binding, Familial Mutants, and Gold Nanoparticles

廖宜鴻

Yi-Hung Liao

指導教授：陳韻如 博士

蔡明道 博士

Advisor: Yun-Ru Chen, Ph.D.

Ming-Daw Tsai, Ph.D

中華民國 103 年 8 月

August 2014

國立臺灣大學（碩）博士學位論文
口試委員會審定書

中文題目：透過金屬離子結合、家族性突變型、以及奈米金粒子瞭解阿茲海默症乙型類澱粉蛋白纖維化的複雜性

英文題目：Understanding the Complexity of Alzheimer's Disease's Amyloid-β Fibrillization via Metal Ion Binding, Familial Mutants, and Gold Nanoparticles

本論文係__廖宜鴻__君（學號_D96B46015_）在國立臺灣大學生化科學所完成之碩（博）士學位論文，於民國 103 年 6 月 18 日承下列考試委員審查通過及口試及格，特此證明

口試委員：

陳韻如（簽名）

（指導教授）

蔡明道　　林俊武

陳佩燁

王勝仕

陳振中

誌謝

感謝多年來我的論文指導老師陳韻如博士的耐心教誨，讓我得以順利再次從物理領域跨到生化科學。陳韻如博士獨立建構起一個至目前頗具規模且研究成果豐碩的實驗室的發展模式也給我對於如何成為一個獨立研究的科學家甚多啟發。

感謝口試時諸位口試委員陳佩燁博士，陳振中博士、林俊成博士、王勝仕博士、蔡明道博士關於實驗的寶貴建議。

人生至此小小里程碑，我要把最大的感恩獻給我的核心家庭，在天國的阿公、阿嬤、爸媽、麗萍、宜駿、美螢、予晨、宜韋、佩君，無論是從小到大給我最大的支持與陪伴，或是人生起落之喜怒哀樂與酸甜苦辣生活體驗的共享，都對於我的人生觀的建構起了無價的積極作用。另外，我的父系與母系大家族的所有成員也對我至目前為止彩色的人生扮演極為重要的角色。我特別想感謝從小到大看我長大的本亮叔叔和我對於人生百態的討論與交流，與雖來不及看我長大，但我相信一直給我保佑的本傑叔叔。我也特別感謝素珍阿姨、素嬌阿姨、素雲阿姨對我從小到大的愛護與像媽媽一樣的各種叮嚀。感謝像親姊般的白雯表姊的陪伴與照顧。感謝我的所有表兄弟姊妹、堂兄弟姊妹的互相扶持與共同的歡樂時光。

感恩在中央物裡認識的好友們，安良、嘉原、景元、政穎、棋蓉，的物理、時事、與天南地北的討論，每每在討論後就有股自己對物理的認知是多渺小的感觸，卻同時也有著激勵自己持續吸收物理知識，以期未來可以應用在生物物理研究的喜悅。

最後，但非最少，的感謝要獻給基因體中心 7L11 的實驗室同仁，在每天的相處中大家的相互照應及學術討論。我敬佩微微學姊和軍宇的研究員精神與投入。感謝天偉在枯燥實驗時還時常帶給大家的歡樂時光和美食的精準推薦。在他粗曠的外表下的纖細內心時常溫暖實驗不順遂的同仁的內心。謝謝常先生的照顧與人生歷練的分享。謝謝婉琤、寧瑄兩位”徒弟”的教學相長。謝謝裕勝對於 3C 產品的專業建議和對電影的感想分享。謝謝明哲和他太太芳智提供的醫療專業建議，感激不盡。感謝博士班學程的同學，弘儒、嘉嘉、信宏、Raja、Winny 的相互打氣。

2014 八月

廖宜鴻

中文摘要

類澱粉蛋白斑塊是許多神經退化性疾病的病徵。斑塊的主要成分是乙型類澱粉蛋白，其纖維化目前被接受是造成阿茲海默症的致病原因。然而，乙型類澱粉蛋白的致病性的調控機制至今仍未有全盤的理解，也未有一致的結論。我們在三個章節中探討三個與乙型類澱粉蛋白有關的主題。第一個主題，我們嘗試了解奈米尺度的金粒子是否影響乙型類澱粉蛋白的纖維化過程及形成此影響的原因。實驗結果顯示未經過表面修飾的裸奈米金粒子能以與劑量呈正相關的方式抑制乙型類澱粉蛋白的纖維化，並造成其形成斷裂的類澱粉蛋白纖維與球型多倍體。我們亦發現裸奈米金粒子偏好附著於纖維而非無定型的堆積。此外，奈米金粒子表面的負電位對於其對乙型類澱粉蛋白纖維化的抑制作用有關鍵性的影響。我們的合作人員亦提供細胞毒性測試結果，顯示經過奈米金粒子抑制後的乙型類澱粉蛋白的最終產物對神經細胞的毒性較低。

第二個主題中，我們欲瞭解與家族性遺傳阿茲海默症有關的 E22 及 D23 單點突變如何影響同源聚合與異源聚合形成之類澱粉蛋白纖維結構。在我們實驗中，同源聚合指的是單一來源的乙型類澱粉蛋白經培養後形成之纖維，而異源聚合則是混合同濃度之兩種不同乙型類澱粉蛋白 (原生型與突變型) 再經培養後形成的類澱粉蛋白纖維。實驗結果發現同源聚合纖維在蛋白質二級結構上與異源聚合纖維有顯著的不同。而此二集結構上的相異並未反應在類澱粉蛋白纖維螢光探測分子 Thioflavin T 與纖維結合的反應計量上。然而，透過 ThT 與類澱粉蛋白纖維結合後

的螢光壽命的測量卻可以得知此參數可能能夠反應纖維結構的異同。我們尚在進行更多相關的實驗以佐證目前實驗結果的初步結論。

我們在最後一個主題探討過渡型金屬離子，特別是二價銅離子與鋅離子，與乙型類澱粉蛋白的交互作用細節及另幾類家族性遺傳相關的 H6 及 D7 單點突變如何影響這交互作用。首先我們提供鋅、銅、鐵、鋁離子與原生型乙型類澱粉蛋白的豪秒級結合動力學，結果顯示這四種金屬離子與乙型類澱粉蛋白結合的速度有顯著差異。接著我們專注於另一類家族性遺傳阿茲海默症變異型 H6 和 D7 對於銅離子與乙型類澱粉蛋白結合的影響。實驗結果顯示，除了 D7A 和 H6R 外，銅離子結合伴隨著表面疏水性區域的減少。核磁共振實驗結果表明在未加金屬離子前，變異型與原生型乙型類澱粉蛋白在芳香族支鏈光譜區域，特別是 H6， H13/H14，和 Y10，有些微差異。銅離子結合而導致的光譜消失在 D7H 變異型中較為不顯著。^{1}H-^{15}N 異核核磁共振光譜顯示銅離子與 D7H 和原生型乙型類澱粉蛋白結合的相異之處。

Abstract

Amyloid plagues are the major pathogenic hallmarks in many neurodegenerative diseases. Fibrillization of the primary constituents, amyloid-β (Aβ), in plagues is considered the pathogenesis of Alzheimer's disease (AD). Conclusive evidence is still lacking to reach a comprehensive and convergent view of how Aβ is modulated in the pathogenesis of AD. Here, in three separate chapters, we examined how gold nanoparticles (AuNPs) interfere with fibrillization of Aβ, the effects of single-point N-terminal mutation, H6 and D7, on the interactions between metal ions and Aβ, and how single-point mutations, E22 and D23, influence the structures of fibril.

In Chapter 3, experimental results showed that (1) bare AuNPs inhibited Aβ fibrillization in a dose-dependent manner and redirected Aβ forming fragmented fibrils and spherical oligomers; (2) bare AuNPs bound preferentially to Aβ fibrils but not amorphous aggregates; (3) negative surface potential of AuNPs was required for inhibitive effect. In conjunction with our *in vitro* biophysical and biochemical data, cell studies from our lab member revealed that in our experimental settings, inhibition of Aβ fibrillization by negatively charged AuNPs also reduce Aβ-induced cytotoxicity in neuronal cells.

In Chapter 4, we aimed to reveal distinctions among structures of homopolymeric fibrils (homo-fibrils) formed from incubation of monomers of a single species, and heteropolymeric ones (hetero-fibrils) started from incubation of equal-molar-mixed monomers of wild type and an Aβ variant. We showed that E22 hetero-fibrils are distinct from E22 homo-fibrils in terms of secondary structures. Perturbed secondary structure could influence conformational packing of cross β-sheet, which were not revealed by stoichiometry between Aβ and ThT but by ThT fluorescence lifetime.

In Chapter 5, we investigated millisecond binding kinetics of four metal ions, Zn^{2+}, Cu^{2+}, Fe^{3+}, and Al^{3+}. We then focused on Cu^{2+} and demonstrated that mutation at residues H6 and D7 impact on Cu^{2+} binding affinities. We found by Bis-ANS fluorescence that diminished hydrophobic exposure was accompanied by Cu^{2+} binding except for D7A and H6R. Our preliminary proton NMR showed that there existed environmental variance surrounding residues H6, H13/H14, and Y10 among monomeric Aβ variants in native condition. Cu^{2+}-binding-induced peak loss was less evident in D7 mutants. ^{1}H-^{15}N NMR HSQC spectroscopy provided additional information regarding the residual involvement on Cu^{2+} binding between D7H and wild type Aβ.

Abbreviations

The single-letter and three-letter standard amino acid codes are used to designate amino acid residues.

Aβ	Amyloid-β peptide
Aβ40	Amyloid-β(1-40) peptide
Aβ42	Amyloid-β(1-42) peptide
AD	Alzheimer's disease
AFM	Atomic force microscopy
AICD	APP intracellular domain
Al	Aliminum
APP	Amyloid precursor protein
AuNPs	Gold nanoparticles
CD	Circular dichroism
Cu	Copper
Cu^{2+}	Copper ion with valence of two electrons
DMSO	Dimethyl sulfoxide
FAD	Familial Alzheimer's disease
Fe	Iron
FTIR	Fourier transform infrared
F-moc	N-(9-fluorenyl)methoxycarbony
GdnHCl	Guanidine hydrochloride
GSAP	γ-secretase activating protein
HFIP	Hexafluoro-2-propanol
HSQC	Heteronuclear single quantum coherence
M	Molar
mg	Milligram
mL	Milliliter
mm	Millimeters
mM	Millimolar
min	Minute
ms	Millisecond
NaOH	Sodium hydroxide
NCT	Nicastrin
nm	Nanometer

nM	Nanomolar
l	Path length (in cm)
PEG-*b*-PLA	poly(ethylene glycol)methyl ether-block-polylactide
ppm	Parts per million
pM	Picomolar
UV	Ultraviolet
UV/Vis	Ultraviolet/Visible
μL	Microliter
μM	Micromolar
Zn	Zinc
Zn^{2+}	Zinc ion with valence of two electrons

Table of Contents

口試委員會審定書 i

誌謝..... ii

中文摘要..... iv

Abstract..... vi

Abbreviations viii

Table of Contents.....x

List of Figures..... xiv

List of Tables xviii

Chapter 1 Introduction 1

1.1 Alzheimer's disease.....1

1.1.1 Overview 1

1.1.2 Risk factors and treatments 3

1.1.3 Hypotheses of the pathogenesis of Alzheimer's Disease 4

1.2 Amyloid-β 5

1.2.1 Amyloid-β monomer 8

1.2.2 Amyloid-β fibrils.....9

1.3 Amyloid-β and metal ions 11

1.4 Single-point mutations of Amyloid-β.....13

1.4.1 Familial mutations, A21, E22, and D23, in Alzheimer's disease.....13

1.4.2 N-terminal familial mutations, H6 and D7, in Alzheimer's disease 15

1.5 Application of nanotechnology in the studies of Alzheimer's disease.....16

Chapter 2 Materials and methods.....18

2.1 Materials.....18

2.2 Methods.....18

2.2.1 Aβ monomer preparation 18

2.2.2 AuNPs preparation 20

2.2.3 Thioflavin T assay 21

2.2.4 Dynamic light scattering 21

2.2.5 Transmission electron microscopy 22

2.2.6 Fourier transform infrared spectroscopy 22

2.2.7 Far-UV circular dichroism spectroscopy.....23

2.2.8 Fluorescence lifetime measurement 23

2.2.9 Stopped-flow fluorescence 24

2.2.10 Fluorescence spectroscopy 25

2.2.11 Proton and ^{1}H-^{15}N HSQC NMR spectroscopy.....25

Chapter 3 Interference of gold nanoparticles in the fibrillization process of wild type Aβ40..... 27

3.1 Aims 27

3.2 Bare AuNPs inhibit Aβ fibrillization without self-clustering.....28

3.3 Bare AuNPs alter ThT fluorescence intensity of preformed Aβ fibrils.....31

3.4 Absorbance spectra of Aβ monomers or preformed Aβ fibrils 33

3.5 DLS analysis shows redirected Aβ species in the presence of AuNPs.....35

3.6 Bare AuNPs induce Aβ fibril fragmentation and oligomer formation and preferentially bind to Aβ fibrils 37

3.7 Negatively charged AuNPs inhibit Aβ fibrillization in vitro.....40

Chapter 4 Structural differences between homo-polymeric and hetero-polymeric Aβ fibrils.....43

4.1 Aims 43

4.2 Homo- and hetero- fibrils are morphologically indistinguishable under TEM imaging. 44

4.3 Binding stoichiometry of Thioflavin T to amyloid-β fibrils 46

4.4 Secondary structures of fibrils revealed by far-UV circular dichroism 48

4.5 Secondary structures of fibrils revealed by Fourier transformation infrared spectroscopy 52

4.6 Fluorescence lifetime of bound ThT on fibrils.....57

Chapter 5 Interactions of Cu^{2+} with wild type and N-terminal familial mutants of Aβ 62

5.1 Aims 62

5.2 Metal ion binding examined by stopped-flow fluorescence. 62

5.3 Intrinsic fluorescence of H6 and D7 mutants upon Cu^{2+} binding 65

5.4 Bis-ANS fluorescence of H6 and D7 mutants upon Cu^{2+} binding.....68

5.5 ^{1}H NMR spectroscopy.....72

5.6 ^{1}H-^{15}N HSQC spectroscopy of D7H and wild type Aβ.....78

Chapter 6 Discussion.....84

6.1 Negatively Charged Gold Nanoparticles Inhibit Alzheimer's Amyloid-β Fibrillization, Induce Fibril Dissociation, and Mitigate Neurotoxicity.....84

6.1.1 Results of various effects imposed by AuNPs on Aβ.....84

6.1.2 Inhibition of Aβ fibrillization by nanoparticles.....87

6.1.3 Effect of localized charge on Aβ fibrillization.....88

6.2 Homo- and hetero- polymeric Aβ fibrils.....91

6.3 Cu^{2+} coordination of H6 and D7 mutants of Aβ.....92

6.3.1 Effect of H6 mutation on Cu^{2+} binding to Aβ.....94

6.3.2 Effect of D7 mutation on Cu^{2+} binding to Aβ.....95

Reference.....97

Supplementary data.....108

List of Figures

Figure 1. Estimated growth of dementia in the world. 2

Figure 2. Schematic of APP processing. 6

Figure 3. Structural characteristics of Aβ monomer. 9

Figure 4. Schematic illustration of amyloid fibril formation via nucleation-dependent mechanism. 10

Figure 5. Three-dimensional structural model of Aβ40 fibrils. 10

Figure 6. Coordination structure of Cu^{2+}-Aβ complex. 13

Figure 7. Mutation sites located inside and outside Aβ sequence.. 14

Figure 8. Absorption spectrum of 30 nm AuNPs. 29

Figure 9. Time course of ThT fluorescence changes of Aβ monomers incubated with and without 30 nm AuNPs. 30

Figure 10. Time course of ThT fluorescence changes of preformed Aβ fibril incubated with and without bare AuNPs. 32

Figure 11. Time course absorbance spectra of Aβ monomers or preformed Aβ fibrils incubated in the presence of 1.36 nM AuNPs. 34

Figure 12. DLS analysis of size distribution of the Aβ species induced by AuNPs. 36

Figure 13. TEM images of co-incubated monomeric Aβ and bare AuNPs, and co-incubated Aβ fibrils.. 39

Figure 14. Fibrillization kinetics of Aβ in the absence and prescence of 1.36 nM bare, amine-, and carboxyl- conjugated AuNPs recorded by ThT assays.. 41

Figure 15. TEM images of the 160 h-incubated Aβ in presence of 1.36 nM AuNPs. 42

Figure 16. TEM images of homo- and hetero- fibrils of E22G, E22K, E22Q, and D23N. 45

Figure 17. ThT binding stoichiometry of (a) homo-and (b) hetero- fibrils. 47

Figure 18. CD spectra of homo-fibrils. 48

Figure 19. CD spectra of each FAD homo-fibrils, hetero-fibrils, and equal-molar-mixed homo-fibrils. 51

Figure 20. FTIR spectra of homo-fibrils. 53

Figure 21. FTIR spectra of FAD homo-fibrils, hetero-fibrils,and equal-molar-mixed homo-fibrils. 56

Figure 22. Comparison of ThT fluorescence lifetime for FAD homo-fibrils. 59

Figure 23. Comparison of ThT fluorescence lifetime for FAD hetero-fibrils. 60

Figure 24. Binding kinetics of Zn^{2+}, Cu^{2+}, Fe^{3+}, and Al^{3+} with Aβ40.. 63

Figure 25. Tyrosine emission spectra of wild type, H6, and D7 mutant Aβ..... 66

Figure 26. Cu^{2+} titration curves of wild type, H6, and D7 variants of Aβ monitored by tyrosine fluorescence. 68

Figure 27. Bis-ANS emission spectra of wild type, H6, and D7 mutant Aβ.. 69

Figure 28. Cu^{2+} titration curves of Aβ monitored by BisANS fluorescence.. 71

Figure 29. Aromatic region in the ^{1}H NMR spectra of wild type Aβ40. 73

Figure 30. Comparison of ^{1}H NMR spectra of wild type Aβ and its H6 and D7 variants in the absence of Cu^{2+}.. 75

Figure 31. Peak broadening around aromatic region during Cu^{2+} titration of wild type Aβ40. 76

Figure 32. Reduction of H6 and H13/H14, δH peaks, and Y10 peaks for H6 and D7 variants of Aβ.. 77

Figure 33. Comparison of ^{1}H-^{15}N HSQC NMR spectrum from Zagorski's and our group. 78

Figure 34. Comparison of ^{1}H-^{15}N HSQC spectra from wild type and D7H Aβ..... 80

Figure 35. ^{1}H-^{15}N HSQC spectra of peptide in the presence of one molar equivalent Cu^{2+}.

..... 81

Figure 36. ^{1}H-^{15}N HSQC spectra of peptide in the presence of two molar equivalent Cu^{2+}.

..... 82

Figure 37. Relative NH peak intensities obtained from ^{1}H-^{15}N HSQC spectra with different amounts of Cu^{2+}.. 83

Figure 38. Diagram of Aβ fibrillization pathways influenced by AuNPs..... 86

List of Tables

Table 1. Summary of lifetimes of ThT upon binding to amyloid fibrils.....59

Table 2. Summary of dissociation constants Kd extracted from curve fitting of data from intrinsic tyrosine and Bis-ANS fluorescence.....69

Chapter 1 Introduction

1.1 Alzheimer's disease

1.1.1 Overview

German psychiatrist and neuropathologist, Dr. Aloysius "Alois" Alzheimer, was the first, in 1906, to present the pathology and the clinical symptoms of presenile dementia observed on a 51-year-old female patient Mrs. Auguste Deter[1]. The latest statistics and facts assessed by "The Alzheimer's Association" revealed that dementia, of which Alzheimer's disease (AD) accounts for 60 % - 80 %, influences at least 44 million people worldwide in 2013[2]. Figure 1 shows an estimate growth of dementia in the world made back in 2009[3]. Approximately 500 thousands of people die of AD each year. Sixty percent of this number is estimated to be contributed from Asia, and the prevalence around the globe is estimated to triple by 2050[4]. Early common symptoms shared by dementia are progressive memory loss, difficulties in undertaking familiar tasks and using language, cognitive deterioration, and deprivation of physical capability. These mental declinations gradually erode physical integrity and ultimately claim millions of lives yearly[5]. According to the *2014 Alzheimer's Disease Facts and Figures*[6] published by the Alzheimer's Association, in addition to the escalating prevalence and mortality, in United States, social costs on caregivers to maintain quality care to the 5 million people with dementia are 17.7 billion hours of unpaid care from 15.5 million of healthy family

members or friends in 2013. The same report also estimated that, economically, an 214 billion U.S. dollars have to be spent in taking care of people with AD. The figure is forecasted to reach 1.2 trillion by 2050. Despite that scientific efforts to elucidate the mechanism of AD have gained significant progress, AD is still incurable. Fighting against AD and other dementia is of paramount importance to reverse not only the disease-developing course on patients but the exploding social and economic costs on related neurodegenerative diseases.

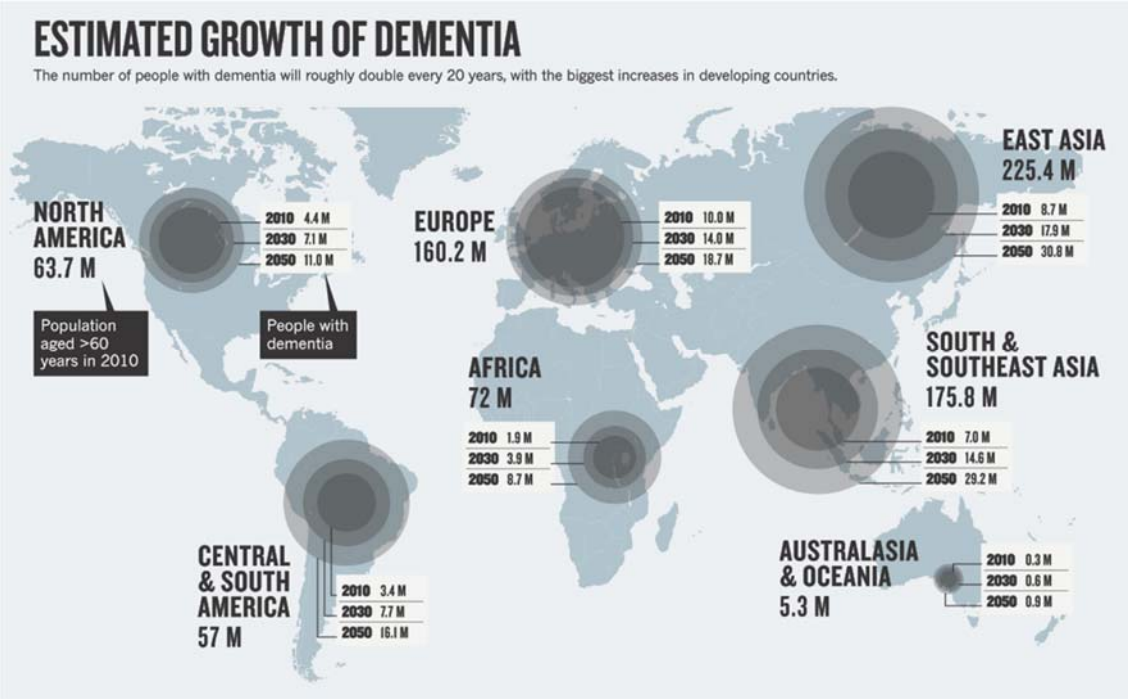

Figure 1. Estimated growth of dementia in the world. Adapted from ref. 3.

1.1.2 Risk factors and treatments

A wide spectrum of risk factors such as aging[7], genetic mutation[8], brain trauma caused by head injury[9], dysregulation of lipid and insulin metabolism[10–14], and exposure to heavy metals[15–18] were investigated and are considered to increase chances to cause AD. Pathological hallmarks of AD include extracellular brain deposits called senile plagues which are enriched in amyloid fibrils and neurofibrillary tangles (NFTs) made of hyper-phosphorylated tau protein[15], and neuropil threads[15,19,20]. To date, several drug targeting have been marketed and administered to alleviate symptoms of mild-to-moderate drugs that target NMDA receptor to restore homeostasis of glutamatergic systems or acetylcholinesterase to enhance production of acetylcholine in dysfunctional neurons aim to improve learning and memory[21]. There are also drugs aimed to relieve depression or aggression. Treatments that have proceeded into at least phase II trial and have promising results are immunotherapy[22,23], metal chelator treatment[24–26], and Tau aggregation inhibitors[27,28]. Nevertheless, present treatments are not satisfactory in that progression of the disease is delayed, not halted[20].

1.1.3 Hypotheses of the pathogenesis of Alzheimer's Disease

Pathogenesis of AD is still a matter of debate. However, importance of amyloid is shared among the two major competing pathogenic hypotheses. Amyloids are a group of proteins capable of aggregating into fibrils characterized by cross-β sheets. Amyloid fibrils can be identified by x-ray diffraction[29], Congo red birefringence using polarized light[30], and external fluorescent probe thioflavin T (ThT)[31]. Amyloid fibrils have been found to be common signatures in many neurodegenerative diseases including Alzheimer's (AD), Parkinson's (PD), and Huntington's diseases (HD)[32]. The earliest proposed hypothesis[33] was based on the evidence that dysregulated metabolism of amyloid precursor protein (APP) leads to a cascade of downstream reactions, developing into abnormally high level of Aβ production and resulting in deleterious Aβ fibrils deposits found in central nervous system (CNS) of AD patients. The second pathogenic hypothesis shifted focus to the dyshomeostasis of redox-reactive metal ions such as Zn^{2+}, Cu^{2+}, and Fe^{3+} [34]. The model was based mainly on the post-mortem analysis showing that concentration of several ions increased in senile plagues and neuropils of AD patients[34–36]. More recently, hypotheses such as two-hit and presenilin model were proposed to explain AD pathogenesis from different perspectives. The two-hit model hypothesizes that that concomitant occurrence of oxidative stress and abnormal mitotic alterations

leads to AD[37,38]. Presenilin model proposes that lost function of transmembrane protein presenilin triggers pathogenesis of AD[39].

1.2 Amyloid-β

The corresponding amyloid proteins in AD is amyloid-β (Aβ). Aβ are proteolytic products after sequential cleavages of β- and γ- secretases[40] on amyloid precursor protein (APP)[40–42] in the amyloidogenic pathway. To be specific, APP is first cleaved by β-secretase, producing soluble fragment sAPPβ in the extracellular space and a carboxy-terminal fragment CTFβ. Subsequent processing on CTFβ by γ-secretase complex generates APP intracellular domain (AICD) and Aβ. The γ-secretase is a protein complex composed of presenilin, nicastrin (NCT), γ-secretase activating protein (GSAP), and multipass transmembrane proteins encoded by pen-2, and aph-1 genes[42,43]. The other pathway is a non-amyloidogenic pathway in which α-secretase cleaves APP in its extracellular domain to release a soluble fragment sAPPα and a carboxy-terminal fragments CTFα (Figure 2).

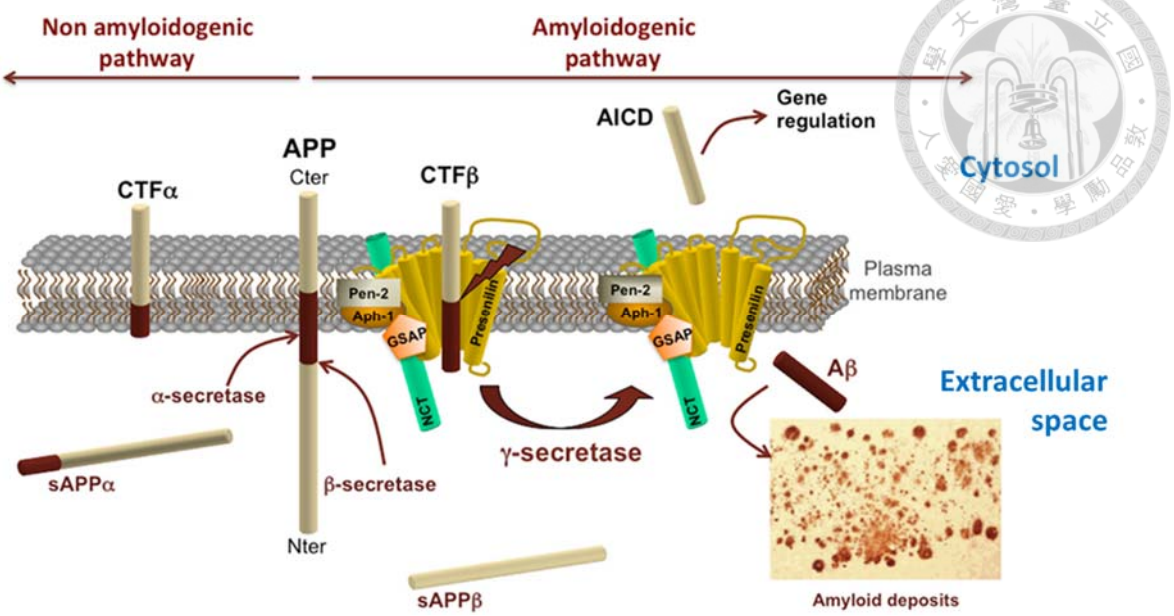

Figure 2. Schematic of APP processing. Adapted from ref. 42. APP processing can undergo either the non-amyloidogenic pathway (left) or the amyloidogenic pathway (right). In the non-amyloidogenic pathway, α-secretase cleaves APP in its extracellular domain to release a soluble fragment sAPPα and a carboxy-terminal fragments CTFα. In the non-amyloidogenic pathway, β- and γ- secretases sequentially cleave APP. The resulting products are sAPPβ in the extracellular space and a carboxy-terminal fragments CTFβ. Subsequent processing on CTFβ by γ-secretase complex generates AICD and Aβ. The γ-secretase is a protein complex composed of presenilin, nicastrin (NCT), γ-secretase activating protein (GSAP), pen-2, and aph-1 .

Predominant Aβ species are isoforms Aβ40 and Aβ42 which respectively consists of 40 and 42 amino-acid residues with the latter bearing identical sequence as the former except for the extra two residues at the C-terminus. Aβ40 is 10 times more abundant than Aβ42, but Aβ42 aggregates faster and plays a more evil role[44–47]. Aβ is a intrinsically disordered and is prone to aggregating into fibrillar structures characterized by cross-β

sheets[48]. Structural modeling shows that the cross β-sheet stacks along the axis of fibril[49]. For long time Aβ fibrils were regarded as a direct cause of neuronal death, and the amyloid aggregation of Aβ at the extracellular space has been implicated in the pathogenesis of AD. In recent years, however, accumulating evidences demonstrate that specific intermediates, i.e. Aβ oligomers, in Aβ fibrillization contribute majorly to the neurotoxicity and correlate best with the cognitive impairment and synaptic dysfunction[50]. Ratio of Aβ40 and Aβ42 has been implicated to alter population of various Aβ species, which are correlated with cytotoxicity to neurons[51]. Several oligomeric species have been reported including Aβ dimers/trimers[52], spherical oligomers[53], Aβ-derived diffusible ligands (ADDLs)[54], globulomers[55,56], annular protofibrils[57], Aβ56*[58], and curvilinear protofibrils[59]. On the other hand, Aβ fibrils are relatively less toxic[60], but different types of fibrils have been shown to cause various toxicities[61]. The structure-neurotoxicity relationships and the importance of structure-function relationships in protein sciences necessitate the detailed structural determination of all forms of Aβ.

1.2.1 Amyloid-β monomer

Aβ monomer is a natively unfolded or intrinsically disordered protein lacking intact secondary and tertiary structures[48] (

Figure 3). Biochemical properties from solution NMR, limited proteolysis/mass spectrometry, fluorescence spectroscopic investigations indicated that the N-terminus (residues 1-28) is hydrophilic[62], the central protease-resistant (residues 20-30) segment harboring turn/bend-like structure is flanked by two β-strands (residues 17–21 and 31–36), and the C-terminus (residues 29-40 for Aβ40 and 29-42 for Aβ42) is hydrophobic[63–66]. The turn/bend-like structure is stabilized by hydrophobic interactions between side chains of V24 and L28, and by long-range electrostatic interactions between L28 and E22 or D23[66]. Higher conformational stability of the central turn/bend region is correlated with higher propensity oligomerization[67]. In addition, the protease-resistant segment covers residues E22 and D23 that are implicated to serve as a nucleation site for Aβ monomer folding[66].

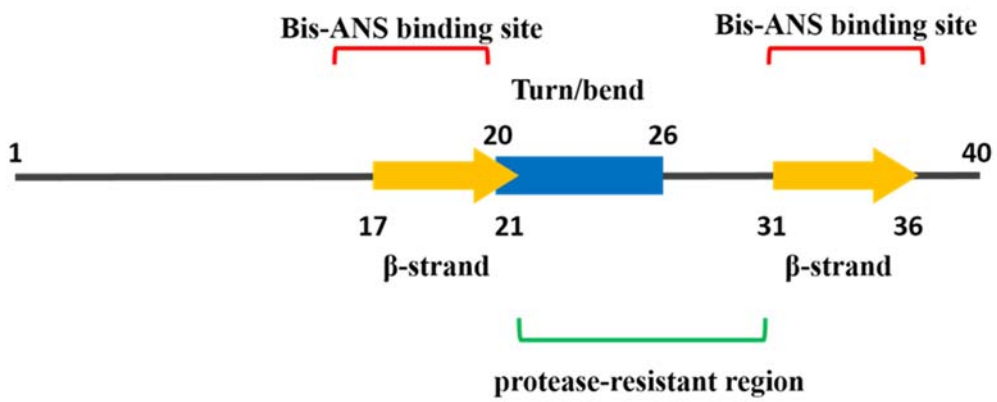

Figure 3. Structural characteristics of Aβ monomer.

1.2.2 Amyloid-β fibrils

Monomeric Aβ molecules were proposed to polymerize into oligomers that serve as nuclei for subsequent elongation into fibrils via a nucleation-dependent polymerization mechanism[68,69] (Figure 4). Three-dimensional structures of Aβ fibrils have been obtained by solid state NMR spectroscopy[49,61,70,71]. Figure 5 shows a three-dimensional structural model of a five-stacking-β-sheets segment of one Aβ40 fibril proposed by Petkova et al. in 2002[49]. They discovered that in a single monomer in Aβ40 fibrils the N-terminus containing the first 10 residues is structurally disordered, the two β-strands in residues 12–24 and 30–40 form two in-register parallel β-sheets through intermolecular hydrogen bonding between side chains on each side of the β-sheets in contact, a bend in residues 25–29 that bring the two β-sheets in contact, and an intramolecular salt bridge formed between side chains of D23 and K28[49].

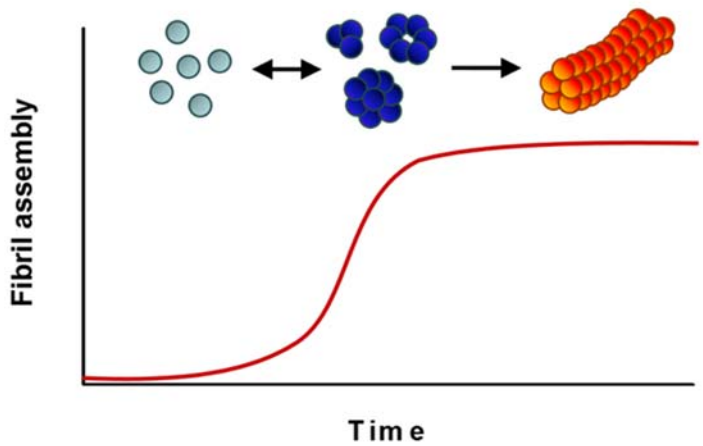

Figure 4. Schematic illustration of amyloid fibril formation via nucleation-dependent mechanism.

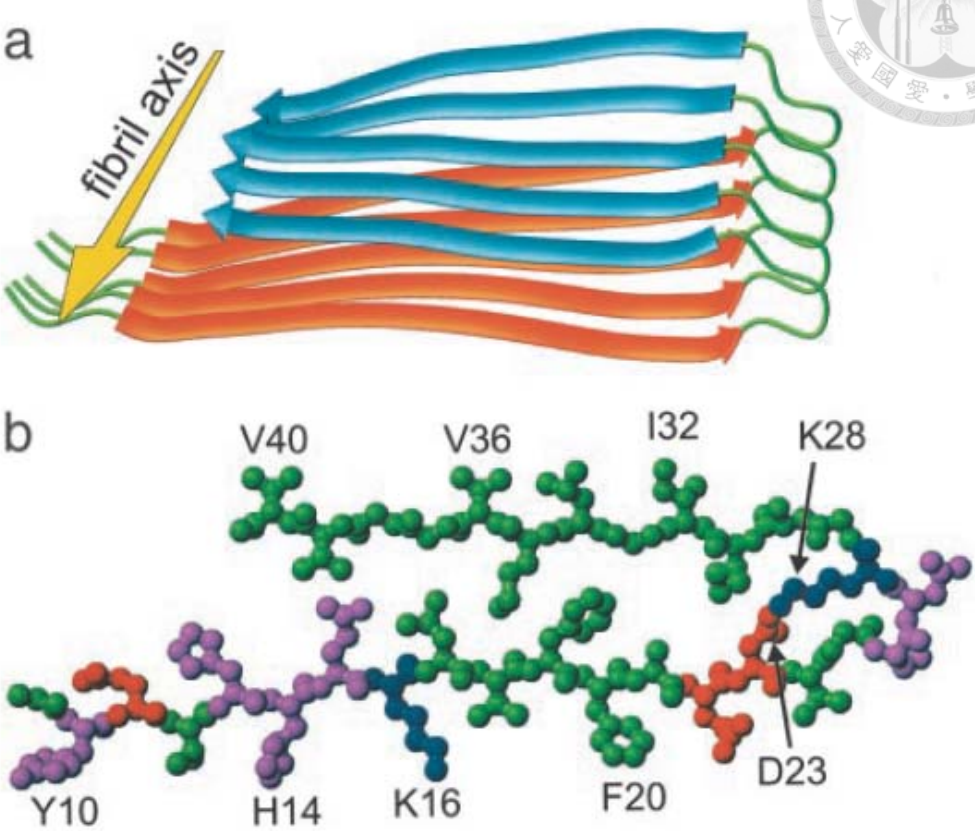

Figure 5. Three-dimensional structural model of Aβ40 fibrils. Adapted from ref. 49. (a) Schematic representation of a single layer of cross-β unit extended along the direction of fibril axis (yellow arrow). The β-strands formed at residues 12–24 are depicted as orange ribbons. The β-strands formed at residues 30-40 are depicted as blue ribbons. (b) The 10-40 segment of Aβ viewed down the long axis of the fibril. Residues are colored according to the properties of the side chains. Residues with hydrophobic side chains are in green, polar ones are in magenta, positive ones are in blue, and negative ones are in red.

In 2005, another work by Petkova et al. using scanning transmission electron microscopy (STEM) and solid state NMR spectroscopy refined the model and revealed

that the structural variations in molecular level lead to distinct fibrillar morphologies[61]. Robert Tycko concluded in a review paper that the following similarities between Aβ40 fibrils prepared in quiescence and by gentle agitation exist[71]. First, residues 1–9 are structurally disordered. Secondly, residues 10–22 and 30–40 form two β-strands flanking a bend/loop in residues 23–29[71]. The β-strands form an extending in-register, parallel β-sheets via intermolecular hydrogen bonds within the β-sheets[71]. In their 2005 and 2006 publications, Petkova et al. determined from isotope dilution experiments that the β-sheets are staggered, creating intermolecular rather than intramolecular contacts between neighboring β-sheets[61,72]. In addition to Tycko's group, staggered contacts suggesting intermolecular salt bridges between D23 and K28 in cross β-sheets were also found in Aβ42 fibrils[70].

1.3 Amyloid-β and metal ions

Homeostasis of physiologically vital metal ions is critical in maintaining normal neurotransmission[73]. Lowell et al. reported a comprehensive comparison showing that Fe^{3+}, Zn^{2+}, and Cu^{2+} are at least twice as much concentrated in AD neuropils as in control (healthy) neuropils[74]. The difference is further widened to at least threefold when the AD-specific senile plagues were compared with normal neuropils. Redox-active capability of

Fe^{3+} and Cu^{2+} has been shown to elevate production of H_2O_2 and in turn to aggravate oxidative stress by forming metal-Aβ complex[15,75].

Investigations at molecular level demonstrated that all three metal ions mentioned above are capable of binding Aβ peptide[18,20,76]. Zn^{2+} and Cu^{2+} ions accelerate Aβ aggregation into amorphous deposits[23,24]. Fe^{3+} and exogenous Aluminum (Al^{3+}) promote Aβ oligomerization and fibrillization[25,26]. While the binding affinity determined from various *in vitro* studies was discrepant and is still inconclusive, the coordination of metal-Aβ complex is accepted with more consensus. Results from X-ray absorption spectroscopy (XAS)[77] and electron paramagnetic resonance (EPR; also known as electron spin resonance, ESR)[78,79] studies agreed that intramolecular H6, H13, and H14 are involved in forming Cu^{2+}-Aβ complex. EPR studies further implicated that the N-terminal amine nitrogen from Asp-1 (D1) and the carbonyl oxygen from Ala-2 (A2) are involved in the formation of Cu^{2+}-Aβ complex[80] (Figure 6), suggestive of an important role of N-terminal Aβ in AD pathology. It was reported that intermolecular Cu^{2+}-Aβ complexes can be formed via histidine bridges[81]. Similar but more complex coordination scenarios involving different numbers of histidine, intra- and inter- molecular binding modes, and possible binding partners at the N-terminus or E11 were reported for Zn-Aβ complex[82–85]. For iron, ^{1}H NMR titration study showed strong binding between Fe and histidine residues[86].

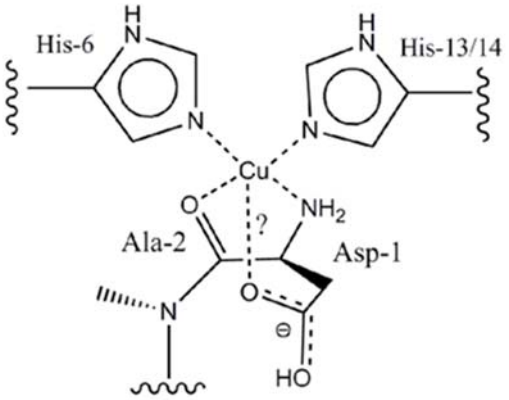

Figure 6. Coordination structure of Cu^{2+}-Aβ complex. Adapted from ref. 20. This is the most plausible Cu^{2+} coordination. It involves a nitrogen from H6, a nitrogen from either H13 or H14, the N-terminal amine nitrogen from D1, and the carbonyl oxygen from A2. The question mark denotes a weakly bound carboxylate from the side chain of D1 is possible.

1.4 Single-point mutations of Amyloid-β

1.4.1 Familial mutations, A21, E22, and D23, in Alzheimer's disease

Despite that familial mutation cases comprise around 10 % compared to sporadic cases[87], evidence that these point mutations can drastically alter the fibrillization kinetics and properties of Aβ inspired effort to gain insight of the underlying mechanism[88]. Point mutations may occur both outside and inside Aβ sequences as shown in Figure 7. Point mutations can lead to total Aβ production, alteration in biophysical properties, or population change in oligomeric species. Of all the mutants studied, mutation at A21, E22,

and D23 drew relatively more attention due to locations at the protease-resistant segment related to nucleation process. A comparative biochemical study on FAD mutants A21G (Flemish), E22G (Arctic), E22K (Italian), E22Q (Dutch), and D23N (Iowa), which cause early-onset AD, showed that all except A21G fibrillized faster than wild type Aβ, and all five mutants adopt the same two-state equilibrium folding mechanism as wild type Aβ does, and that E22 mutants are relatively unstable[65]. Computer simulation results suggest that folding stability was correlated with disturbance in fibrillization kinetics and this phenomenon was attributed to decreased free energy level[89,90].

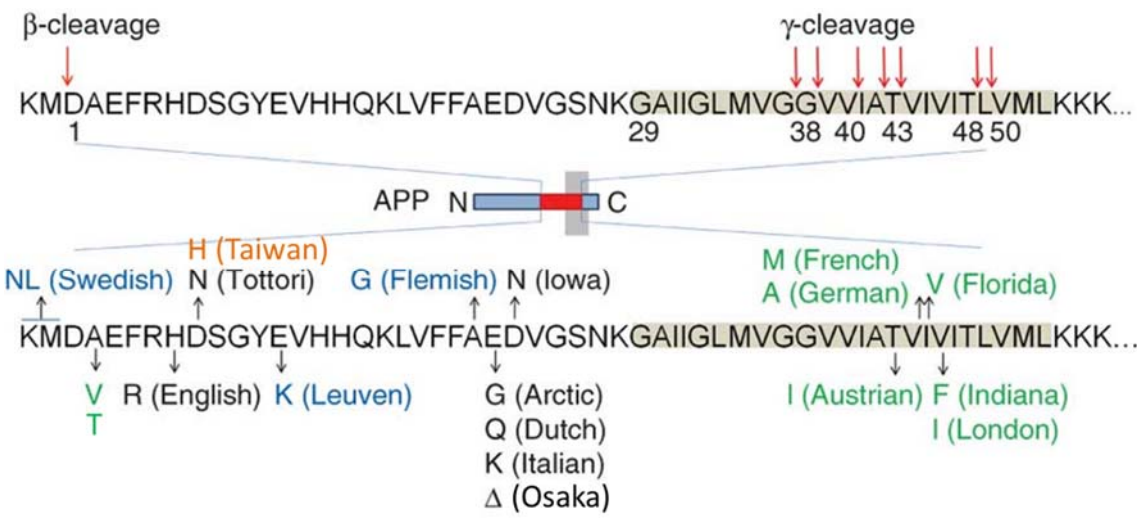

Figure 7. Mutation sites located inside and outside Aβ sequence. Adapted from ref 87. A2V and A2T mutations have not been associated with names.

1.4.2 N-terminal familial mutations, H6 and D7, in Alzheimer's disease

Hori et al. was the first to show that both N-terminal mutations at H6R (English) and D7N (Tottori) accelerate fibrillization without altering Aβ production[91]. They found H6R and D7N mutation specifically affect elongation phase rather than nucleation phase during fibrillization. They proposed that the N-terminally mutated Aβ may have a different fibrillization mechanism. Another D7 mutation, D7H, recently discovered in a Taiwanese family, behaves differently from D7N. D7H increases Aβ production along with elevated Aβ42/Aβ40 ratio, enhanced Aβ40 fibrillization, and promoted formation of low molecular wright species for Aβ42[92]. Metal ion binding studies are carried on H6 and D7 variants given that these findings illustrated the impacts of H6 and D7 mutations to the amyloidogenic properties of Aβ and other findings that histidines are critical in the coordination of metal ion. Cu^{2+} binding properties examined on H6R and D7N showed that the former influences Cu^{2+} coordination on Aβ while the latter does not[93]. D7H decreases the level of reduced Cu^{+}, indicative of lower redox activity for Cu^{2+}-Aβ D7H complex. Another N-terminal FAD mutations occur at A2 residue. A2T was derived from A673T mutation in amyloid precursor protein (APP) found from 1795 Icelanders[94]. This mutation protects the elderly against AD and cognitive decline in both homozygous and heterozygous states. A2V, found in an Italian family, was derived from A673V mutation in APP which cause AD only in homozygous state[95]. A2V disturbed APP processing,

enhanced Aβ production, and amyloid fibrils formation *in vitro*. A2V cannot form fibrils when mixed with wild type Aβ. It was reported to interfere with the coordination with Cu^{2+} as well[96].

1.5 Application of nanotechnology in the studies of Alzheimer's disease

Fast-advancing nanotechnology has proven that nanoparticles (NPs) can be conveniently modified to provide functional versatility[97–99]. NPs have been demonstrated to carry potentials in biological applications such as drug delivery[100–104], imaging[102,105–107], and diagnostic tools for diseases such as cancers[108,102]. The therapeutic target in neurodegenerative diseases is central nervous system (CNS). CNS is composed of the brain and the spinal cord, extremely important organs of human. CNS is protected by blood-brain barrier (BBB) that only allows passage of a small fraction of molecules between blood and CNS[109]. It is this property that few effective pharmaceutical molecules enters CNS to carry out functions[110–113], significantly diminishing efficacy of drugs. In this regard, versatile and multifunctional nano-sized materials have been researched intensively and extensively, showing promising applications to undertake pharmaceutical tasks aimed for precise targeting of drugs in CNS. Cherney et al. found that the metal chelating drug Clioquinol for AD can be uptaken by brain with higher efficiency in an

encapsulated form inside polybutylcyanoacrylate (PBCA) nanoparticles than in the drug only way[114]. Clioquinol inside CNS will target metals in senile plaques, and therefore can execute at least dual functions, imaging and metal-chelating. Encapsulated fluorescent probe ThT were able to be located at fibrils in microglia and neurons, where the spectroscopic properties of ThT allow scientists to detect fibrillar Aβ[115]. Excellent surface-modification capability and metallic properties of gold nanoparticles (NPs) enabled successful *in vitro* targeting to fibrils via conjugated peptide sequences and subsequent breakdown of fibrils through remote heating by microwaves[116]. More recently, Song et al. employing reconstituted apolipoprotein E3–reconstituted high density lipoprotein (ApoE3–rHDL) to validate its its accessibility to the brain after intravenous injection, preferential binding to monomeric and oligomeric Aβ, and efficiency in lysosomal degradation of brain Aβ in neuronal cells in an AD animal model[117]. Moreover, those ApoE3–rHDL not passing BBB into CNS were shown to redirect circulating Aβ to the liver for degradation.

Chapter 2 Materials and methods

2.1 Materials

Dimethyl sulfoxide (DMSO), hexafluoro-2-propanol (HFIP), and ThT were purchased from Sigma-Aldrich (St. Louis, MO, USA). Bare, amine-conjugated, and carboxyl-conjugated AuNPs were purchased from Nanopartz Inc. (Salt Lake City, UT, USA). Guanidine hydrochloride (GdnHCl), and Thioflavin T (ThT) were purchased from Sigma-Aldrich (St. Louis, MO). Tris and NaCl were purchased from Amresco (Solon, OH, USA). $CaCl_2 \cdot 2H_2O$ was from J. T. Backer (Phillipsburg, NJ, USA). $AlCl_3 \cdot 6H_2O$, $CuCl_2$, $FeCl_3 \cdot 6H_2O$, and $ZnCl_2$ were purchased from Riedel-de Haeen Inc. (Sigma-Aldrich, St. Louis, MO, USA). All metal ions stock solutions were prepared in double-distilled Milli-Q water.

2.2 Methods

2.2.1 Aβ monomer preparation

Synthetic Aβ peptide was synthesized using Fmoc (N-(9-fluorenyl) metho-xycarbonyl) chemistry and purified by reversed phase high performance liquid chromatography. The molecular mass was confirmed by MALDI-TOF mass spectrometry (UltraFlex II; Bruker BioSciences, Billerica, MA, USA). To prepare monomeric peptide stock, we employed

two preparations whose usage depended on limitations imposed by experiments. In experiments in Chapter 3 where AuNPs were involved, HFIP-DMSO method was introduced due to their compatibility with AuNPs. Briefly, powder of synthetic Aβ was freshly treated with 100 % HFIP to eliminate pre-existing aggregates. It was then sonicated for 10 min, followed by removal of HFIP using a desiccator. After desiccation, a transparent thin film of Aβ was formed. The Aβ thin film was then dissolved in DMSO at a concentration of 10 mg/mL and rapidly diluted 20-fold in 20 mM sodium phosphate buffer, pH 7.4. Centrifuged was applied at 17,000 × *g* at 4 °C for at least 10 min. The supernatant was collected and the monomer concentration was determined by the following equation

$$[A\beta] = \frac{(Abs@280\ nm - Abs@340\ nm)}{\varepsilon \times l} \qquad \text{Eqn. 1}$$

where ε is the molar extinction coefficient of protein and its unit is $M^{-1}cm^{-1}$. The path length l is the distance the light travels across the cuvette and the unit is cm. Calculation of extinction coefficient was based on the data published by Edelhoch H[118]. In the case of Aβ the strongest intrinsic fluorescence comes from the sole tyrosine residue, and therefore contributes most to the molar extinction coefficient. The molar extinction coefficient ε

used throughout this dissertation is 1,280 $M^{-1}cm^{-1}$. Subtraction of absorbance at 280 nm with that at 340 nm was used to exclude absorbance caused by turbidity.

In experiments discussed in Chapter 4, Aβ was dissolved in 8 M GdnHCl buffered in 10 mM phosphate buffer, pH 7.4, at a concentration of 5 mg/mL, followed by 30-fold rapid dilution into 10 mM phosphate buffer, pH 7.4. In Chapter 5, Aβ powder was dissolved in 8 M GdnHCl buffered in 10 mM Tris, pH 7.4, at a concentration of 10 mg/mL and was subsequently subjected to a 10-fold rapid dilution accordingly to 10 mM or 100 mM Tris, pH 7.4.

2.2.2 AuNPs preparation

AuNP concentrations were provided in the manufacture's manuals. The optical density (OD) were around 1 for the commercial AuNPs and was confirmed using a quartz cuvette with a light path of 1 cm and a DU 800 spectrophotometer (Beckman Coulter Inc., CA, USA). The concentration of AuNPs were provided in the Nanopartz's certificate of analysis for each batch. The concentration varied slightly batch by batch, but close to 400 pM in the batches we bought. The AuNPs were stored in 4 °C freezer instantly after it was delivered. Prior to the experiments, adequate amount of AuNPs were centrifuged at 17,000 × *g* at 4 °C for at least 10 min. After centrifuge, the supernatant was removed

delicately and was resuspended in Milli-Q water. This procedure was to rid of trace contaminants in the chemical synthesis.

2.2.3 Thioflavin T assay

One hundred micromolar of Aβ was mixed with AuNPs in a 1:1 ratio (% v/v) and incubated in a 384-well microplate with 50 μM ThT and 0.02 % sodium azide. The final volume was 50 μL. Continuous orbital shaking at 1,000 rpm at room temperature was employed. ThT fluorescence intensities were measured by a microplate reader (SpectraMax M5, Molecule Devices, Sunnyvale, CA, USA) at 25 °C. ThT emission was monitored at 485 nm with excitation at 442 nm. Three replicates were performed and the data were averaged. The standard deviations were calculated.

2.2.4 Dynamic light scattering

Samples of interest were subjected to size analysis by Zetasizer Nano (Malvern Instruments, Worchestershire, UK) using disposable solvent resistant micro cuvette (ZEN0040) at room temperature. Three replicates were performed and average was used to represent experimental results in each condition.

2.2.5 Transmission electron microscopy

The samples were deposited on 400-mesh Formvar carbon-coated copper grids (EMS Inc., Hatfield, PA, USA) for 2 min. Adequate amount of samples were applied onto the copper grid, followed by negative staining using 2 % uranyl acetate for 5 min. The grid was rinsed once with Milli-Q water. The samples were examined with a Hitachi H-7000 transmission electron microscope (Hitachi, Chiyoda, Tokyo, Japan) with an accelerating voltage of 75 kV.

2.2.6 Fourier transform infrared spectroscopy

IR spectra were recorded with a Thermo Scientific Nicolet 6700 spectrometer equipped with an ATR sampling accessory (PIKE MIRacle, USA). Samples were deposited onto ATR crystal, and solvent evaporation was facilitated with an air dryer blowing room temperature air. One hundred interferograms were recorded at room temperature with a resolution of 2 cm. For each spectrum, corresponding background was subtracted. All spectra between 1,500 and 1,800 cm^{-1} were normalized to unity, and were displayed between 1,600 and 1,700 cm^{-1}.

2.2.7 Far-UV circular dichroism spectroscopy

Far-ultraviolet circular dichroism (far-UV CD) spectra were collected from 250 to 200 nm at 25 °C using a Jasco J-815 spectropolarimeter (Jasco Inc., MD, USA). A quartz cuvette with a path length of 3 mm was used. Three scans were recorded and averaged for each measurement.

2.2.8 Fluorescence lifetime measurement

Samples were added to a cuvette (Hellma Analytics, Germany) with 3 mm light path. The cuvette was mounted into a home-made black chamber for measurement. The detector was set to record the fluorescent lights emitting from the cuvette and making a right angle to the incident light path. The Monochromatic laser source at 442 nm was used for excitation and was supplied by a computer controlled multichannel picosecond diode laser driver “Sepia II” module (PicoQuant, Berlin, Germany). A Time-correlated single-photon counting (TCSPC) module “PicoHarp 300” (PicoQuant, Berlin, Germany) was employed for photon collection and counting. A grating filter was used to ensure emission fluorescence at 485 nm was detected. Instrumental response function (IRF) was also recorded.

2.2.9 Stopped-flow fluorescence

The kinetics of Aβ and metal ion binding was examined using a stopped flow module (Bio-Logic, Claix, France) attached to a Jasco J-815 spectropolarimeter. The stopped-flow module was composed of a multimixer SFM-400, a motor power supply MPS-250, and a photomultiplier system PMS-250. A fluorescence cuvette, FC-15, with an optical path of 1.5 mm was used. Excitation at 270 nm was used to monitor the tyrosine fluorescence of Aβ at 12.5 μM. A single mixing reaction using a volume ratio of 9:1 for the metal ions and Aβ was performed at 25 °C. The final metal ion concentrations were 1.25 mM. The metal-to-Aβ ratio was 100 to 1. Here, Aβ was prepared in 100 mM Tris buffer, pH 7.4, to avoid metal-ion-induced acidity. In this setting, the final pH is above 7.0 after reactions. The flow rate was fixed at 11 mL/s, resulting in a dead time of 4.7 ms. The data were collected every 0.5 ms for the first 2 s, every 20 ms in the range of 2–60 s, and every 0.5 s for 60–100 s. The data were fitted to multi-exponential equations using Bio-kine 32 V4.51 (Bio-Logic, Claix, France) with either single or double exponential equations with a linear base line,

$$F_{obs} = at + b + c_1 \times e^{-k_1 t} \qquad \text{Eqn. 2}$$

$$F_{obs} = at + b + c_1 \times e^{-k_1 t} + c_2 \times e^{-k_2 t} \qquad \text{Eqn. 3}$$

where a and b are the slope and offset for the linear base line, and c and k are the amplitudes and rate constants for the exponential phases, respectively.

2.2.10 Fluorescence spectroscopy

Each of 25 μM Aβ peptide in 10 mM Tris, pH 7.4, were independently titrated with 100 mM Tris-buffered 2 mM $CuCl_2$ or $ZnCl_2$, pH 7.4, to final 8 molar equivalent metal ion. Volume increase due to titrated metal ions was less than 10 % of the initial volume. Excitation wavelength was set at 270 nm. Emission spectra from intrinsic fluorescence of tyrosine (Y10) residue were recorded from 290 to 360 nm using a FluoroMax-3 spectrofluorometer (Horiba Jobin Yvon). For Bis-ANS measurement, excitation wavelength was 400 nm and emission fluorescence was monitored from 450 nm to 550 nm. Slit widths were 3 nm for excitation and 5 nm for emission. Temperature of titration experiments was controlled by a circulating water bath and set at 25 °C.

2.2.11 Proton and ^{1}H-^{15}N HSQC NMR spectroscopy

Proton (^{1}H) and ^{1}H-^{15}N heteronuclear single quantum coherence (HSQC) NMR measurements were performed on Bruker Avance 600 MHz NMR spectrometer equipped with 5 mm triple resonance cryoprobe and Z-gradient. In ^{1}H NMR experiments, 50 μM of unlabeled Aβ peptide was prepared using GdnHCl method in 10 mM Tris buffer containing 90 % D_2O, pH 7.4. In HSQC experiments, 50 μM of ^{15}N-labeled peptides was prepared using the same method in proton NMR except that 10 mM Tris buffer containing

10 % D_2O, pH 7.4, was used instead. Titrated Cu^{2+} were prepared in 100 mM Tris buffer containing 10 % D_2O, pH 7.4. All NMR experiments were conducted at 5 °C. Shigemi NMR microtubes (Shigemi, Inc., USA) were employed. Sample volume was 250 μL. Volume of titrated Cu^{2+} was less than 10 % of initial volume. Forty eight scans were accumulated to acquire each spectrum

Chapter 3 Interference of gold nanoparticles in the fibrillization process of wild type Aβ40

3.1 Aims

Literature review revealed that nano-sized polymers are able to influence the nucleation phase in Aβ40 fibrillization[119], inorganic NPs can inhibit fibrillization of Aβ42[120], and biodegradable poly(ethylene glycol)methyl ether-block-polylactide (PEG-*b*-PLA) NPs can promote its interactions with Aβ42[121]. However, it was still unclear that what properties of NPs are key factors in fibrillar inhibition and whether the end products Aβ after inhibition by NPs have lower cellular toxicity. The latter is of critical importance in developing NPs into practical tool for therapeutics. Motivated by these unanswered questions and a demonstration that bare gold nanoparticles are capable of tipping lysozyme in native state towards forming aggregates[122], we decided to initiate a project to explore the effect of bare AuNPs on the fibrillization of a model amyloid system, wild type Aβ40, *in vitro*. The charge property of AuNPs was also examined whether it plays a role in the interactions between AuNPs and amyloid.

3.2 Bare AuNPs inhibit Aβ fibrillization without self-clustering

The quality of commercial 30 nm AuNPs were confirmed by absorption spectrum and DLS right after we received the product shipment. Typical absorption spectrum of AuNPs with 30 nm in diameter had a single absorption peak at around 523 nm (Figure 8). We initiated the study by co-incubating various concentrations of bare AuNPs and Aβ monomers and monitored Aβ fibrillization using ThT assay. In this chapter, Aβ is used throughout to stand for Aβ40. ThT is a classic amyloid dye that is commonly used to probe Aβ fibril formation due to its strong fluorescence emission upon binding to cross-β fibril structures[31,123,124]. In our experiments, 100 μM Aβ monomers were mixed in 1 to 1 volume ratio at 25 °C to reach the desired final concentration. The final peptide concentration was 50 μM buffered in10 mM sodium phosphate buffer, pH 7.4, and AuNPs concentrations ranged from 0 to 2.72 nM. The samples were continuously agitated at 1,000 rpm in the presence of 50 μM ThT. The ThT fluorescence intensities were monitored at indicated time points for 72 h and the Aβ fibrillization kinetics in the absence and presence of bare AuNPs are shown in Figure 9. The kinetics for Aβ alone exhibited characteristics of amyloid fibril formation, where a lag phase about 6 h was followed by an elongation phase lasting for about 13 h and a steady state after 18 h. The lag phases were not significantly changed in the presence of AuNPs. We found the ThT intensity decreased in an AuNP dose-dependent manner, in which a transition was between 0.042

to 2.72 nM AuNPs. The results indicated that addition of bare AuNPs to Aβ monomers interfered with Aβ fibrillization pathways.

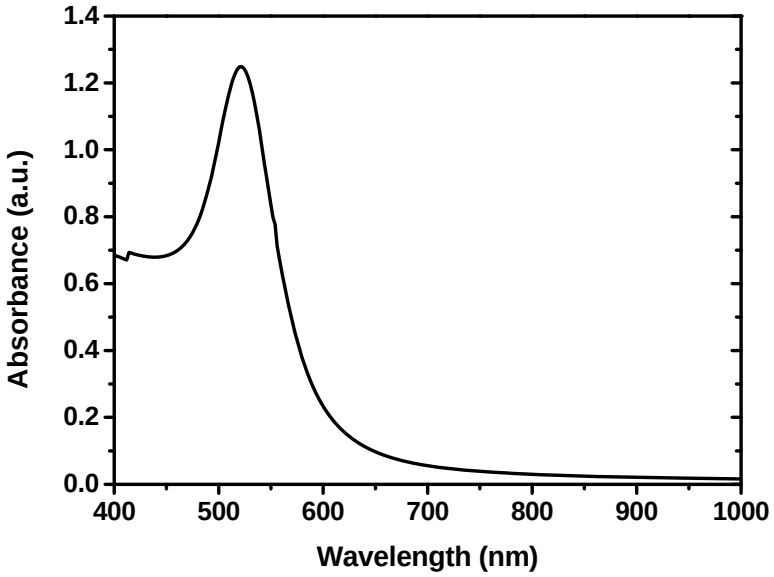

Figure 8. Absorption spectrum of 30 nm AuNPs. Stock suspension taken directly from purchased Nanopartz bare AuNPs (~400 pM) was measured directly. Milli-Q was used as a blank solution.

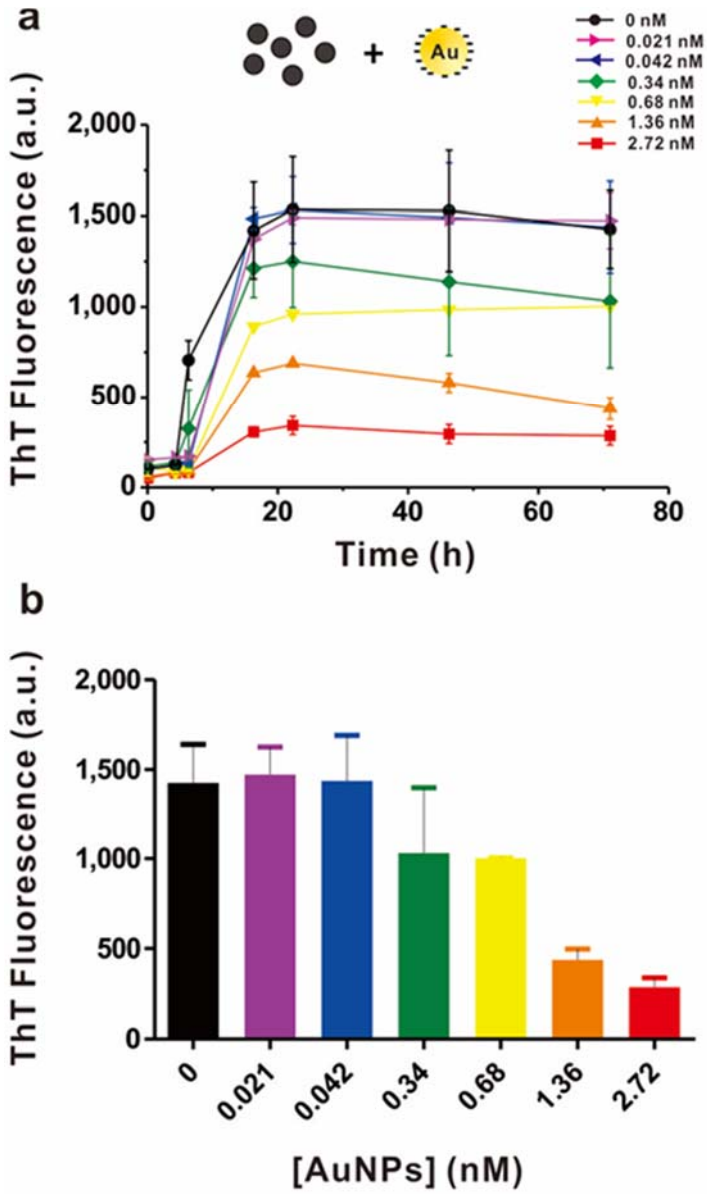

Figure 9. Time course of ThT fluorescence changes of Aβ monomers incubated with and without 30 nm AuNPs. Fifty micromolar Aβ was incubated in the absence and in the presence of 0.021 nM to 2.72 nM 30 nm AuNPs. A 384-well opaque microplate was used. The samples were continuously agitated by orbital shaking at 1,000 rpm. (a) Fifty micromolar of ThT was employed to report formation of fibrils for 72 h. The inset on the upper part of this figure illustrates that bare AuNPs were mixed with monomeric Aβ before co-incubation. (b) The ThT fluorescence intensities of (a) at 72 h.

3.3 Bare AuNPs alter ThT fluorescence intensity of preformed Aβ fibrils

Next, we investigated the effects of AuNPs on the preformed Aβ fibrils by ThT assay. Preformed Aβ fibrils were first prepared by incubating 100 μM of Aβ monomers at room temperature with continuous orbital shaking at 1,000 rpm for more than 80 h. The preformed fibril formation was validated by the elevated ThT fluorescence and TEM imaging. The preformed fibrils were then mixed with various concentrations of the 30 nm AuNPs in a 1 to 1 ratio volume ratio and monitored in the same incubation condition described in Chapter 3.2. During the incubation, all ThT fluorescence intensities slowly decreased (Figure 10). Fibril sedimentation might be accounted for the decrease of ThT intensity level of Aβ fibril alone[125]. Interestingly, the initial ThT intensities were decreased in an AuNP dose-dependent fashion, indicative of fast interacting kinetics occurred between AuNPs and mature fibrils. The data showed a decreasing trend in the ThT fluorescence intensities during incubation. The results indicated that AuNPs also affect the properties of the preformed Aβ fibrils to some extent.

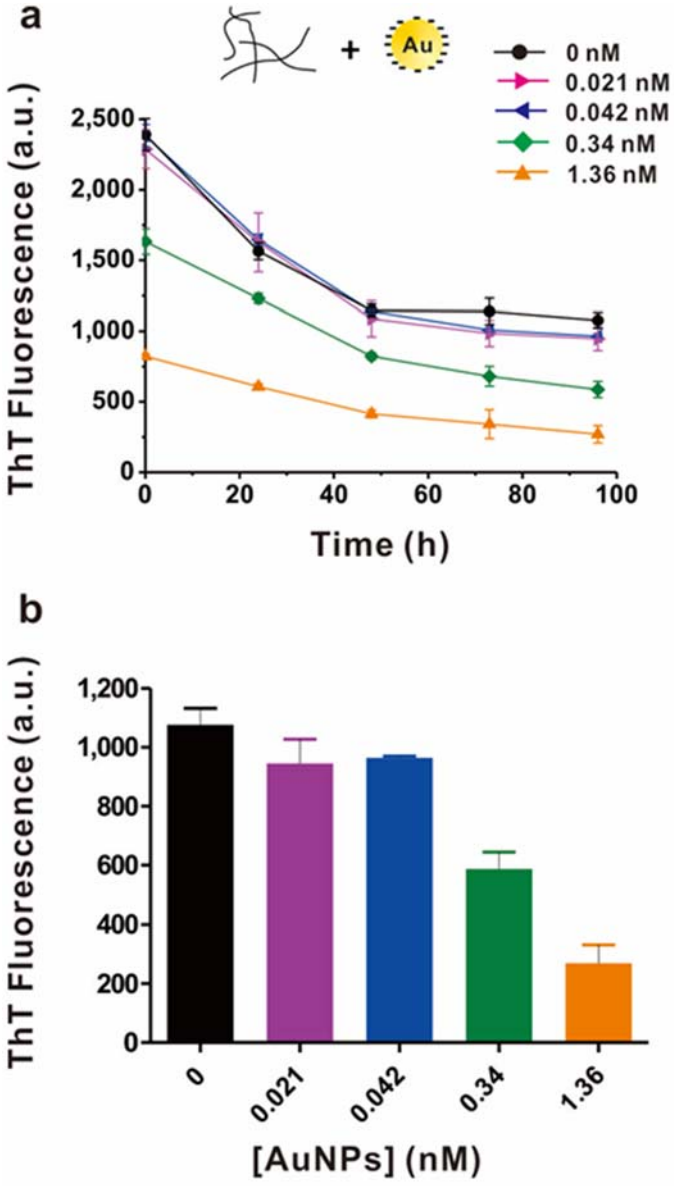

Figure 10. Time course of ThT fluorescence changes of preformed Aβ fibril incubated with and without bare AuNPs. Fifty micromolar preformed Aβ fibrils were incubated in the absence and in the presence of 0.021 nM to 1.36 nM 30 nm AuNPs. A 384-well opaque microplate was used, and the samples were continuously agitated at 1,000 rpm. (a) Fifty micromolar of ThT was employed for recording changes in ThT fluorescence intensities for up to 96 h. The inset on the upper part of this figure illustrates that bare AuNPs were mixed with fibrillar Aβ and continued incubation. (b) The ThT fluorescence intensities of (a) at 96 h.

3.4 Absorbance spectra of Aβ monomers or preformed Aβ fibrils

AuNPs have been reported to form self-clusters while inducing lysozyme aggregation[122]. The final clusters exhibited red-shifted absorbance spectra due to the plasmonic coupling between the aggregated AuNPs. Hence, we asked whether AuNPs incubated with Aβ also generated AuNPs self-clusters. Replicated samples were prepared and subjected to absorbance measurement following the condition for ThT assays. The absorbance spectra were recorded from 400 to 1,000 nm at different time points for Aβ monomers (Figure 11a) or preformed Aβ fibrils incubated with 1.36 nM AuNPs (Figure 11b). We did not observe any absorption shift in both cases, which indicates that the AuNPs did not form self-clusters during incubation with Aβ monomers or preformed Aβ fibrils.

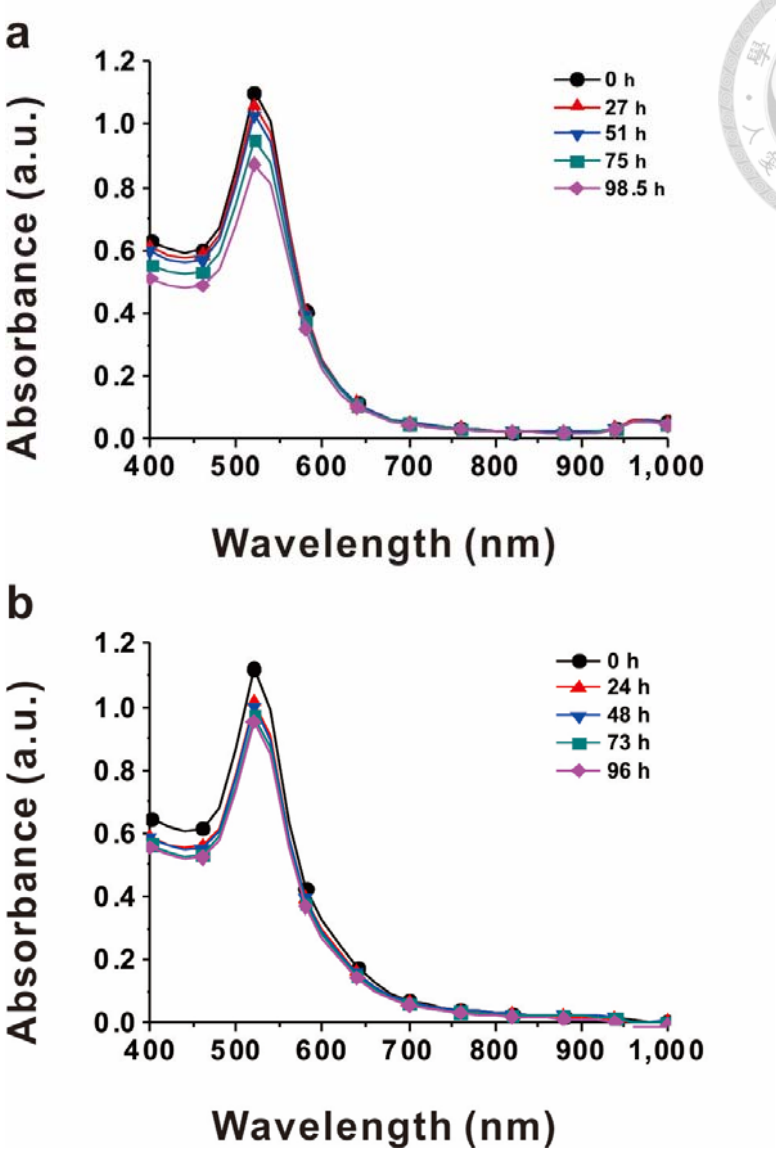

Figure 11. Time course absorbance spectra of Aβ monomers or preformed Aβ fibrils incubated in the presence of 1.36 nM AuNPs. Fifty micromolar of (a) Aβ monomers and (b) preformed fibrils were incubated in the presence of 1.36 nM of 30 nm AuNPs. A 384-well opaque microplate was used, and the samples were continuously agitated at 1,000 rpm.

3.5 DLS analysis shows redirected Aβ species in the presence of AuNPs

To confirm the results obtained from ThT assays, we employed DLS to study the particle size distributions (Figure 12). DLS is frequently used to examine the hydrodynamic radius of spherical particles in solution and the intensity of scatter lights is dominated by large particles in solution. Although Aβ fibrils are heterogeneous and with long rod-like shapes, DLS analysis can provide a qualitative estimation of the aggregate distribution. Here, we first examined the size distributions of the AuNPs alone (Figure 12c). Triplicate measurements were carried out and shown. The data were plotted as scattered light intensity versus size in diameter. The samples were diluted in double distilled water and measured in disposable DLS cuvettes. In the case of 0.34 nM AuNPs alone, a single peak at ~60 nm was observed. For the end-point products of Aβ monomers in the absence and presence of 0.021 to 2.72 nM AuNPs (Figure 12a), we found that Aβ only control showed three major populations of large particles with the diameters at ~100 nm, ~700 nm, ~4 μm. With increasing AuNP concentrations, such large species decreased in intensity and the species became smaller. In the presence of 2.72 nM AuNPs, no large species were observed and a single species with a diameter of ~60 nm was detected, which may be contributed from the AuNPs. Moreover, we examined the species generated from incubating AuNPs with preformed Aβ fibrils (Figure 12b). In the absence of AuNPs, DLS analysis of preformed fibrils showed heterogeneous distribution of large aggregates

populated from 100 nm to 5 μm. Upon incubation with AuNPs, DLS intensities from large particles decreased and the scattering was gradually dominated by particles smaller than 100 nm. Above 0.34 nM AuNPs, no large species were detected. Instead, a major peak situated at ~60 nm and a minor peak at ~8 nm were observed. Taken together, the diminishment of larger aggregates, > 100 nm, may reflect the population changes in Aβ species after AuNPs incubation.

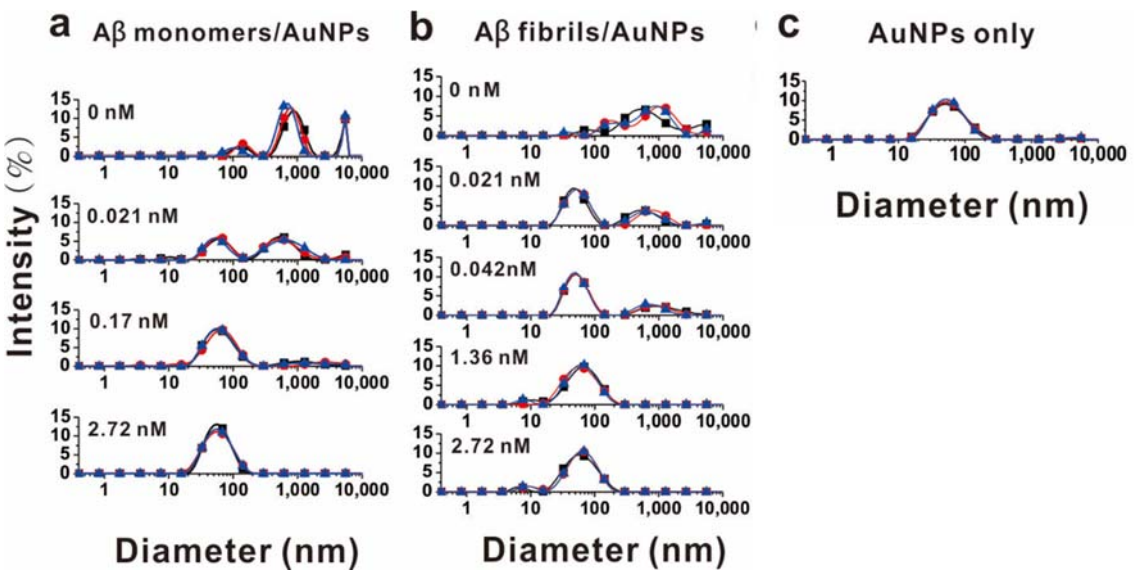

Figure 12. DLS analysis of size distribution of the Aβ species induced by AuNPs. Incubated samples, (a) 72 h-incubated Aβ monomers, (b) 96 h-incubated Aβ preformed fibrils, and (c) 72 h-incubated AuNPs, were subjected to size analysis using DLS at room temperature.

3.6 Bare AuNPs induce Aβ fibril fragmentation and oligomer formation and preferentially bind to Aβ fibrils

To further verify the results from the DLS analysis, TEM was used to visualize the morphological properties of the end-point products from either incubated with Aβ monomers (Figure 13a-f) or preformed fibrils (Figure 13g-l). In the absence of AuNPs, Aβ formed long, smooth, and entangled fibrils as expected (Figure 13a). However, upon incubation with different AuNP concentrations as indicated, several Aβ species were observed. Some fibrils seemed fragmented and became shorter or truncated, which are pointed out by black arrows in Figure 13. Moreover, many spherical oligomers ranging from 10 to 15 nm in diameter were observed (pointed out by white arrows in Figure 13). Such species were either attached to or located in close proximity to the fibrils without associating with the AuNPs. Few AuNP clusters were found, which is consistent with the result from absorbance spectra, implying AuNPs did not self-aggregate (The spherical black particles with a diameter of ~30 nm in the images were the AuNPs). On the other hand, co-incubation of the preformed Aβ fibrils with AuNPs resulted in morphologically changes in fibrils as well. In the presence of 0.34 and 1.36 nM AuNPs, we found coexistence of ragged fibrils and some small spherical oligomer-like structures with diameters ~5 to 8 nm (Figure 13g-j). The amorphous aggregated species increased with increasing AuNP concentrations. In the presence of 10 nM AuNPs, we found a striking

contrast that AuNPs preferentially attached to the mature fibrils rather than the amorphous aggregates. AuNPs seemed to alter the morphology of fibrils, inducing oligomer and amorphous aggregate formation. The TEM images demonstrated a consistent phenomenon with our ThT and DLS studies.

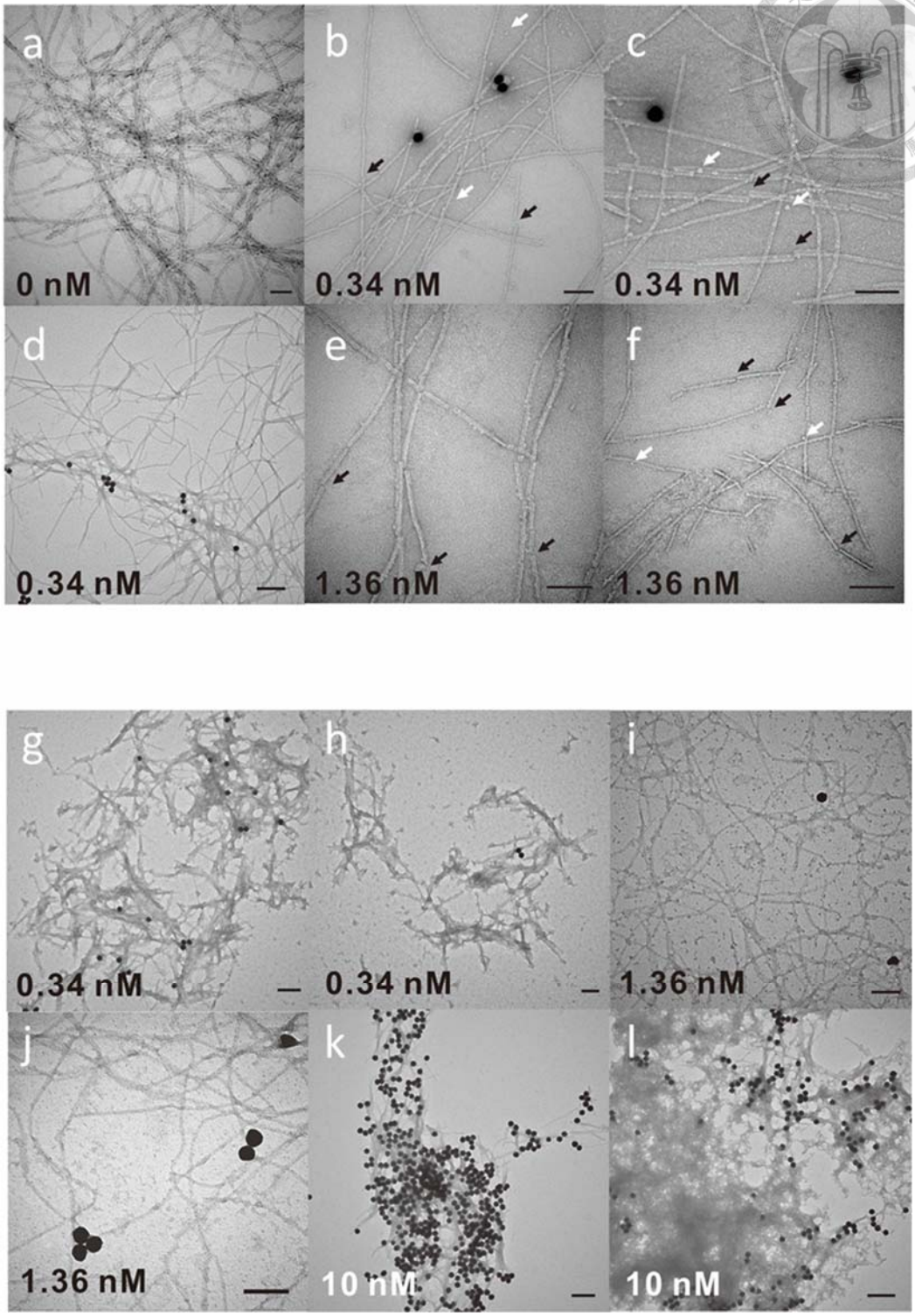

Figure 13. TEM images of co-incubated monomeric Aβ and bare AuNPs, and co-incubated Aβ fibrils. Scale bar is 100 nm. Black arrows indicate frag-mentation of fibrils. White arrows indicate spherical oligomers. The number at the lower left corner in each image indicates the concentration of AuNPs.

3.7 Negatively charged AuNPs inhibit Aβ fibrillization in vitro

To understand the molecular interactions between AuNPs and Aβ, we asked whether the surface potential of AuNPs is the main factor contributed to this phenomenon. We used different surface modified AuNPs including amine- and carboxyl-conjugated AuNPs to examine the charge effect on Aβ fibrillization (Figure 14). The AuNPs used here were all 30 nm in diameters. The surface conjugated and bare AuNPs were incubated with Aβ monomers and monitored by ThT assays as previously described. Interestingly, we found that only the carboxyl-conjugated and bare AuNPs have inhibitory effects to Aβ fibrillization, but not the amine-conjugated AuNPs. The amine-conjugated AuNPs elongated slightly slower than that of the Aβ only control, but reached the same ThT intensity after 40 h. Nevertheless, the bare and carboxyl-conjugated AuNPs showed similar patterns with the final ThT at a much lower level than that of the Aβ control. The results suggested that the surface negative charges of AuNPs are essential for the interactions of Aβ and AuNPs leading to inhibiting the fibrillization. The end-point products from both surface modified AuNPs were examined by TEM and distinct morphologies were observed. After incubating with amine-conjugated AuNPs, the mass majority of Aβ still formed mature fibrils exhibited characteristic structures (Figure 15a), which is consistent with the ThT data. Few amine-conjugated AuNPs were seen on the EM grids. While incubating with carboxyl-conjugated AuNPs, only very short Aβ

filaments, <100 nm, and oligomers were observed. The carboxyl-conjugated AuNPs mostly attached to such short species (Figure 15b and c).

One of our lab member, Mr. Yu-Jen Chang, examined whether the end products of Aβ after co-incubation with bare and negatively charged AuNPs alleviate the toxicity. Results from his work are included in the discussion chapter. Data of cytotoxicity assays are shown in the supplementary.

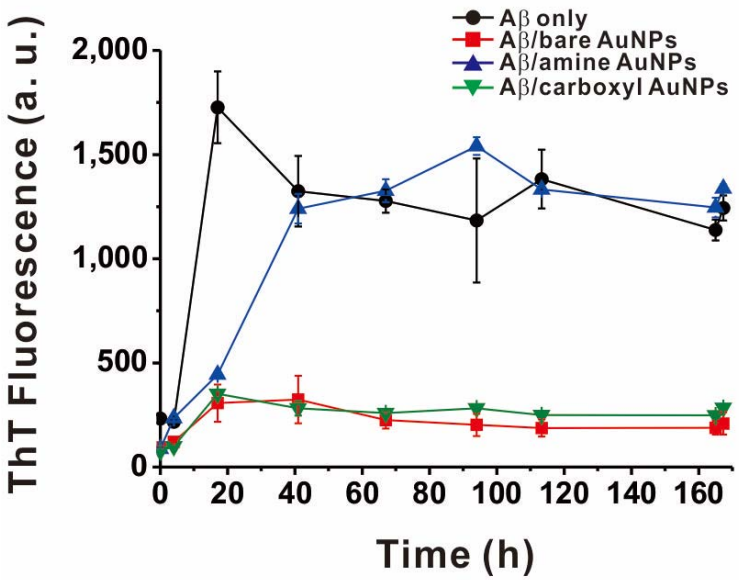

Figure 14. Fibrillization kinetics of Aβ in the absence and prescence of 1.36 nM bare, amine-, and carboxyl- conjugated AuNPs recorded by ThT assays. Aβ concentration is 50 μM. The concentration of all three kinds of AuNPs is the same at ~400 pM. Fifty micromolar of ThT was used.

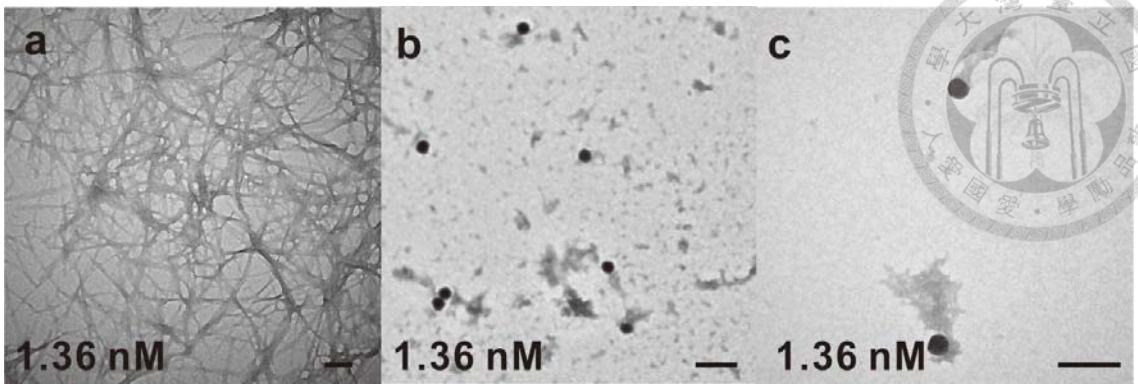

Figure 15. TEM images of the 160 h-incubated Aβ in presence of 1.36 nM AuNPs. (a) amine-conjugated and (b and c) carboxyl-conjugated AuNPs. Scale bar is 100 nm.

Chapter 4 Structural differences between homo-polymeric and hetero-polymeric Aβ fibrils

4.1 Aims

Seeding experiments manifested that amyloidogenic proteins or peptides can turn into amyloid fibrils with a variety of sequence-similar ones and with different efficiency[126,127]. In addition, different ratios of mixed Aβ40 and Aβ42 were shown to impact on the progression of fibrillization[127–129]. Evidence from *in vitro* aggregation assays in Kulic et al. work showed anti-amyloidogenic property of heterozygous APP E693Δ mutation (E22Δ for Aβ) and an inhibitory effect of E22Δ Aβ42 on the fibrillization of E22Δ Aβ40 [130]. A similar phenomenon was reported in heterozygous state of APP A673V (A2V) mutation[95] and in both homozygous and heterozygous states of A673T (A2T)[94]. Therefore, we were motivated by these experimental results to address whether fibrils of Aβ E22 and D23 variants formed hetero-polymerically are structurally different from that formed homo-polymerically, and whether the unique difference can be revealed by the binding properties of ThT and by secondary structures.

4.2 Homo- and hetero- fibrils are morphologically indistinguishable under TEM imaging.

We utilized ThT to report fibrillization of homo- and hetero- fibrils. A stock concentration of at least 50 μM monomeric Aβ, homo-polymerically or hetero-polymerically were incubated at 25 ^{0}C in quiescence for at least two weeks. In our experimental setup, the four hetero-fibrils of E22 and D23 variants, E22G, E22K, E22Q, and D23N, are fibrillized by quiescent incubation of equal-molar-mixed monomeric variants and wild type Aβ40. For instance, E22G hetero-fibrils were formed by quiescent incubation of mixture of E22G and wild type monomers. On the other hand, E22G homo-fibrils were formed singly from quiescent incubation of monomeric E22G. In some fibril preparations, we made the starting materials in total 25 μM instead of 50 μM due to lower refolding yield of the peptide. Figure 16 shows the fibrillar morphology confirmed by TEM imaging. Scale bar represents 100 nm.

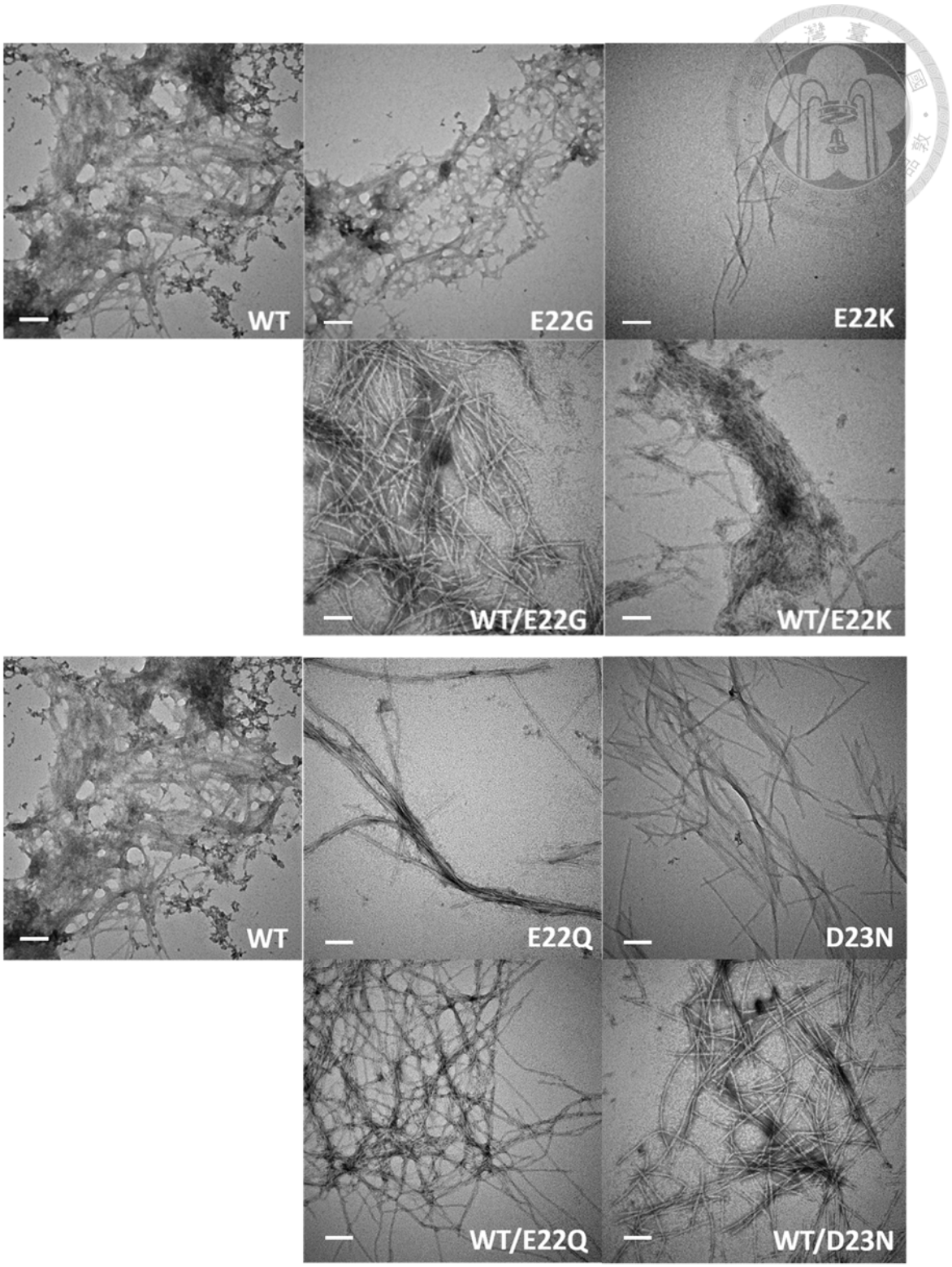

Figure 16. TEM images of homo- and hetero- fibrils of E22G, E22K, E22Q, and D23N. Scale bar is 100 nm. Fibrils were incubated in quiescence for at least two weeks at 25 ^{0}C.

4.3 Binding stoichiometry of Thioflavin T to amyloid-β fibrils

We speculated that any structural difference of the fibrils could result in differential ThT binding to amyloid fibrils. First we titrated homo-fibrils with ThT. The incubated stock fibril solutions were centrifuge at 17,000 × *g* at 4 °C for at least 10 min. Supernatant was removed and precipitated fibrils were resuspended in Milli-Q water. Increasing concentration of ThT drastically elevated fluorescence readings, indicating effective ThT binding onto amyloid fibrils composed of characteristic cross-β sheet. For all FAD homo-fibrils, 80 % of ThT fluorescence was achieved before 5 μM (one molar equivalent) ThT was titrated in. Beyond this concentration, elevation of ThT fluorescence rapidly declined as evidenced by the slow increase in ThT intensity (Figure 17a). For hetero-fibrils, intensities of ThT fluorescence increased before 2 molar equivalent ThT was added and remained unchanged beyond that ratio. Stoichiometry conformed to 2:1 ThT to fibril ratio (Figure 17b). Taken together, our results showed and implicated that the two molar equivalent ThT binds to one molar of all the fibrils studied.

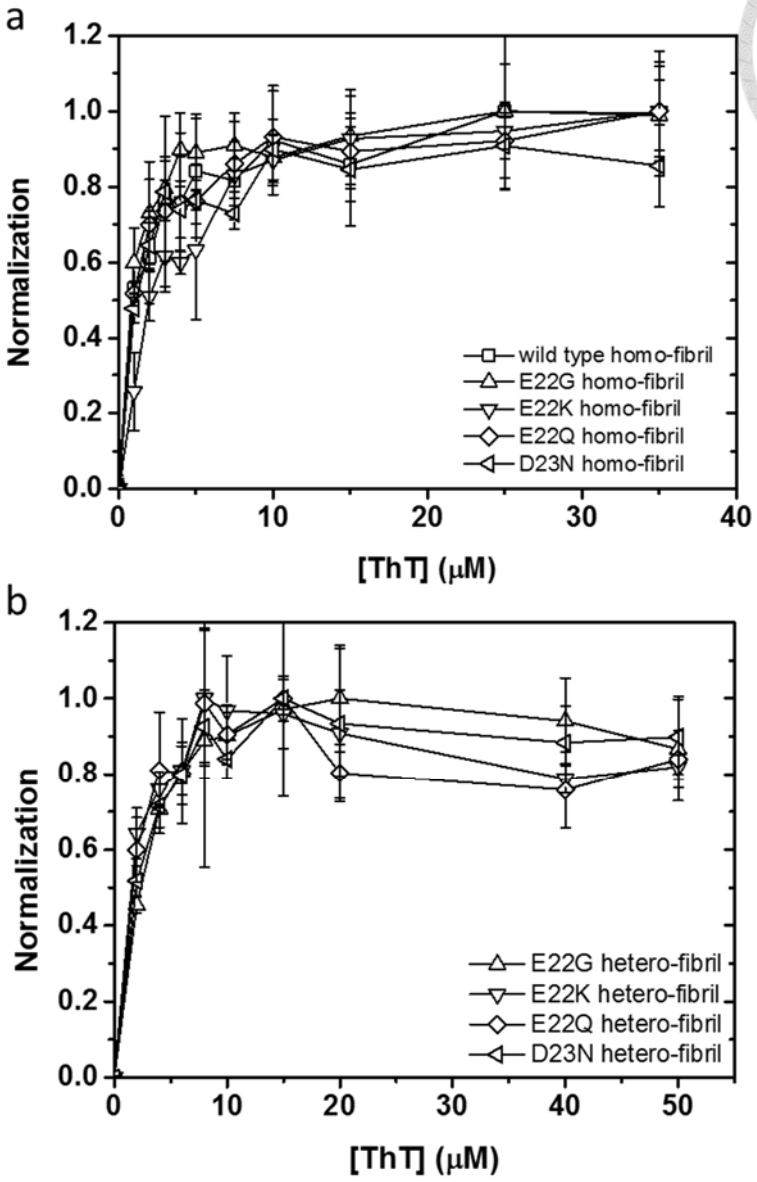

Figure 17. ThT binding stoichiometry of (a) homo-and (b) hetero- fibrils. Total peptide concentration was 50 μM. For hetero-fibrils, equal molar (25 μM) of each FAD variant monomers were co-incubated with wild type ones at room temperature for at least two weeks. The incubated stock fibril solutions were centrifuge at 17,000 × *g* at 4 °C for at least 10 min. Supernatant was removed and precipitated fibrils were resuspended in Milli-Q water.

4.4 Secondary structures of fibrils revealed by far-UV circular dichroism

All homo-fibrils except E22K exhibited a spectral minimum near 220 nm wavelength (Figure 18), indicating fibrils were enriched in β-sheet structures. More detailed analysis revealed that the spectral minima of both E22G and E22Q were situated at 222 nm, but wild type and D23N had spectral minima at 219 nm. Spectral minima of E22K fibrils was at 228 nm despite that the spectrum resembled β-sheet profile.

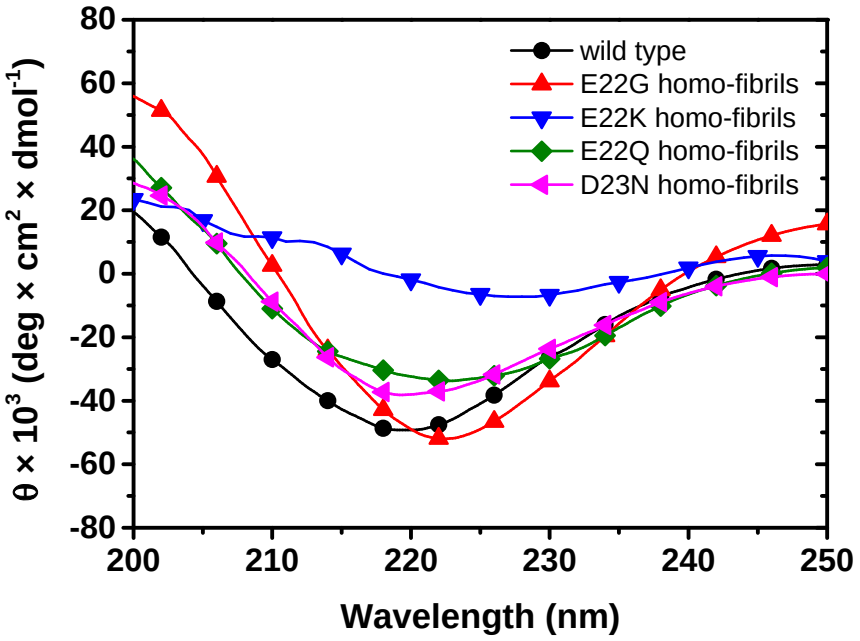

Figure 18. CD spectra of homo-fibrils. Fibrils were processed The incubated stock fibril solutions were centrifuge at 17,000 × *g* at 4 °C for at least 10 min. Supernatant was removed and precipitated fibrils were resuspended in Milli-Q water.

In each figure from Figure 19a to Figure 19d we juxtaposed CD spectrum of wild type homo-fibrils, one FAD homo-fibrils and corresponding hetero-fibrils, and equal-molar-mixed homo-fibrils. Spectra of equal-molar-mixed homo-fibrils served as control group to demonstrate that the observed differences of hetero-fibrils came from genuine structural characteristics instead of spectral superimposition of homo-fibrils of parental species. CD spectrum of E22G hetero-fibrils almost overlapped with that of wild type hetero-fibrils, suggesting that in terms of secondary structure it resembles more to wild type than to E22G homo-fibrils (Figure 19). All hetero-fibrils showed marked differences from their counterpart equal-molar-mixed control, providing authenticity of our observations. WT/E22K fibril exhibited an almost flat profile (Figure 19b). E22Q hetero-fibrils showed a spectral minimum at 225 nm, which deviated by 5 nm from the 220 nm shared by wild type and E22Q homo-fibrils Figure 19. Similar phenomenon was also observed for D23N (Figure 19d). To summarize, CD spectra revealed that E22G hetero-fibrils resembled more to wild type ones, E22K and E22Q hetero-fibrils resembled more to, respectively, E22K and E22Q homo-fibrils, and D23N hetero-fibrils resembled to neither of its corresponding homo-fibrils.

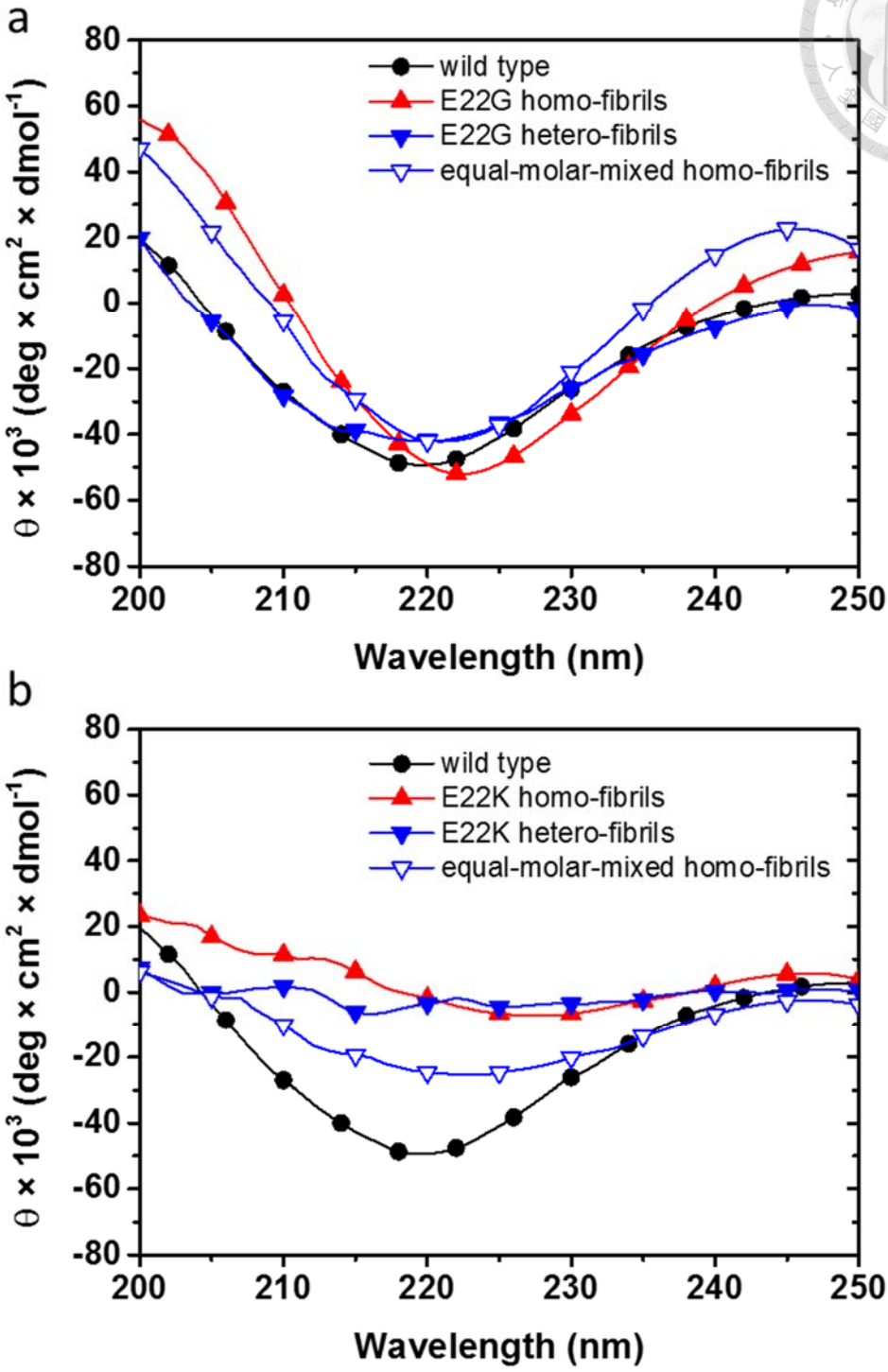
a
wild type
E22G homo-fibrils
E22G hetero-fibrils
equal-molar-mixed homo-fibrils
θ × 10³ (deg × cm² × dmol⁻¹)
Wavelength (nm)
b
wild type
E22K homo-fibrils
E22K hetero-fibrils
equal-molar-mixed homo-fibrils
θ × 10³ (deg × cm² × dmol⁻¹)
Wavelength (nm)

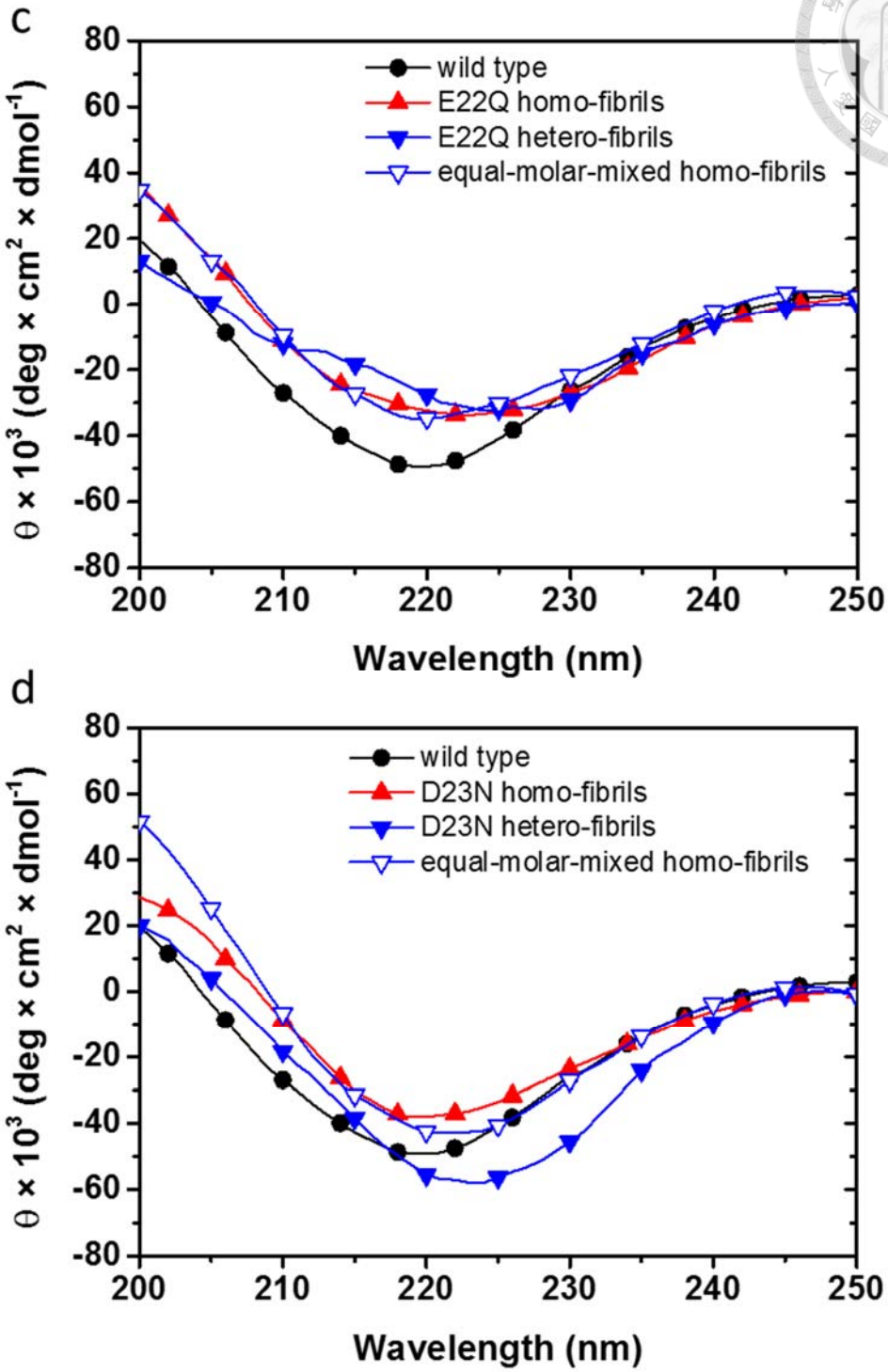

Figure 19. CD spectra of each FAD homo-fibrils, hetero-fibrils, and equal-molar-mixed homo-fibrils. The incubated stock fibril solutions were centrifuge at 17,000 × *g* at 4 °C for at least 10 min. Supernatant was removed and precipitated fibrils were resuspended in Milli-Q water.

4.5 Secondary structures of fibrils revealed by Fourier transformation infrared spectroscopy

We complemented CD spectroscopy data with another commonly used tool, FTIR, attempting to further examine that the β-sheet structures revealed by CD spectra are the determinant cross β-sheet of amyloid fibrils. Fibrils were precipitated and resuspended in Milli-Q water as described in methods prior to each measurement. Original absorbance spectra between 1,500 cm^{-1} to 1,800 cm^{-1} were processed and presented as normalization. It facilitated comparison of relative content of secondary structures in fibrils. All fibrils, homopolymeric or heteropolymeric, exhibited similar FTIR spectral profiles (Figure 20 and 21). The β-sheet characteristic 1,630 cm^{-1} peaks were the most dominant for all six homo-fibrils. Compared to wild type homo-fibrils, spectra of E22G and D23N homo-fibrils similarly had lower 1,660 cm^{-1} peak and slightly higher peak between 1,640 cm^{-1} and 1,650 cm^{-1}. The spectrum of E22Q homo-fibrils was similar to that of E22G and D23N in the region between 1,640 cm^{-1} and 1,650 cm^{-1}, but was higher in the 1,660 cm^{-1} peak than E22G and D23N homo-fibrils. Spectrum of E22K homo-fibrils was the highest among the six between wavenumber 1,640 - 1,700 cm^{-1}.

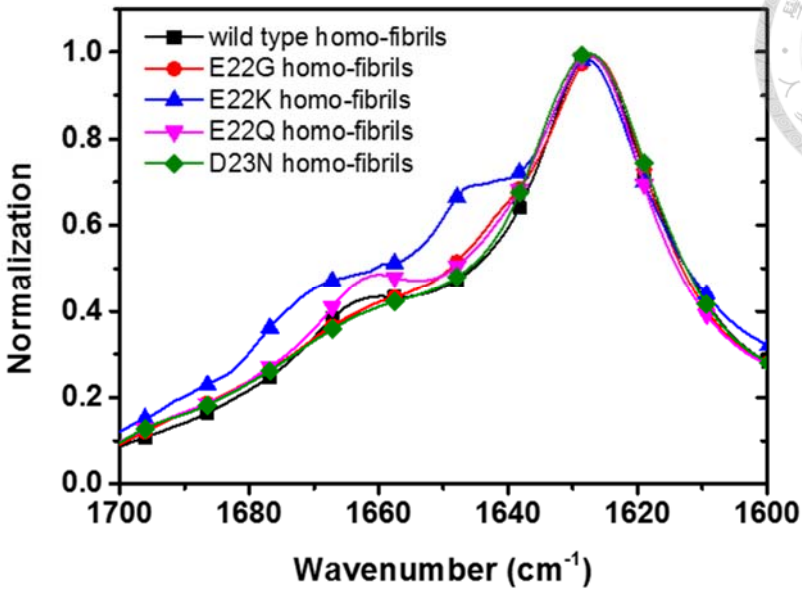

Figure 20. FTIR spectra of homo-fibrils. A hundred microliter of stock solution of fibrils were centrifuged at 17,000 × *g* at room temperature. Supernatant was discarded and precipitated fibrils were re-suspended in 10 μL of 10 mM sodium phosphate buffer, pH 7.4. Re-suspended fibrils were deposited on the ATR crystal prior to drying by non-heated air flow from a hair dryer.

Juxtaposition of CD spectra of wild type homo-fibrils, FAD homo-fibrils and hetero-fibrils, and equal-molar-mixed homo-fibrils again were presented in Figure 20 and 21 for better differentiation. E22G homo-fibrils had a similar spectrum as wild type one (Figure 21a), but we noticed an elevated absorbance in the 1,650 cm^{-1} region, implicating more α-helices/random coil content[131]. Spectra of E22G hetero-fibrils and equal-molar-mixed homo-fibrils overlapped very well with E22G homo-fibrils, suggesting all three species bear identical secondary structure contents. E22K homo-fibrils exhibited increased

absorbance in regions around 1,650 cm^{-1} and 1,670 cm^{-1} (Figure 21b). Peak around 1,670 cm^{-1} is suggested to represent β-turns and other secondary structures[131]. E22K hetero-fibrils had a less evident peak at 1,630 cm^{-1}. This indicated that β-sheet content are relatively less abundant than other secondary structures. Spectrum of E22Q homo-fibrils, compared to wild type one, had a slightly higher peak around regions from 1,640 cm^{-1} to 1,660 cm^{-1}, but spectrum of E22Q hetero-fibrils was elevated at the same regions (Figure 21c). For D23N homo-fibrils, its spectrum, like E22G, only showed mildly lower peak around 1,660 cm^{-1} when compared to wild type, but absorbance elevation was observed for D23N hetero-fibrils at regions ranging from 1,400 cm^{-1} to 1,700 cm^{-1} (Figure 21d). In summary, we found each of the four FAD hetero-fibrils had relatively fewer content of β-sheet than did corresponding homo-fibrils. The most dramatic difference was found for E22K.

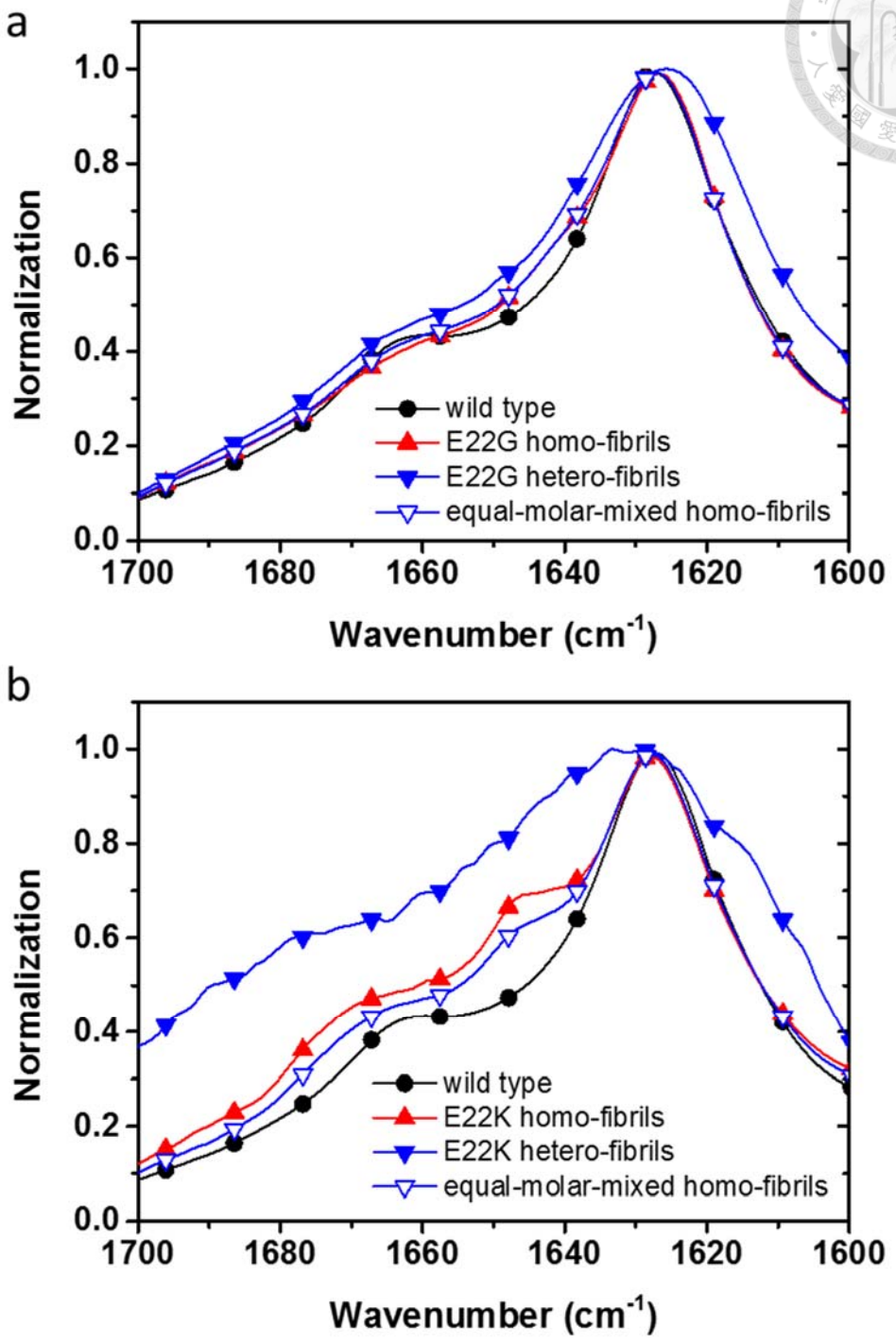
a
Normalization
1.0
0.8
0.6
0.4
0.2
0.0
1700
1680
1660
1640
1620
1600
Wavenumber (cm-1)
wild type
E22G homo-fibrils
E22G hetero-fibrils
equal-molar-mixed homo-fibrils
b
Normalization
1.0
0.8
0.6
0.4
0.2
0.0
1700
1680
1660
1640
1620
1600
Wavenumber (cm-1)
wild type
E22K homo-fibrils
E22K hetero-fibrils
equal-molar-mixed homo-fibrils

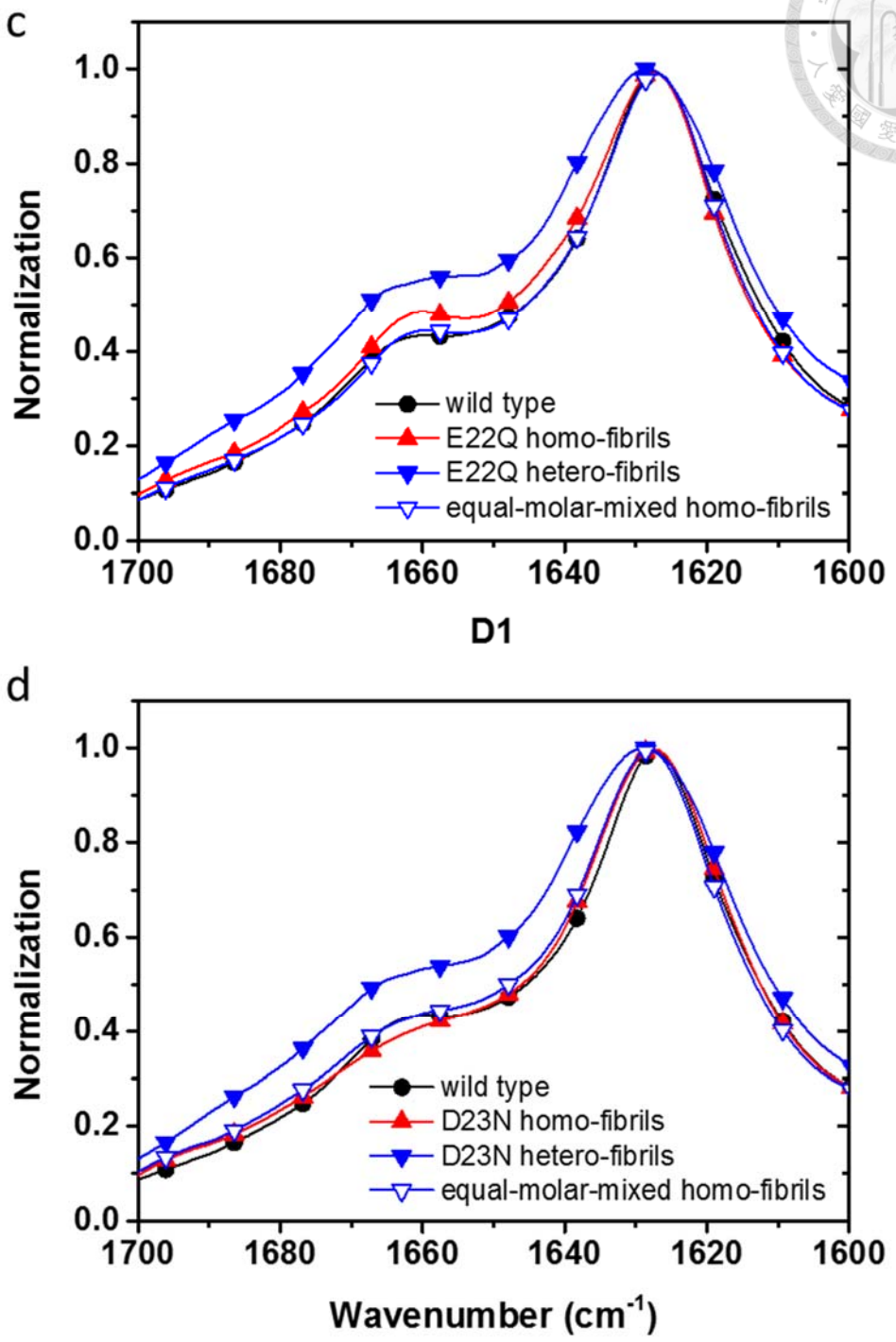

Figure 21. FTIR spectra of FAD homo-fibrils, hetero-fibrils,and equal-molar-mixed homo-fibrils.

4.6 Fluorescence lifetime of bound ThT on fibrils

After complementary spectroscopic examination using CD and FTIR revealed distinction in the secondary structures of fibrils, we turned to the fluorescent probe ThT, exploiting another property of fluorescence, fluorescence lifetime. We would like to understand whether the differences in secondary structures can be reported by fluorescence lifetime of ThT. In 2012, Mohanty et al. pioneered in using ThT as a sensitive method to monitor fibrillation of insulin in the pre-fibrillar regime[132]. We processed fibrils for fluorescence lifetime measurement with the same method as used in FTIR experiments. ThT was added to final 5 μM to avoid influence from free dye. Our results showed that for all the homo-fibrils, lifetimes of ThT fluorescence were multiexponential as the decay profiles were non-linear when the photon counts was plotted in log scale (Figure 22a). A detailed analysis of the decay profiles showed that the decay curve for E22K deviated from the rest of spectra (Figure 22b). The decay curves of hetero-fibrils were shown in Figure 23 along with that of wild type fibril. The decay curves varied from each other. Better visualization is strengthened in the zoom-in view in Figure 23b. All decay curves were subjected to fitting analysis using a multiexponential decay model in an attempt to extract lifetimes. ThT binding onto E22K homo-fibrils resulted in two lifetimes, 1.33 ns and 2.38 ns, which were longer than the rest of homo-fibrils (Table 1). Bound ThT on homo-fibrils other than E22K can be classified into two

groups. The first group had a lifetime of ~0.8 ns, and the second group had a longer lifetime, 1.9 ns for E22G, E22Q, and D23N fibrils and 2 ns for wild type fibrils. We found two scenarios in the lifetime changes when we compared that of bound ThT on each FAD hetero-fibrils with corresponding homo-fibrils. The lifetimes of ThT were both prolonged to 1.1 ns and 2.13 ns when binding onto E22G hetero-fibrils. On the contrary, the lifetimes of ThT were shortened when it binds onto E22K, E22Q, and D23N hetero-fibrils. The extent of reduction was observed for E22K.

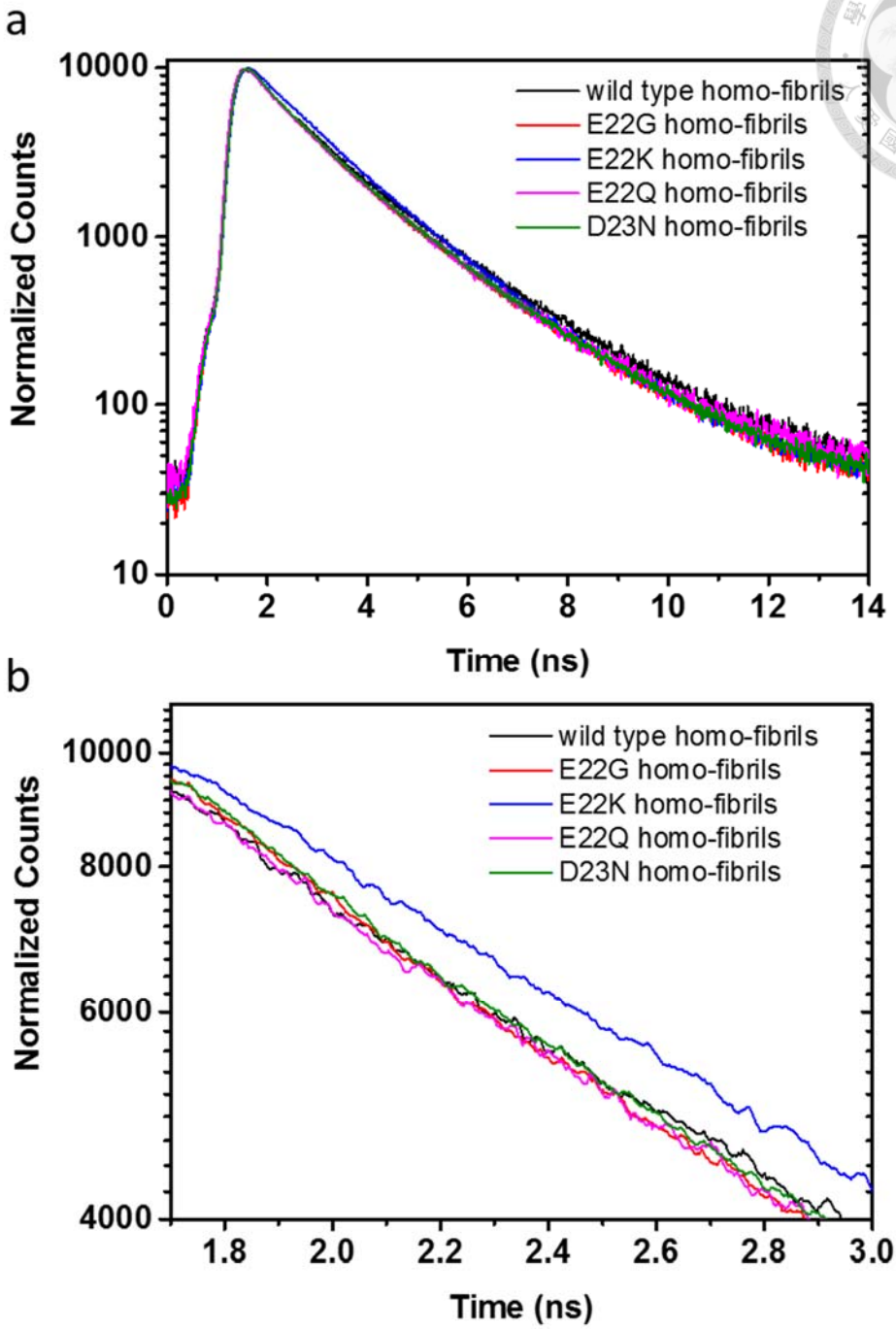

Figure 22. Comparison of ThT fluorescence lifetime for FAD homo-fibrils. (a) full scale and (b) zoom-in of lifetime decay profiles of at least 10 μM fibrils in the presence of 5 μM ThT. Photons were collected for 60 minutes and were normalized to a 0 to 10,000 scale for comparison.

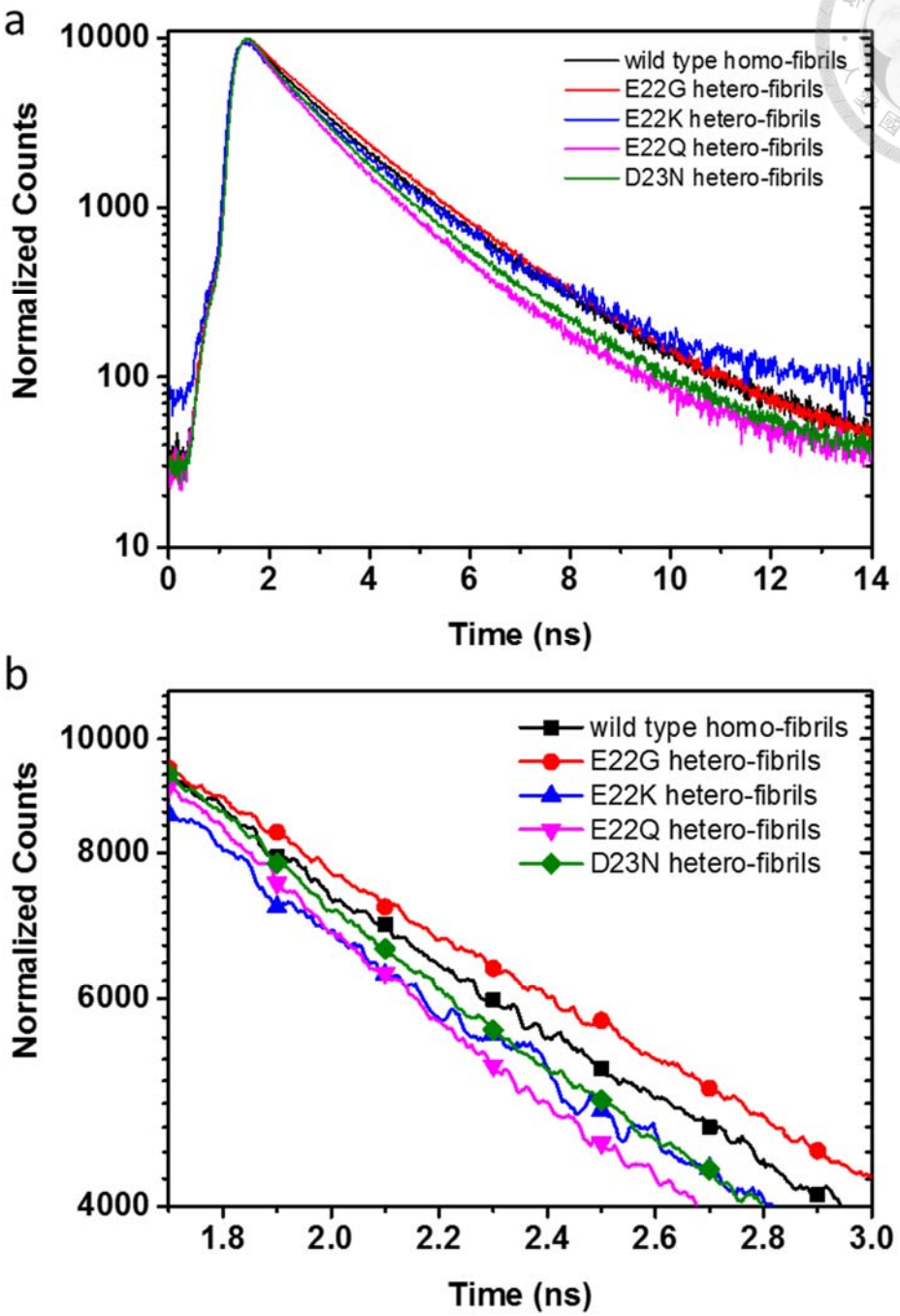

Figure 23. Comparison of ThT fluorescence lifetime for FAD hetero-fibrils. Wild type homo-fibrils data is used for showing how deviated the decay profiles of hetero-fibrils are from the majority of homo-fibrils (except E22K). (a) full scale and (b) zoom-in of lifetime decay profiles of at least 10 μM fibrils in the presence of 5 μM ThT. Photons were collected for 60 minutes and were normalized to a 0 to 10,000 scale for comparison.

Homo-fibrils	τ1 (ns)	τ2 (ns)	R^2	Hetero-fibrils	τ1 (ns)	τ2 (ns)	R^2
Wild type	0.8	1.99	0.99				
E22G	0.75	1.89	0.99	*E22G*	1.1	2.13	0.99
E22K	**1.33**	**2.38**	0.99	*E22K*	0.72	1.94	0.99
E22Q	0.8	1.89	0.99	*E22Q*	0.6	1.66	0.99
D23N	0.8	1.91	0.99	*D23N*	0.69	1.79	0.99

Table 1. Summary of lifetimes of ThT upon binding to amyloid fibrils.

Chapter 5 Interactions of Cu^{2+} with wild type and N-terminal familial mutants of Aβ

5.1 Aims

In this chapter, we emphasized on N-terminal mutations of Aβ associated with three types of FAD, H6R, D7N, and D7H. As H6 and D7 mutations occur at the residue either validated to bind directly to Cu^{2+} in coordination or sitting next to it, we asked whether mutations perturb integrity of Cu^{2+} binding and how residue replacement affect the extent of the perturbation. We used stopped-flow fluorescence, intrinsic fluorescence, Bis-ANS fluorescence, proton NMR spectroscopy, and ^{1}H-^{15}N HSQC NMR spectroscopy to provide insights of Cu^{2+} binding to the three disease-related FAD variants. Two other non-disease-related variants H6A and D7A were included to increase residue diversity.

5.2 Metal ion binding examined by stopped-flow fluorescence.

The stopped-flow apparatus monitoring total quantum yield of tyrosine fluorescence was employed to acquire the binding kinetics of the metal ions and 12.5 μM Aβ40 (Figure 24).

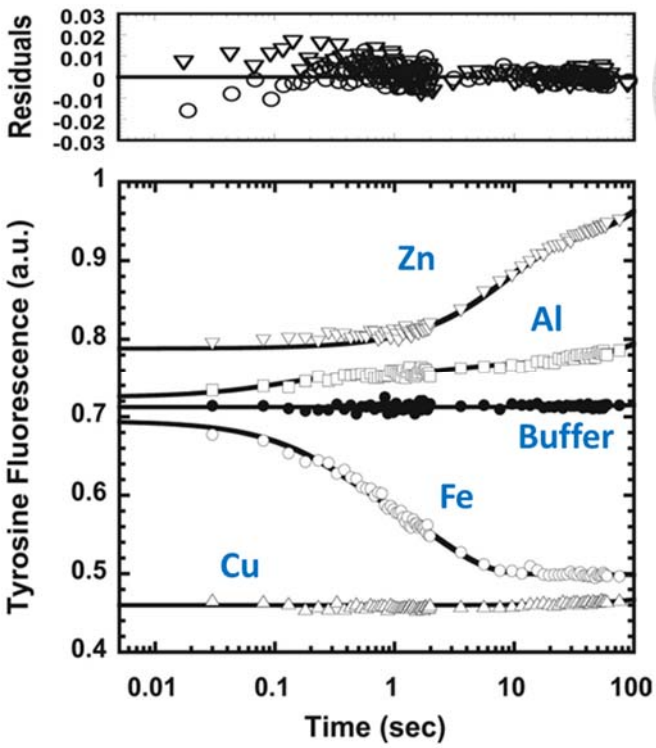

Figure 24. Binding kinetics of Zn^{2+}, Cu^{2+}, Fe^{3+}, and Al^{3+} with Aβ40. The reaction was 12.5 μM Aβ40 and 1.25 mM metal ions performed using stopped-flow. Aβ40 monomers were prepared in 10 mM Tris, pH 7.4. Tyrosine fluorescence changes was recorded within 5 min, and was presented the first 100 s.

The final metal ion concentration was 100 times more than that of Aβ. The ThT fluorescence intensity was monitored from the instrumental dead time, ~5 ms, up to 100 s. The control experiment of Aβ mixing with Milli-Q had no fluorescence intensity change in 180 seconds, suggesting no conformational changes occurred during the time span. When Aβ mixed with the metal ions, the intensity signals showed exponential increases for Zn^{2+} and Al^{3+}, whereas the signals decayed exponentially for Fe^{3+}. The

signals for Cu^{2+} had no significant change after 5 ms. However, we noticed that the initial detectable ThT signals was drastically decreased compared to other curves. The offset of Zn^{2+} was elevated, consistent with the baseline elevation in the steady state spectra. The offset changes for Al^{3+} and Fe^{3+} were relatively small compared to fluorescence intensity changes indicative of metal ion binding occurring beyond 20 ms in both cases. Overall, the amplitude changes of tyrosine intensity signals were consistent with the changes observed in the steady state spectra[133], where Zn^{2+} and Al^{3+} increased the fluorescence, but Fe^{3+} and Cu^{2+} quenched the fluorescence. The data were fitted to exponential equations with a linear baseline assuming the metal ion binding events are pseudo-first-order reactions. Fe^{3+} and Al^{3+} were best fitted to two exponential equations, whereas Zn^{2+} was best fitted to a single exponential equation. Two exponential equation has two binding constants and single exponential equation has one binding constant. Therefore, the number of binding constants can be accounted for the stoichiometry between Aβ and metal ions. Our results suggested that the stoichiometry is 1:1 for Zn^{2+}/Aβ and Cu^{2+}/Aβ, and 2:1 for both Fe^{3+}/Aβ and Al^{3+}/Aβ. In contrast to Zn^{2+}, Fe^{3+}, and Al^{3+}, Cu^{2+} had nearly no signal change after the dead time, indicating that the binding events were likely completed before the instrumental dead time 5 ms. Therefore, we proposed the order of binding from the fastest to the slowest was Cu^{2+} (sub-milliseconds) > Al^{3+} (k_1 = 6.067 s^{-1} 1, τ = 0.114 s) > Fe^{3+} (k_1 = 3.455 s^{-1} 1, τ = 0.20 s) > Zn^{2+} (k_1 = 0.124 s^{-1}, τ = 5.553 s). The

observed offset could be due to sub-millisecond binding events or environmental effects altering the tyrosine quantum yield. In the case of Zn^{2+}, because the fitting precisely described the events from 0.005 to 100 s, and the elevation was also observed in the steady state spectra. We reasoned that the elevation is not due to a binding event.

5.3 Intrinsic fluorescence of H6 and D7 mutants upon Cu^{2+} binding

We examined Cu^{2+} binding properties of six Aβ peptides, wild type, three D7 mutants, and two H6 mutants. We exploited the proximity of Y10 to the mutated residue, H6 or D7, to report conformational changes of Aβ peptides induced by metal ion binding. Consistent with our published data[133], tyrosine fluorescence intensities of wild type Aβ was quenched upon titration with Cu^{2+} due to its paramagnetic properties[134]. In the absence of Cu^{2+}, emission peak situated at 300 nm for all Aβ (Figure 25). Overall, fluorescence intensities for wild type and D7 mutants were higher than that of H6 mutants possibly due to higher quantum yield. In the presence of eight molar equivalent Cu, tyrosine fluorescence was quenched at least two-fold.

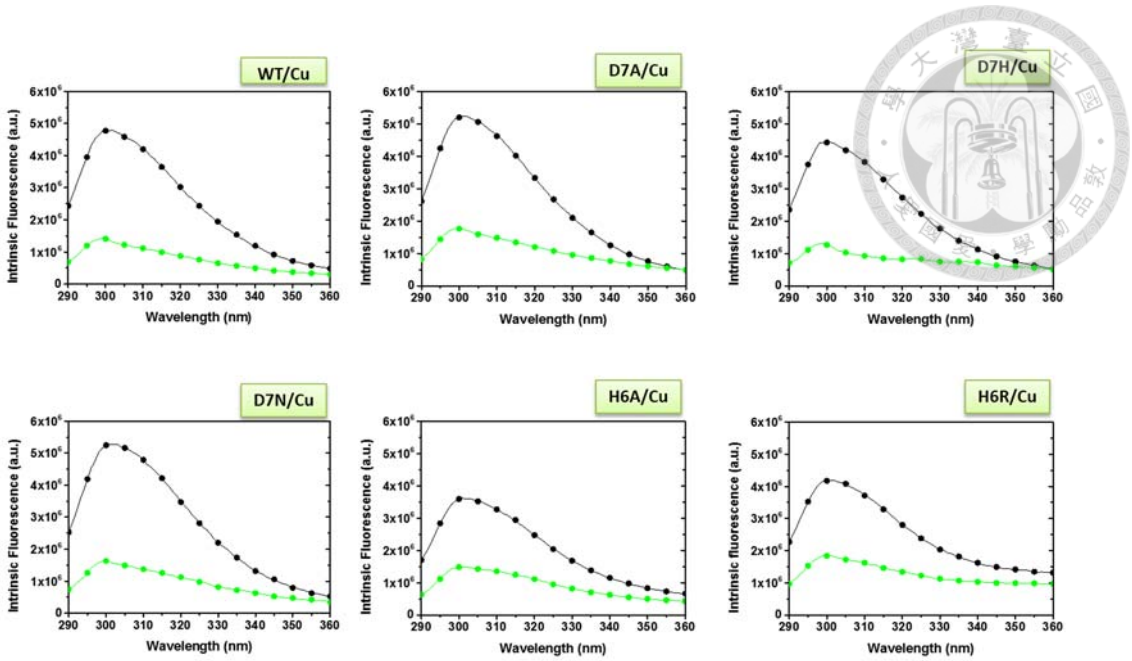

Figure 25. Tyrosine emission spectra of wild type, H6, and D7 mutant Aβ. The spectra for each peptide in the absence (black) and presence (green) of 8 molar equivalent Cu^{2+} are presented. The reactions were such that 25 μM peptide was titrated with up to 8 molar equivalent of Cu^{2+}.

Quenching of tyrosine fluorescence started shortly after Cu^{2+} addition until Cu^{2+} concentration reached close to peptide concentration, 25 μM, in our experiments (Figure 26). Beyond 25 μM, decrease of tyrosine fluorescence slowed down in an exponential way, indicating a weaker quenching. All titration curves of the five FAD mutants showed similar trends. We fit experimental data to a quadratic equation derived from a single protein-ligand interaction model (Eqn. 4),

$$F_{obs} = F_f + (F_i - F_f) \times \frac{\left[(K_d + L_t + P_t) - \sqrt{((K_d + L_t + P_t)^2 - 4 \times P_t \times L_t)}\right]}{2P_t}$$

Eqn. 4

where F_{obs} is the observed fluorescence intensity, F_i and F_f are the initial and final fluorescence intensity recorded in each titration, P_t is the total Aβ concentration, L_t is the total ligand concentration, and K_d is the dissociation constant. Curve fitting gave apparent dissociation constants K_d. Because binding affinity is determined as the inverse of K_d, smaller K_d indicates stronger binding affinity. The dissociation constants derived from curve fitting are listed in Table 2. The K_d of Cu^{2+} binding for wild type Aβ is 9.95 ± 2.84 μM. A quadrupled K_d (39.95 ± 11.72 μM) for H6A indicated the Cu^{2+} binding affinity is reduced four-fold. Substitution of H6 with an arginine residue bearing a charged side chain had negligible impact on Cu^{2+} binding (K_d = 9.8 ± 3.49 μM). Cu^{2+} binding affinity was close to wild type for D7A (K_d = 6.10 ± 2.02 μM), was increased 2.5-fold for D7H (K_d = 3.76 ± 1.1 μM), and was decreased for D7N (15.41 ± 7.19 μM), suggesting an extra histidine strengthen while an asparagine weaken Cu^{2+} binding.

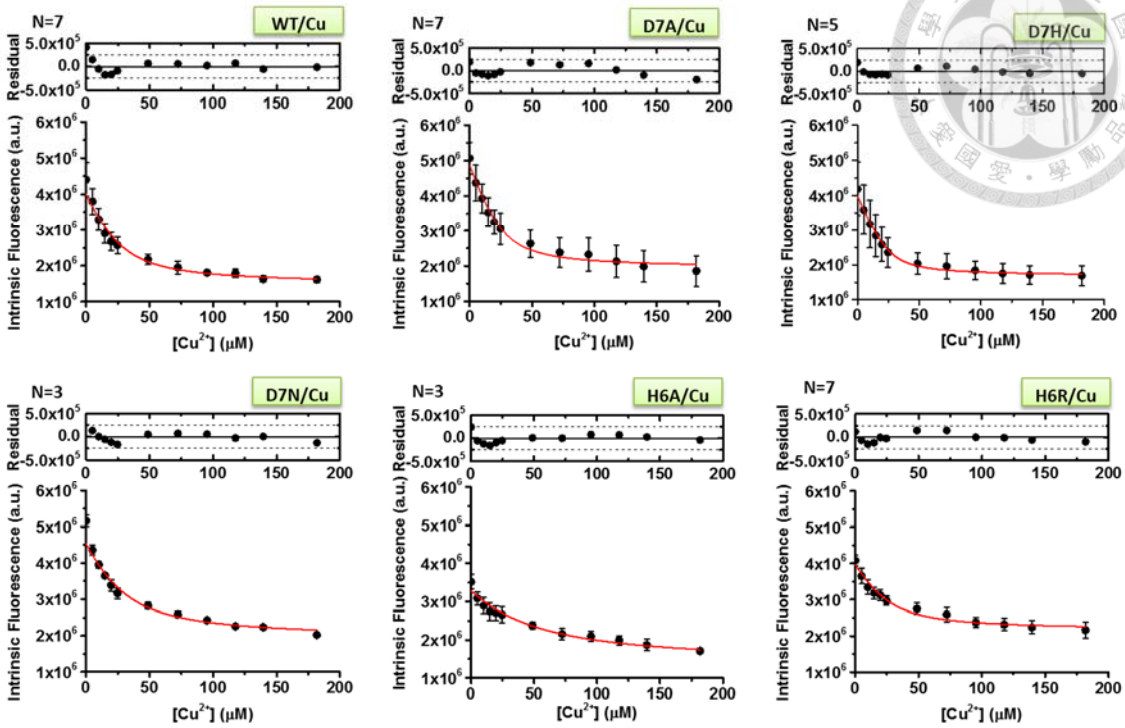

Figure 26. Cu^{2+} titration curves of wild type, H6, and D7 variants of Aβ monitored by tyrosine fluorescence. Twenty-five micromolar of peptide was titrated with up to 8 molar equivalent of Cu^{2+}. Number of replicates used in data averaging are shown at the upper left corner for each figure.

5.4 Bis-ANS fluorescence of H6 and D7 mutants upon Cu^{2+} binding

We attempted to correlate the induced conformational changes with the concomitant exposure of the hydrophobic surfaces formed during Cu^{2+} binding. External fluorescent probe Bis-ANS that binds hydrophobic clusters on protein surface was utilized[135,136]. First, we found that Cu^{2+} binding induced identical blue shift of λ_{max} of Bis-ANS emission but diverse response of Bis-ANS fluorescence intensity for all peptides after eight molar

equivalent Cu^{2+} was added to wild type Aβ (Figure 27). Intensities of Bis-ANS fluorescence for wild type and D7N Aβ remained barely changed after addition of eight molar equivalent of Cu^{2+}. Compared to wild type Aβ, quenching of Bis-ANS fluorescence was found in D7A and D7H. The decrease of intensities were 4-fold for D7A and 2-fold for D7H. Enhancement of Bis-ANS fluorescence was found to be 7-fold for H6R and 2-fold for H6A.

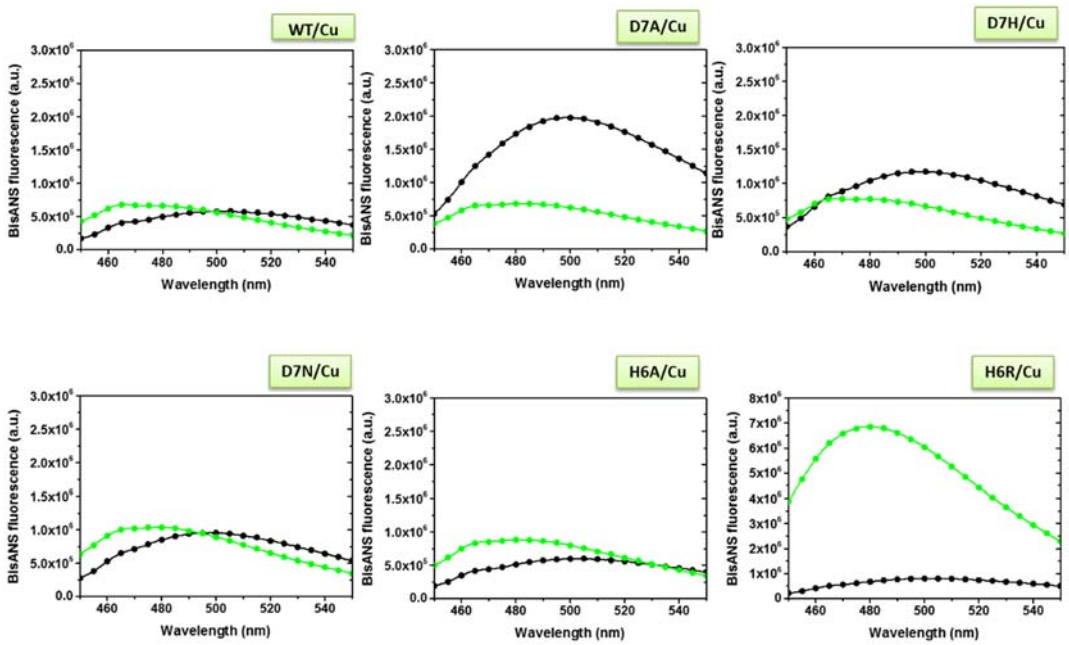

Figure 27. Bis-ANS emission spectra of wild type, H6, and D7 mutant Aβ. The spectra for each peptide in the absence (black) and presence (green) of 8 molar equivalent Cu^{2+} are presented. The reactions were such that 25 μM peptide was titrated with up to 8 molar equivalent of Cu^{2+} in the presence of 5 μM Bis-ANS.

After we performed baseline correction by subtracting each spectrum with corresponding control one, declining titration curves were present by plotting fluorescence intensity against Cu^{2+} concentration (Figure 28). The apparent dissociation constants of Cu^{2+} binding after curve fitting to the same equation used is Chapter 5.3. However, this attempt yielded greater values of standard deviation than that of dissociation constants for several variants. The curves for H6A (K_d = 12.59 ± 5.48 μM) and D7N (K_d = 5.36 ± 2.30 μM) are better fitted as evidenced by the R^2 values 0.967 and 0.972, respectively. The K_d values are more ill-defined for wild type (2.22 ± 3.34 μM) and D7H (4.9 ± 6 μM). The single-ligand binding equation (Eqn. 4) is not applicable to the D7A and H6R curves.

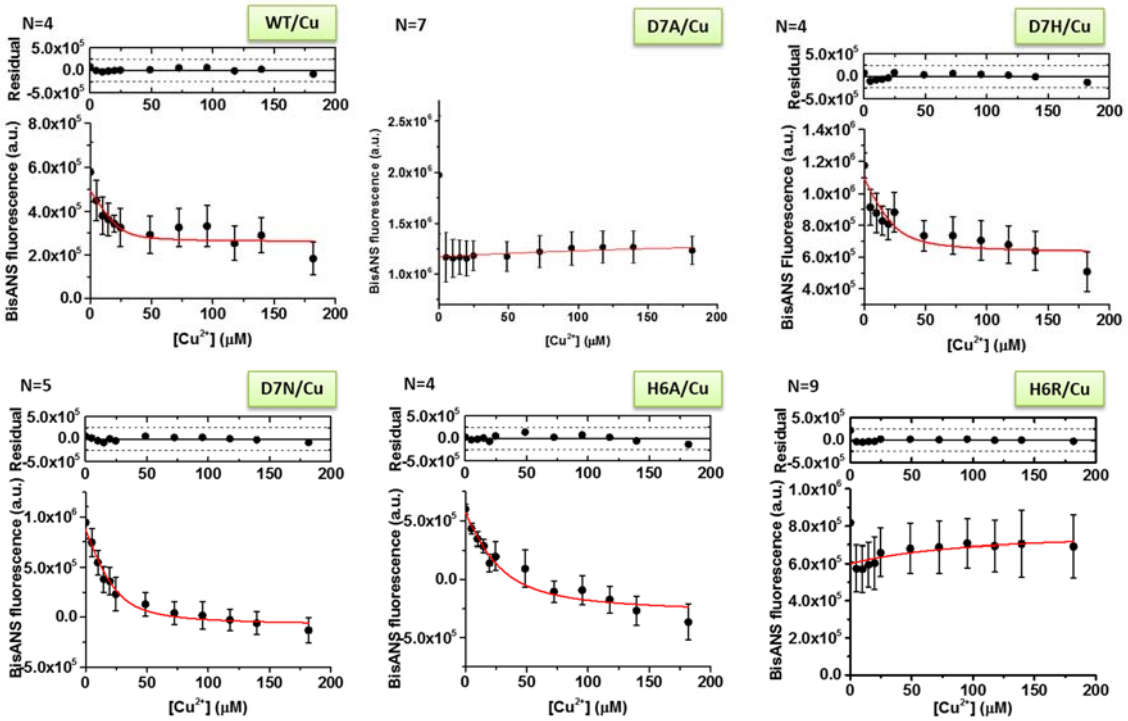

Figure 28. Cu^{2+} titration curves of Aβ monitored by BisANS fluorescence. The spectra for each peptide in the absence (black) and presence (green) of 8 molar equivalent Cu^{2+} are presented. The reactions were such that 25 μM peptide was titrated with up to 8 molar equivalent of Cu^{2+} in the presence of 5 μM Bis-ANS.

K_d from intrinsic fluorescence		*K_d* from Bis-ANS fluorescence	
WT	9.95 ± 2.84 μM	**WT**	2.22 ± 3.34 μM
D7A	6.10 ± 2.02 μM	**D7A**	N.A.
D7H	3.76 ± 1.1 μM	**D7H**	4.9 ± 6 μM
D7N	15.41 ± 7.19 μM	**D7N**	5.36 ± 2.30 μM
H6A	39.95 ± 11.72 μM	**H6A**	12.59 ± 5.48 μM
H6R	9.8 ± 3.49 μM	**H6R**	N.A.

Table 2. Summary of dissociation constants K_d extracted from curve fitting of data from intrinsic tyrosine and Bis-ANS fluorescence.

5.5 ^{1}H NMR spectroscopy

We provided complementary and supporting evidence using NMR spectroscopy to substantiate our findings from intrinsic fluorescence. Proton (^{1}H) NMR Experiments were performed in 10 mM Tris buffer containing 90 % D_2O, pH 7.4, at 5 °C. We focused on the region around 6 – 8 ppm representing hydrogens of C-H bonds on the side chains of Y10 and H6, H13, and H14 histidines. To circumvent potential discrepancy caused by Aβ preparation method, we prepared peptide using GdnHCl method instead of the commonly used NaOH method[137]. In addition, we were concerned that high Aβ concentration such as 75 μM and 130 μM used by other groups could interfere measurement due to aggregation-prone propensity of Aβ. On the other hand, the time needed to accumulate sufficient data for a spectrum is concentration-dependent. Lower peptide concentration takes longer data acquiring time, which, in our titration experiments, increases chances that monomeric peptide nucleates into oligomeric species. Therefore, after taking the concentration and spectra-acquiring time into account, we decided to perform ^{1}H and HSQC NMR measurement with 50 μM of peptide. We confirmed that the GdnHCl preparation method produced proton NMR spectrum was similar to the previously reported ones using NaOH method (Figure 29). Peaks were assigned according to published data by Syme et al.[82,138], and Hou et al.[139]. We assigned the peaks around 7.8

ppm (H6/H13/H14 peaks in Figure 29d) as εH resonances, and peaks around 7.0 ppm (H6 and H13/H14 peaks in Figure 29d) as δH.

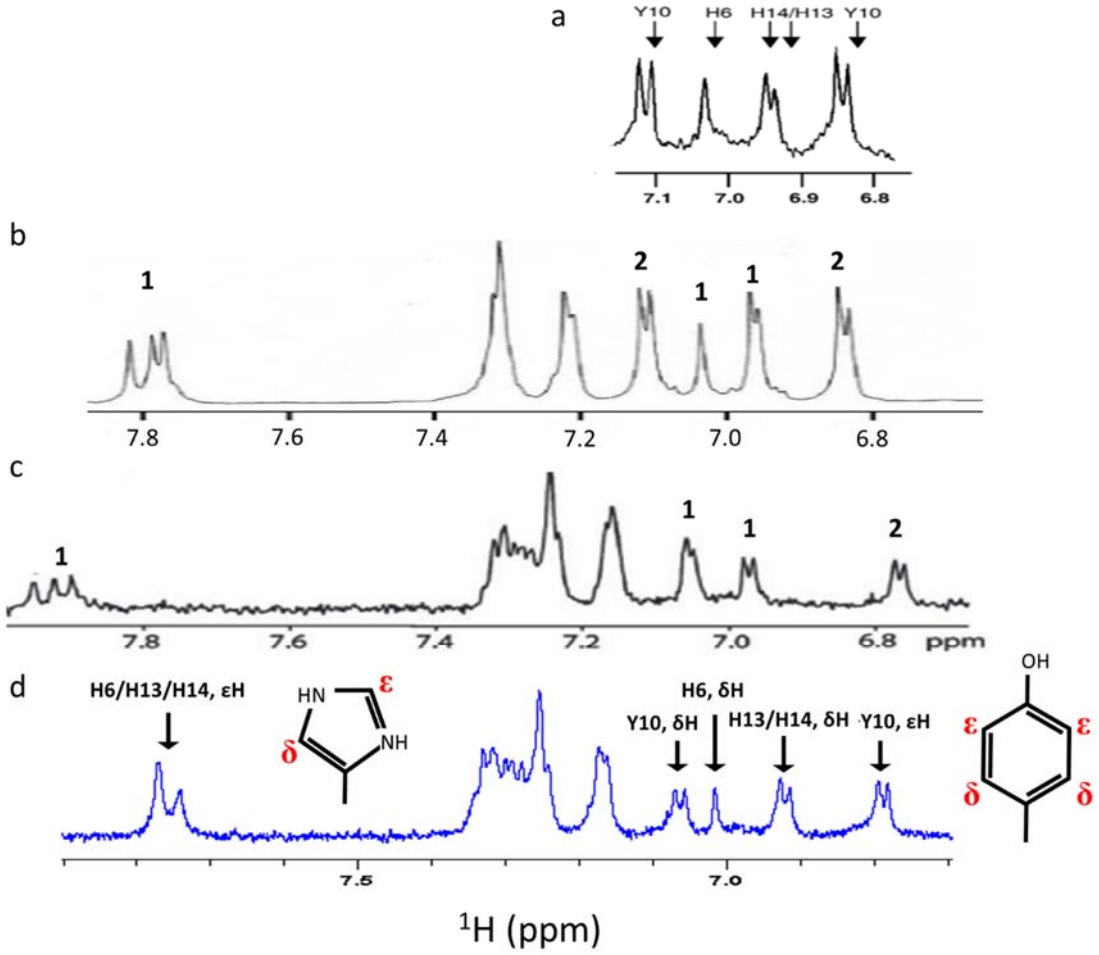

Figure 29. Aromatic region in the ^{1}H NMR spectra of wild type Aβ40. (a) Peak assignment adapted from ref. 81. The experimental conditions are 77 μM Aβ(1-28) in 100 % D_2O, pH 7.8 at 25 °C. (b) Peak assignment adapted from ref. 136, where 1 designates εH and δH from H6, H13, and H14, and 2 designates Y10. The experimental conditions are 1,000 μM Aβ(1-16) in 100 % D_2O, pH 7.4 at 25 °C. (c) Peak assignment adapted from ref. 81, where 1 designats εH and δH from H6, H13, and H14, and 2 designates Y10. The experimental conditions are 130 μM Aβ40 in 5 mM potassium phosphate buffer in D_2O, pH 7.3 at 5 °C. (d) Peak assignment in our spectra based on (a-c). The experimental conditions are 50 μM Aβ40 in 10 mM Tris buffer in 90 % D_2O,

pH 7.4, at 5 °C. The left inset shows the εH and δH on the aromatic ring of histidine. The right inset shows the εH and δH on the aromatic ring of tyrosine.

We compared ^{1}H NMR spectra of six Aβ peptides in the absence of Cu^{2+} (Figure 30). Five regions were highlighted in boxes except for region 3. The peaks of Y10 in Box 1 and 4 had the largest upfield chemical shift to the right for D7A than for other peptides. Besides, we noticed that D7 variants had peak broadening effect in Y10 peaks. In Box 2, the H13/H14, δH peaks underwent an upfield chemical shift for D7A, D7N, H6A, and a downfield shift for D7H. In Box 5, two H6/H13/H14, εH peaks were found for all peptides except D7H, which had extra peaks. Upfield shift were observed for D7N and H6 variants, and a slight downfield shift was seen in D7A. The unboxed region 3 disclosed a greater extent of upfield shift of H6, δH peaks for D7H and D7N, and loss in H6 variants. The peaks around 7.3 ppm could mainly come from the three phenylalanine residues. Taken together, alteration in H6 and D7 residues led to chemical shifts of certain specific peaks in ^{1}H NMR spectra.

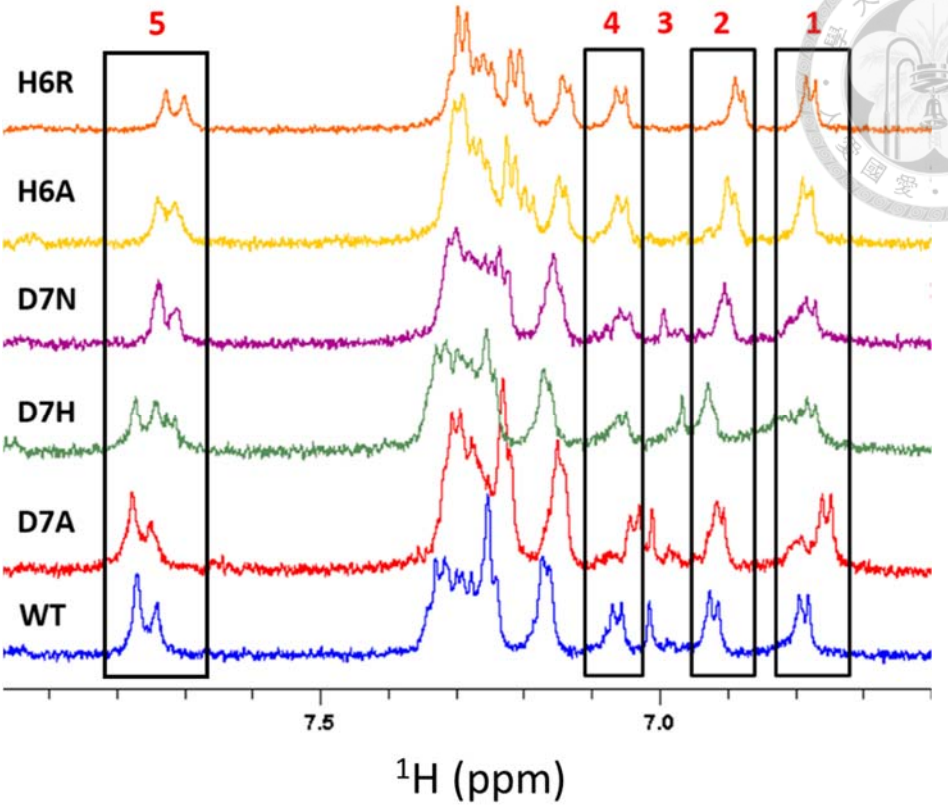

Figure 30. Comparison of ^{1}H NMR spectra of wild type Aβ and its H6 and D7 variants in the absence of Cu^{2+}. NMR measurement was performed in 50 μM peptide buffered in 10 mM Tris containing 90 % D_2O, pH 7.4, at 5 °C.

We performed a series of Cu^{2+} titration using NMR spectroscopy for all six Aβ peptides. We found that addition of Cu^{2+} caused severe signal intensity reduction which could result from peak broadening. Y10 and histidine signals vanished after 0.8 molar equivalent Cu^{2+} was titrated. The signal reduction profile of wild type Aβ was shown in Figure 31. Similar profiles was observed for all peptides in this study (data not shown). The decrease in H6 and H13/H14, δH peaks, and Y10 peaks were plotted against the titrated Cu^{2+}

concentration (Figure 32). To acquire peak intensities at a better signal-to-noise ratio, we implemented 400 scans in titration experiments. Attempts to fit experimental results to a single-ligand binding model were not shown due to unsuccessful fitting results. We found that the peak intensities of H6 and H13/H14, δH remained above 20 % of the initial intensities after ~37 μM (0.8 molar equivalent) Cu^{2+} were titrated, while for the rest of the peptides these two peaks reduced to the lowest level at the same Cu^{2+} concentration. The titration curve of Y10 intensities for D7H deviated from H6 and H13/H14, δH ones and was also distinct from that for others peptides in study, suggesting that in D7H the Y10 is surrounded in a different environment due to the existence of the extra histidine.

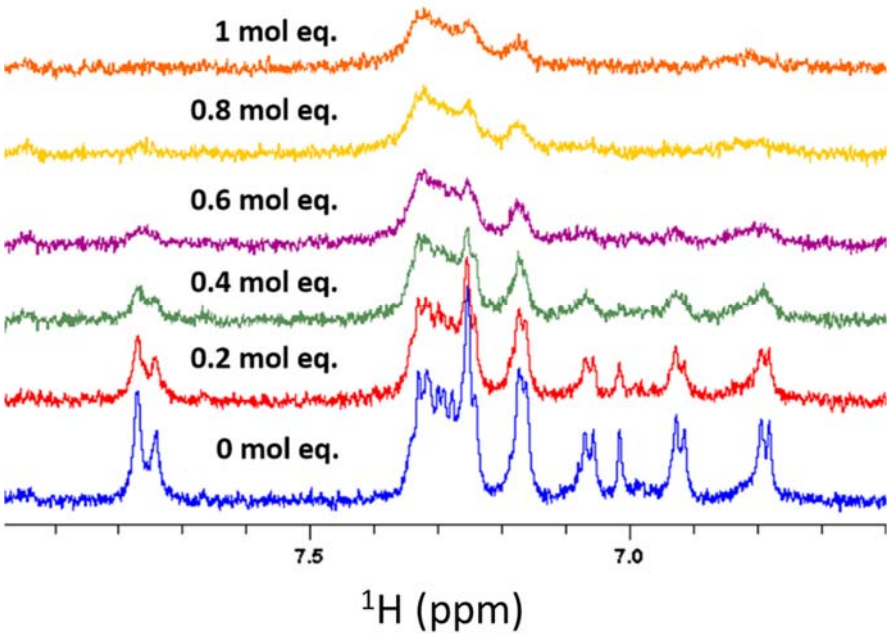

Figure 31. Peak broadening around aromatic region during Cu^{2+} titration of wild type Aβ40. Fifty micromolar of peptide was buffered in 10 mM Tris, pH 7.4. Cu^{2+} were titrated up to two molar

equivalent of Aβ40. Dilution effect was factored in to reach precise molar ratio. NMR measurement was performed at 5 °C.

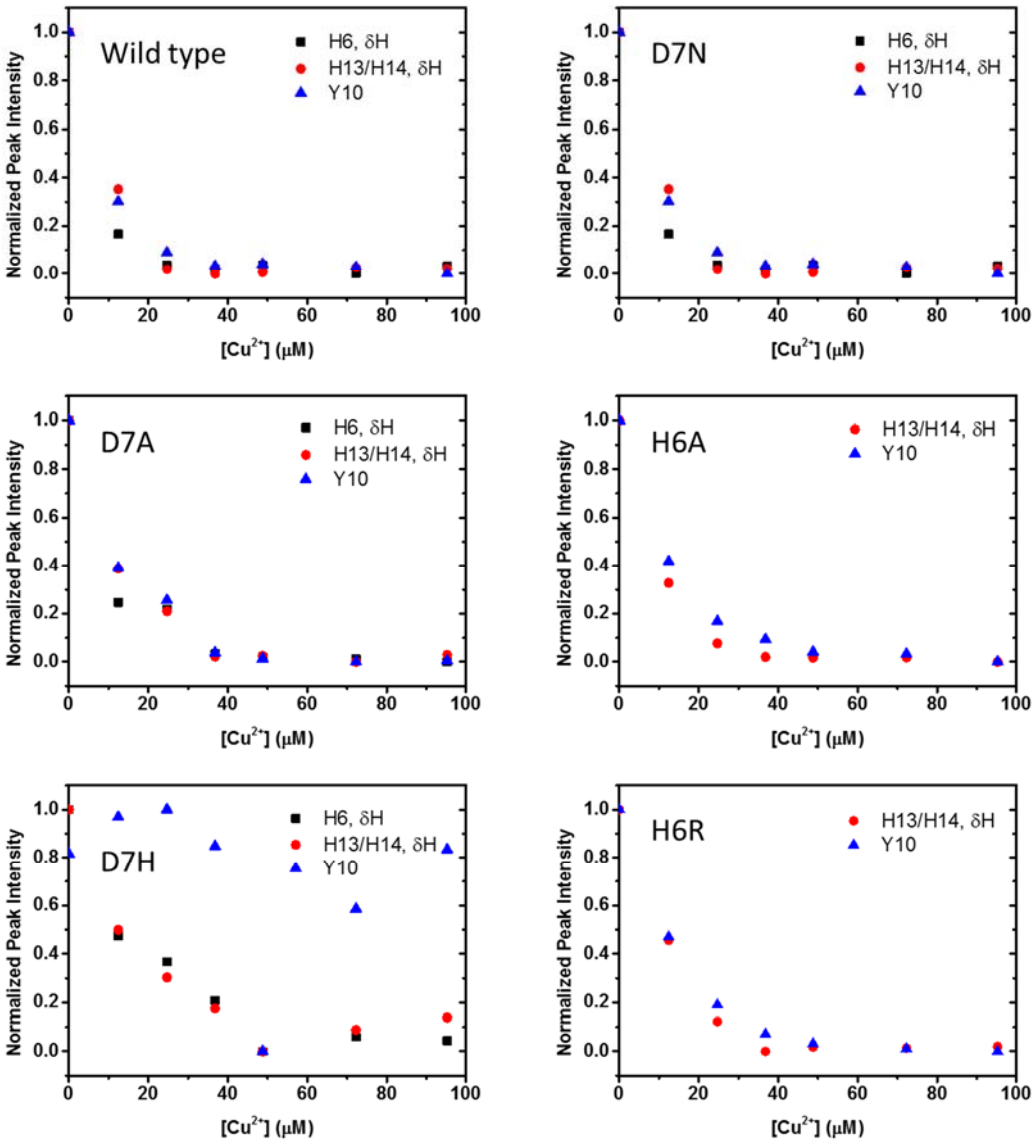

Figure 32. Reduction of H6 and H13/H14, δH peaks, and Y10 peaks for H6 and D7 variants of Aβ. Fifty micromolar of peptide was buffered in 10 mM Tris, pH 7.4. Cu^{2+} were titrated up to two molar equivalent of Aβ40. Dilution effect was factored in to reach precise molar ratio. NMR measurement was performed at 5 °C.

5.6 ^{1}H-^{15}N HSQC spectroscopy of D7H and wild type Aβ

As experimental evidence strongly implicated the involvement of the three histidines H6, H13, and H14 in Cu^{2+} coordination, we were especially interested in whether and how an additional histidine, as in the case of an early-onset AD mutant D7H, impact Cu^{2+} coordination. We employed recombinant 15N labeled wild type and D7H Aβ peptides in titration experiments using ^{1}H-^{15}N HSQC spectroscopy. We showed that Aβ prepared by GdnHCl method had a similar 2D spectrum as reported[139] (Figure 33).

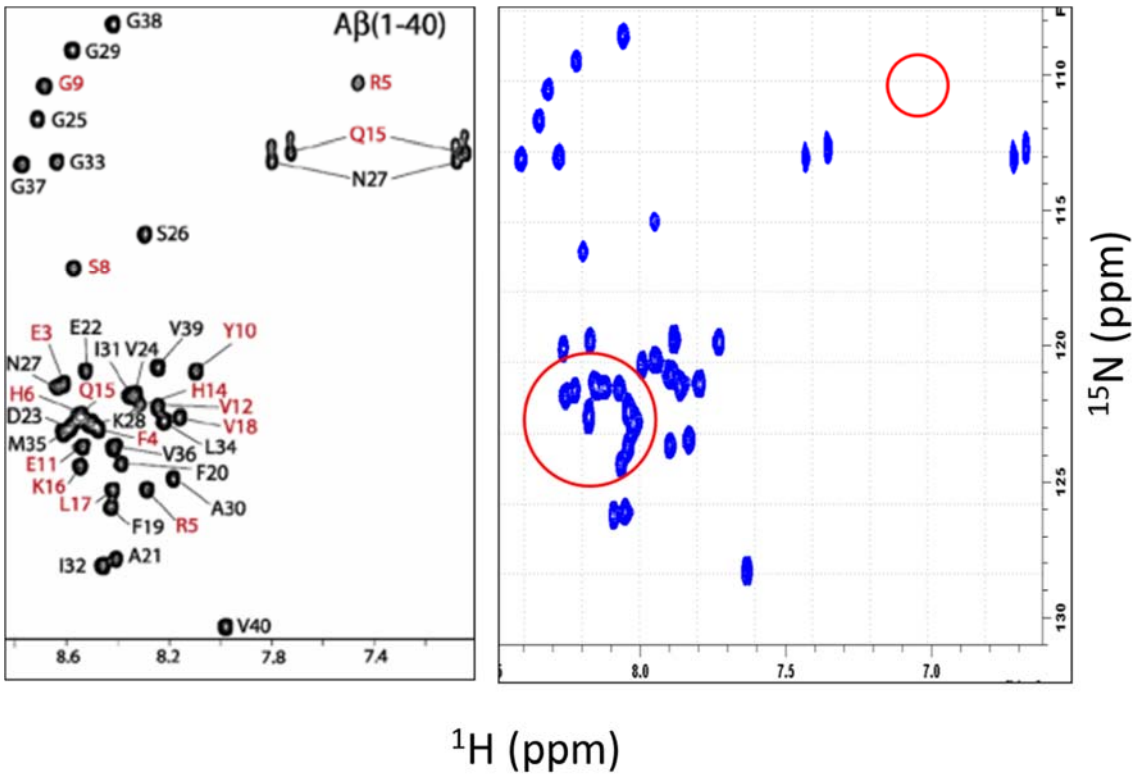

Figure 33. Comparison of ^{1}H-^{15}N HSQC NMR spectrum from Zagorski's and our group. (Left panel) The spectrum of wild type Aβ40 reported by Hou et al.[139]. (Right panel) The spectrum of wild type Aβ40 obtained in our lab. Peptide concentration was 130 μM in Hou et al.'s experiment and was 50 μM in ours. Red circles indicate major spectral difference between Hou

et al.'s results and ours. Our NMR measurement was performed with peptide buffered in 10 mM Tris containing 10 % D_2O, pH 7.4, at 5 °C.

Because we did not perform peak assignment experiments, peaks in our spectrum were assigned based on the one reported by Hou et al.[139] (left panel, Figure 33) Red circle marked the evident differences, which possibly was caused by different peptide preparation, buffer system, or peptide concentration used in measurements.

Compared to the spectrum of wild type Aβ, spectrum of D7H showed displaced F4, G9 and K16 peaks, and vanished R5, S8, and K28 peaks (Figure 34). One molar equivalent Cu^{2+} induced peak disappearance in mostly N-terminal (1-16) residues in both wild type Aβ (Figure 35). Disappearing peaks are highlighted in red. A parallel control experiments in which metal ion buffer was titrated in the same manner into Aβ. Very similar peak disappearance pattern was also observed for D7H upon one molar equivalent Cu^{2+} addition (right panels in Figure 35a and b). After two molar equivalent Cu^{2+} was titrated, comparable peak intensity seen in Figure 35 underwent slightly different changes. F20 and D23 peaks completely disappeared in the D7H spectrum, but not wild type one (Figure 36). Ratio of intensity from Cu^{2+} titration and buffer control experiments for each peak was plotted in Figure 37. Peak reduction pattern of overall residues clearly showed that Cu^{2+} binding occurred at the N-terminal region (residue 1-17) of Aβ.

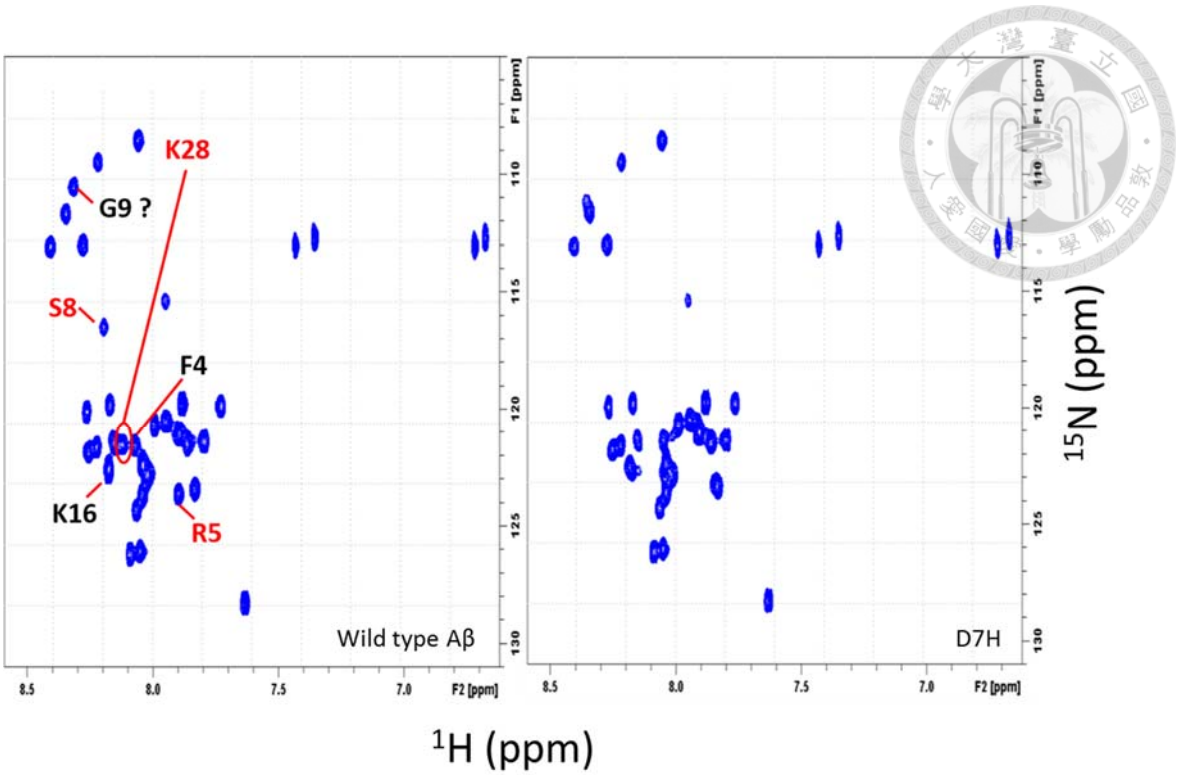

Figure 34. Comparison of ^{1}H-^{15}N HSQC spectra from wild type and D7H Aβ. (Left panel) Wild type Aβ. (Right panel) D7H Aβ. Red color indicate vanishing residues and black color indicate displaced residues. Our NMR measurement was performed with peptide buffered in 10 mM Tris containing 10 % D_2O, pH 7.4, at 5 ºC.

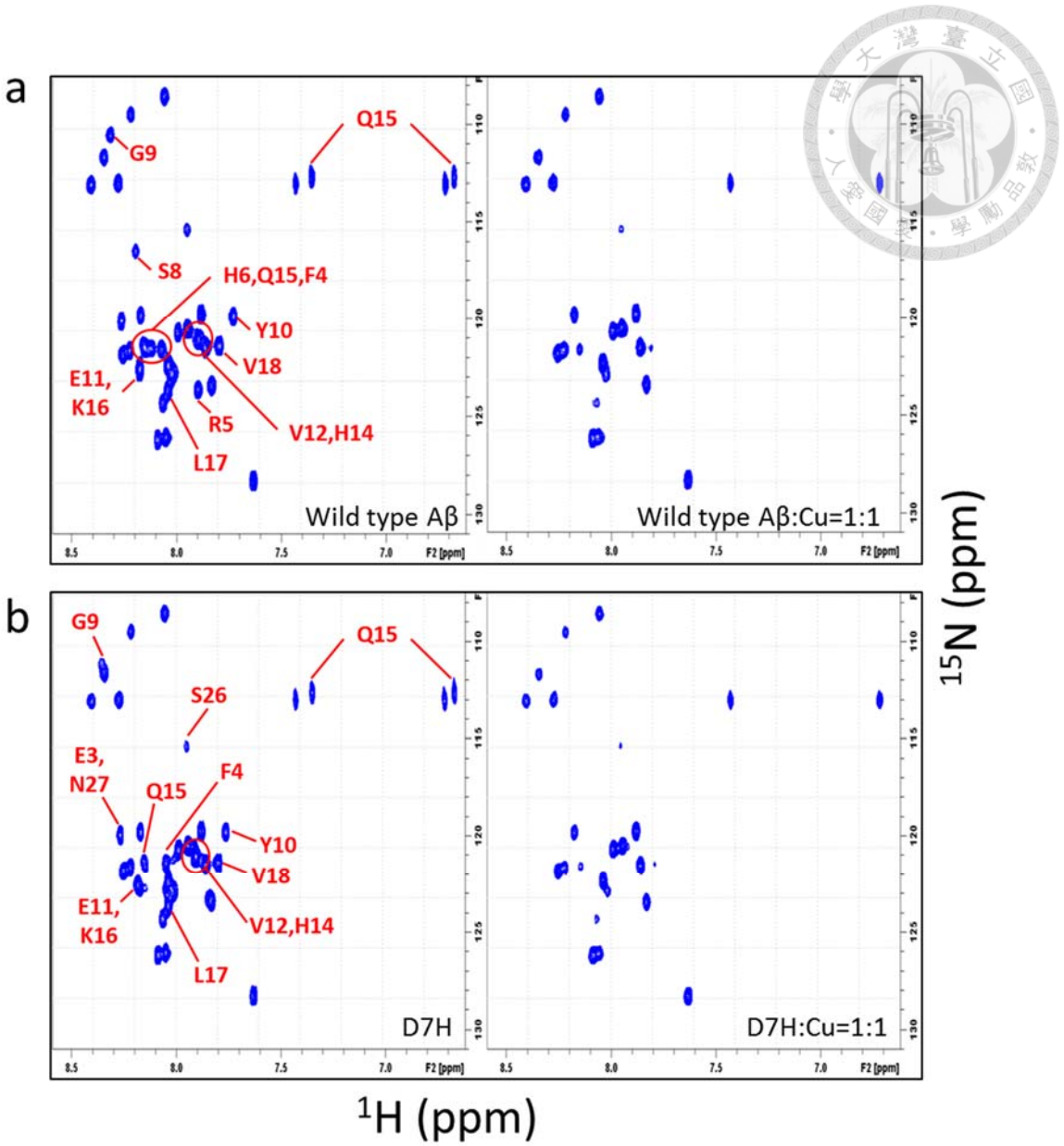

Figure 35. ^{1}H-^{15}N HSQC spectra of peptide in the presence of one molar equivalent Cu^{2+}. (a) Wild type and (b) D7H Aβ. Single-letter amino acid codes with number in red indicate vanishing residues. NMR measurement was performed with peptide buffered in 10 mM Tris containing 10 % D_2O, pH 7.4, at 5 ºC.

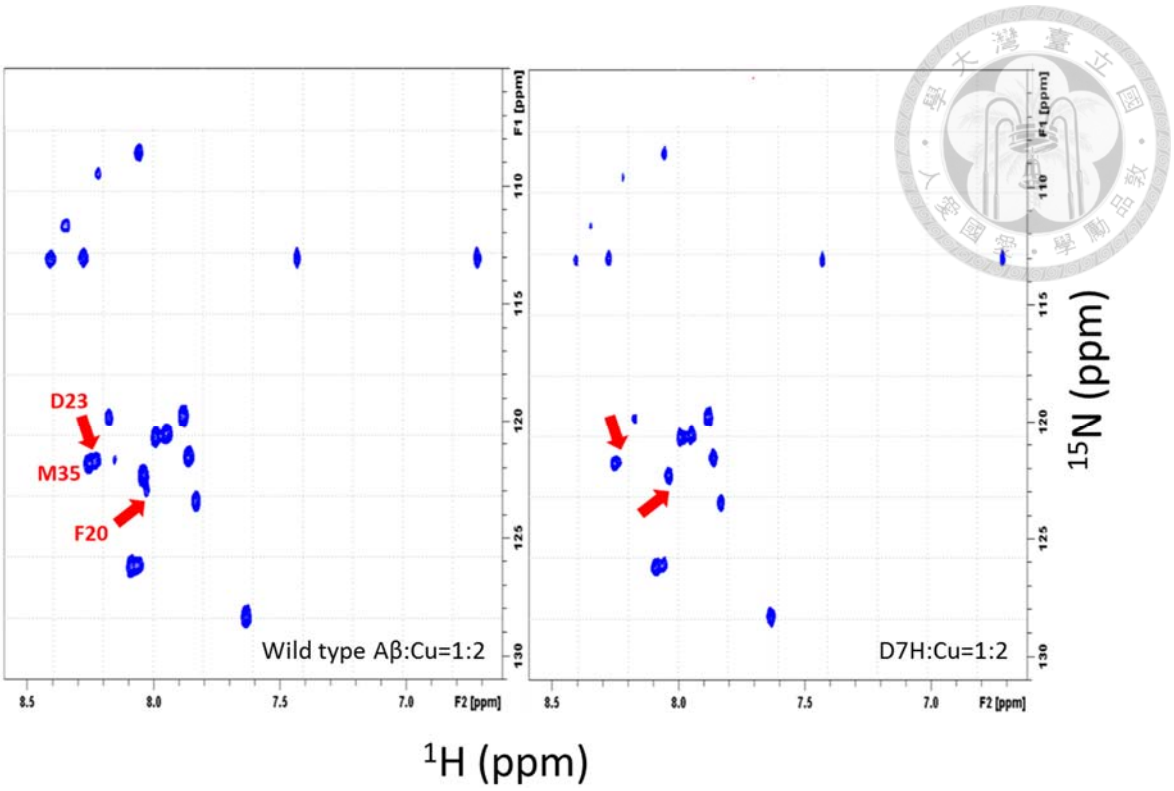

Figure 36. ^{1}H-^{15}N HSQC spectra of peptide in the presence of two molar equivalent Cu^{2+}. (Left panel) Wild type and (Right panel) D7H Aβ. Single-letter amino acid codes with number in red indicate vanishing residues. NMR measurement was performed with peptide buffered in 10 mM Tris containing 10 % D_2O, pH 7.4, at 5 ºC.

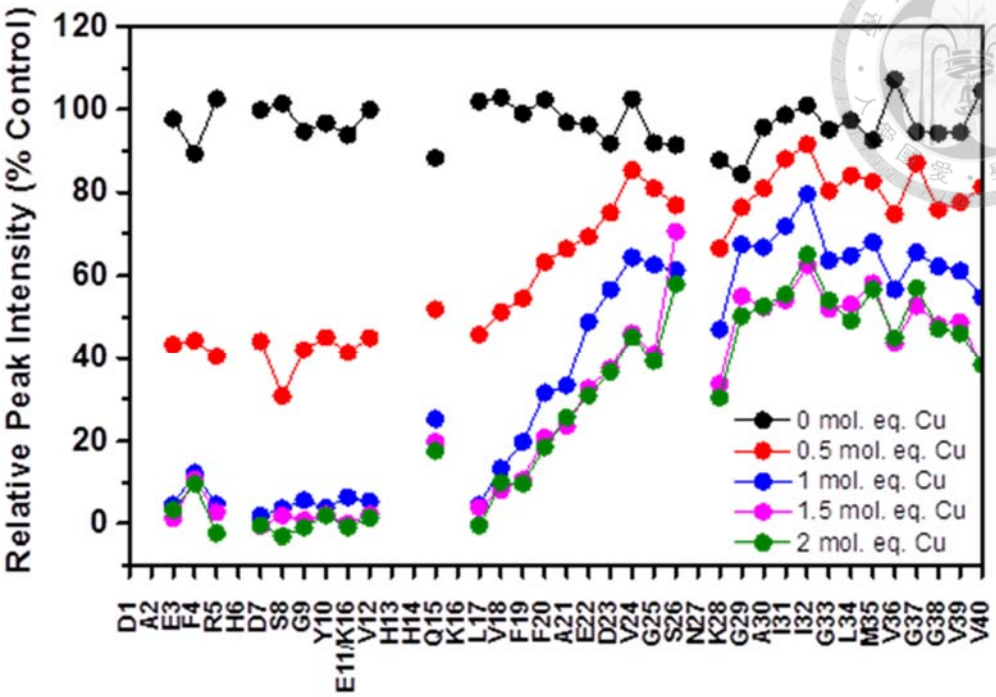

Figure 37. Relative NH peak intensities obtained from ^{1}H-^{15}N HSQC spectra with different amounts of Cu^{2+}. The omitted intensities are due to spectral overlap or rapid solvent exchange. Single-letter amino acid codes with numbers are used to designate residues. NMR measurement was performed with peptide buffered in 10 mM Tris containing 10 % D_2O, pH 7.4, at 5 ºC.

Chapter 6 Discussion

6.1 Negatively Charged Gold Nanoparticles Inhibit Alzheimer's Amyloid-β Fibrillization, Induce Fibril Dissociation, and Mitigate Neurotoxicity

6.1.1 Results of various effects imposed by AuNPs on Aβ

We focused on understanding the effect of the most biocompatible nanoparticles, AuNPs, on Aβ in AD using 30 nm AuNPs. First, ThT experiments showed that bare AuNPs were able to inhibit Aβ fibrillization and initiated fibril alteration as evidenced from the low end-point ThT fluorescence intensities. ThT fluorescence resulting from its binding to amyloid fibrils in parallel with the fibril axis is an indicator of the amount and length of the fibrils[123,140]. Changes in quantity and/or morphology of fibrils could result in fewer ThT binding sites leading to lower ThT intensity. The result was further confirmed by morphological examination by TEM showing generation of shorter, fragmented fibrils and spherical oligomers as well as DLS analysis in which large fibrils (> 100 nm) dominating the scattered lights were significantly reduced to smaller species (< 100 nm). The phenomenon is closely related to the surface charges of the AuNPs since the fibril inhibition effect was only observed in the negatively charged AuNPs. Cytotoxicity assays conducted by one of our lab member showed that the resulting short fibrils and oligomers revealed reduced neurotoxicity to the neuroblastoma N2a cells in comparison to those treated with mature Aβ fibrils formed in the absence of AuNPs. The

rescue effect was only seen in those incubated with negatively charged AuNPs (Figure S1 in Supplementary data). Taken together, we illustrated results from our experiments in Figure 38. The results suggested that the negatively charged AuNPs in nanomolar range can potentially serve as rescuing molecules like chemical chaperones to prevent cell death caused by those detrimental Aβ species. Although AuNPs-altered preformed fibrils were still as toxic as the mature ones, the specificity of bare AuNPs toward mature Aβ fibrils implicates a diagnostic potential in the future.

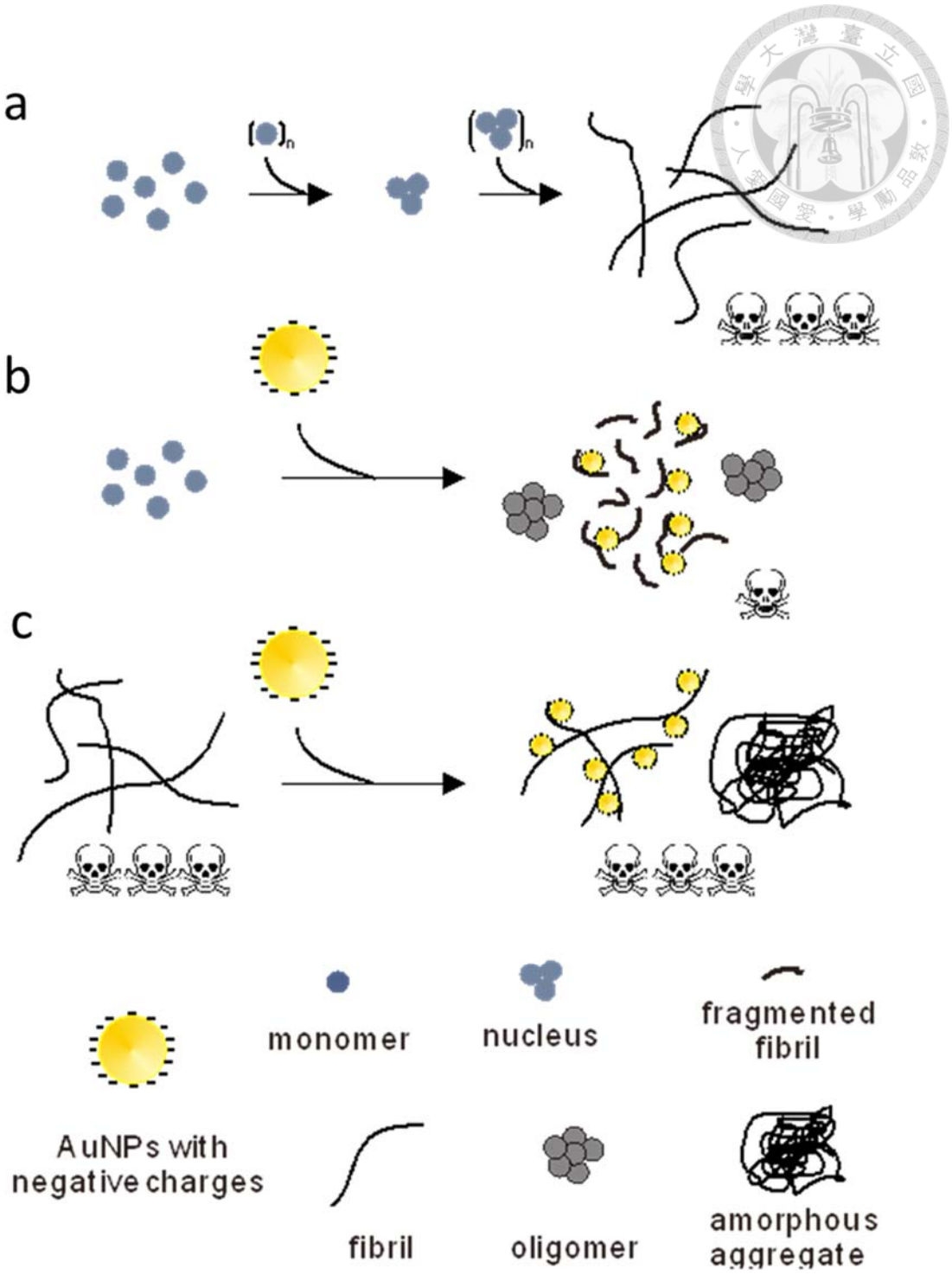

Figure 38. Diagram of Aβ fibrillization pathways influenced by AuNPs. (a) Aβ monomers assemble into mature amyloid fibrils through a nucleation-dependent polymerization and cause neurotoxicity. (b) Aβ monomers incubated with the AuNPs possessing negative surface potential lead to formation of short and fragmented fibrils along with spherical oligomers. The alteration

rescues the toxicity generated from mature Aβ fibrils. (c) AuNPs addition to preformed Aβ fibrils induces ragged fibrils and amorphous aggregates without changing the toxicity level.

6.1.2 Inhibition of Aβ fibrillization by nanoparticles

Inhibition of Aβ40 and Aβ42 fibrillization has been separately reported when mixing with polystyrene, copolymer NPs, and inorganic CdTe NPs[119,120,141]. The copolymeric NiPAM:BAM nanoparicles with less hydrophobicity caused greater extent of retardation in Aβ fibrillization through exclusive interference in the nucleation phase[119]. In addition to the polymer nanoparticles, fullerene molecules can also inhibit Aβ through the uncharged hydrophobic region in Aβ sequence KLVFF[142] and the fibrillization can only be interfered before the fibril formation. AuNPs have been reported to enhance helical coiled-coil peptide fibrillization[143]. Wagner et al. found the stoichiometry of peptides and AuNPs correlates with the nucleus formation leading to more β-sheet fibrils by using different peptide sequences. However, the effect is not generic. Effect of NPs on amyloids is not always in favor of inhibition. In 2007, Linse et al. demonstrated that copolymer NPs, ceriumoxide NPs, quantum dots, and carbon nanotubes all accelerated fibrillization via enhancing nucleation of β2-microglobulin (β_2-m), a dialysis-related amyloid[144]. What is interesting is that Cabaleiro-Lago et al. employed the same copolymeric NiPAM:BAM NPs used in Linse et al. work, but opposite effect was observed on β_2-m. The dual

properties of the same NPs suggest that inhibition only occurs when certain relationship between surface properties of NPs and peptides have to be established.

6.1.3 Effect of localized charge on Aβ fibrillization

We found for the first time that surface charge is essential and that only negatively charged AuNPs inhibit Aβ fibrillization. The charge property of AuNPs are determined by zeta potential which represents the effective surface charges on the colloidal particles and also measures the colloidal stability in solutions[145,146]. The 30 nm bare AuNPs used in this study have a zeta potential at −38 mV as quoted from the manufacture's product description. The amine-conjugated and carboxyl-conjugated AuNPs are + 7 and −39 mV, respectively. By using the negatively charged, but not positively charged, metallic AuNPs, the elongation phase was mainly affected but not the nucleation phase in Aβ fibrillization. Therefore, the negative zeta potential is most likely to be the key factor governing the fibril inhibition. The higher absolute zeta potential representing higher stability of the colloidal system may also contribute somewhat to the effect. Taken together, we suspect that the rate-limiting step of amyloid nucleation is driven by the hydrophobic interactions as demonstrated from previous literatures[119,141] that the hydrophobic nanoparticles can only interfere the species within the nucleation phase. The subsequent elongation phase

is either driven by electrostatic interactions and hydrogen bonding that can be interfered by the negatively charged nanoparticles or redirected due to the species interaction with the negatively charged nanoparticles.

Amyloid aggregates including some types of oligomeric intermediates and fibrils have been shown to be the toxic entities. The surface structure encompassing positively charged clusters of Aβ fibrils have been suggested to contribute to some degree of cytotoxicity[147]. In our experiments, mixed Aβ species including spherical-like oligomers and fragmented short fibrils were both found in the solution after AuNP incubation with Aβ fibrillization and the preformed fibrils. The appearance of such spherical oligomeric species reminds us of the pathological role of the soluble amyloid oligomers in AD. According to our neurotoxicity studies, the altered fibrils after treatment with preformed fibrils did not change the toxicity level probably due to such morphology and species changes were unrelated to fibril toxicity. On the other hand, the bare and carboxyl-conjugated AuNPs induced Aβ oligomers in the Aβ fibrillization were non-toxic and even mitigated the toxicity level. Although the reduce toxicity was not quantitatively proportional to the amount of small species observed in TEM, we think it is due to lacking of precise quantification methods for the toxic entities. Our results suggest that the negatively charged AuNPs in nanomolar range are capable of redirecting Aβ fibrillization into off-pathway intermediates. Similar effect has been seen in a small chemical molecule

from green tea extract, polyphenol (-)-epi-gallocatechine gallate (EGCG), to redirect Aβ and α-synuclein in Parkinson's disease forming off-pathway oligomers[148]. Our data also suggest that the AuNP induced spherical oligomers are different from the pathological soluble Aβ oligomers. Previously, by intravenous administration of different sizes of bare AuNPs in mice has shown that smaller AuNPs, 15 and 50 nm examined, can pass through blood-brain barrier, but not the larger AuNPs, such as 100 and 200 nm[149]. Our results using 30 nm AuNPs may be suitable to penetrate the blood-brain barrier. Overall, our results provide a potential therapeutic development using negatively charged AuNPs on amyloidosis. In conclusion, we have examined the effects of gold nanoparticles (AuNPs) on amyloids using Aβ40 as a model system. Bare AuNPs were found to inhibit Aβ fibrillization and redirect Aβ forming fragmented fibrils and spherical oligomers. Adding bare AuNPs to preformed fibrils resulted in smaller and ragged Aβ species and these AuNPs bound preferentially to Aβ fibrils but not amorphous aggregates. The negative surface potential of AuNPs is very crucial to the observed phenomena since similar effects were observed from carboxyl- but not amine-conjugated AuNPs. The Aβ incubating with negatively charged AuNPs during Aβ fibrillization is less toxic and can be served as potential nano-chaperones to inhibit and redirect Aβ fibrillization and leads to potential applications for AD.

6.2 Homo- and hetero- polymeric Aβ fibrils

We mixed equal molar of wild type Aβ and each of the four FAD related variants in monomeric form and incubate in quiescence to produce hetero-fibrils and sought to identify how this heterogeneity influence the structure of fibrils compared with homo-fibrils formed from monomeric parent species (wild type or FAD). TEM images confirmed formation of fibrils via visualization of fibrillar morphologies. In addition, TEM imaging showed no discernible differences in the morphologies between fibrils homopolymerically or hetero-polymerically incubated. Results from Far-UV circular dichroism spectroscopy first showed that the spectral minimum of E22K was at 228 nm, while the other homo-fibrils had spectral minima around 220 nm. Secondly, we found CD spectum of FAD hetero-fibril can resemble parental FAD homo-fibrils as in the case of E22G, or neither of both parental homo-fibril as in the case of E22Q and D23N. E22K hetero-fibril had no identifiable secondary structure in CD spectrum. We provided complementary data showing that mixed wild type and FAD homo-fibril had different secondary features in terms of CD spectra. The striking difference of E22K homo- and hetero- fibrils from other fibrils were also displayed in FTIR spectra, but was not reflected on the binding stoichiometry of ThT to fibrils. Uniqueness of E22K fibrils were evident in measurement of ThT fluorescence lifetime. Two populations of fluorescence lifetime upon anchoring onto fibrils were determined after fitting experimental curves to a multi-

exponential decay equation for all fibrils in this study. All homo-fibrils except for E22K had a shorter lifetime of 0.8 ns, and a longer lifetime of 1.9 ns. Wild type fibril had a slightly larger value of "longer" lifetime. Fibrillization with equal molar wild type Aβ shortened ThT lifetimes on E22K, E22Q, and D23N fibrils, while prolonging lifetimes for E22G. As ThT fluorescence lifetime has been correlated with sensitive reporter to conformational change of amyloid fibrils[150,151], we suggested the diversity found between hetero- and homo- fibrils reflect subtle differences in fibrillar structures. We will continue exploring adequate relations between ThT lifetime and specific structural characteristics. Three-dimensional structures might be needed to establish a more comprehensive correlation between the observed distinctions in secondary structures with three-dimensional fibrillar structures.

6.3 Cu^{2+} coordination of H6 and D7 mutants of Aβ

Data from titration monitored by intrinsic tyrosine fluorescence showed that loss of H6 impacts on Cu^{2+} binding to Aβ. H6A had a nearly 4-fold decrease in Cu^{2+} affinity. Two of the three D7 mutations, D7A and D7H gave result to enhanced Cu^{2+} affinity, especially D7H, while D7N reduced Cu^{2+} affinity with Aβ. The order of Cu^{2+} binding affinity from the strongest to the weakest in our experiments are D7H > D7A > WT~H6R > D7N >

H6A. Titration data monitored by Bis-ANS fluorescence showed gradual decreased intensities for wild type, D7H, D7N, and H6A Aβ, but not for D7A and H6R. We speculated that unstable monomers may undergo conformational changes, disturbing formation of hydrophobic exposure. Proton NMR results gave information that environment surrounding H6, Y10, and H13/H14 changed after Cu^{2+} addition, which caused corresponding complete disappearance of histidine peaks and severe intensity reduction of tyrosine peak at regions where hydrogens signals of C-H bond on side chains are typically present. Multiple sources of peak intensity loss can account for peak broadening. Signal decrease pattern of Y10 deviated much from titration results of fluorescence spectroscopy, and we were not able to achieve good fitting on our proton NMR results. We speculated that low signal-to-noise ratio was the reason to this failure. Technically, NMR spectroscopy have been successfully applied to identify structural changes of monomeric amyloid in Cu^{2+} titration experiments, from which binding constants derived are consistent with that from fluorescence techniques[139,152]. For instance, Hou et al. reported K_d of wild type Aβ to be 1.6 μM by recording decrease of signal intensities of the R5, V12, and L17 peaks. These residues are the ones neighboring the proposed Cu^{2+} coordinating residues H6 and H13/H14, and fitting data to certain Cu^{2+} binding model. We reasoned that by increasing the "number of scan" at least 10-fold from 48, much improved signal-to-noise ratio would allow us to evaluate Cu^{2+} binding effect

in our study. We are attempting to provide more details of the differential Cu^{2+} binding from EPR and NMR in the future.

6.3.1 Effect of H6 mutation on Cu^{2+} binding to Aβ

Alies et al. employed EPR to show that in their proposed Cu^{2+} coordinating model in physiological pH, the Cu^{2+}-Aβ16 complex can adopt two coordination. The major coordination (component I) is an equatorial sphere in which the Cu^{2+} at the center coordinates with the amide group of D1, H6, H13 or H14, and the carbonyl group from D1-A2 peptide bond[93]. The minor form (component II) is similar to the major one, differing only on the histidine coordination that simultaneously involves H13 and H14, but no H6. On the basis of their model, the diminished affinity of H6A to Cu^{2+} in our system could be explained by an incompetent component I because H6A is not capable of binding Cu^{2+}. Our finding that H6R did not alter Cu^{2+} affinity could be due to two scenarios. First, replacement of H6 with an amino acid bearing a positive charge side chain preserve the charge property of H6, thus maintaining the integrity of Cu^{2+} coordination. The same conjecture was made to account for the similarity of H6A and H6R Aβ(1-16) in Alies et al. paper. The second scenario is that the Cu^{2+}-H6R complex in our experiments bears a coordination like component II, circumventing the diminishment

seen in Cu^{2+}-H6A complex. In fact, Alies et al. also identified that coordination in Cu^{2+}-H6RAβ16 dominantly assume component II coordination adopted by Cu^{2+}-Aβ16, which lend support to our results.

6.3.2 Effect of D7 mutation on Cu^{2+} binding to Aβ

The discrepancy in the association constants derived from tyrosine and Bis-ANS fluorescence could be the consequences that multiple sources of hydrophobic clusters complicated the Bis-ANS fluorescence readings. For instance, hydrophobic regions can be induced intramolecularly upon Cu^{2+} binding, and could as well be formed intermolecularly via assembly of Cu^{2+}-Aβ complexes into large aggregates, thus interfering determination of association constants. ^{1}H-^{15}N HSQC NMR spectra of wild type and D7H showed identical peak reducing patterns after equal molar of Cu^{2+} was added. The complete loss of F20 and D23 peaks in D7H spectrum after two molar equivalent of Cu^{2+} could be due to distinct Cu^{2+} binding mode between wild type and D7H Aβ. We speculated that in physiological pH because Cu^{2+} binding in component I of the proposed model only requires a histidine from H6 and another one from either H13 or H14, the remaining histidine could coordinate an extra histidine if available. It is likely that D7H offers a fourth histidine adjacent to H6, forming a similar steric configuration

with H13 or H14, thereby constituting stronger affinity than wild type Aβ. In future work, detailed Cu^{2+} coordination needs to be provided to verify our speculation and correlate our findings in Cu^{2+} titration with coordination.

Reference

1. Alzheimer, A., Stelzmann, R. A., Schnitzlein, H. N. & Murtagh, F. R. An English translation of Alzheimer's 1907 paper, 'Uber eine eigenartige Erkankung der Hirnrinde'. *Clin Anat* **8,** 429–431 (1995).
2. Alzheimer's News 1/17/2014 | Alzheimer's Association. at <http://www.alz.org/news_and_events_law_by_obama.asp>
3. Abbott, A. Dementia: A problem for our age. *Nature* **475,** S2–S4 (2011).
4. Brookmeyer, R., Johnson, E., Ziegler-Graham, K. & Arrighi, H. M. Forecasting the global burden of Alzheimer's disease. *Alzheimer's & Dementia* **3,** 186–191 (2007).
5. Mattson, M. P. Pathways towards and away from Alzheimer's disease. *Nature* **430,** 631–639 (2004).
6. 2014 Alzheimer's disease facts and figures. *Alzheimer's & Dementia* **10,** e47–e92 (2014).
7. Lindsay, J. *et al.* Risk Factors for Alzheimer's Disease: A Prospective Analysis from the Canadian Study of Health and Aging. *Am. J. Epidemiol.* **156,** 445–453 (2002).
8. Tanzi, R. E. & Bertram, L. Twenty years of the Alzheimer's disease amyloid hypothesis: a genetic perspective. *Cell* **120,** 545–55 (2005).
9. Jellinger, K. Head injury and dementia. *Current Opinion in Neurology December 2004* **17,** 719–723 (2004).
10. Simons, M., Keller, P., Dichgans, J. & Schulz, J. B. Cholesterol and Alzheimer's disease: is there a link? *Neurology* **57,** 1089–1093 (2001).
11. Florent-Béchard, S. *et al.* The essential role of lipids in Alzheimer's disease. *Biochimie* **91,** 804–809 (2009).
12. Van Echten-Deckert, G. & Walter, J. Sphingolipids: Critical players in Alzheimer's disease. *Progress in Lipid Research* **51,** 378–393 (2012).
13. Biessels, G. J. & Kappelle, L. J. Increased risk of Alzheimer's disease in Type II diabetes: insulin resistance of the brain or insulin-induced amyloid pathology? *Biochemical Society Transactions* **33,** 1041 (2005).
14. Hölscher, C. Diabetes as a risk factor for Alzheimer's disease: insulin signalling impairment in the brain as an alternative model of Alzheimer's disease. *Biochemical Society Transactions* **39,** 891–897 (2011).
15. Zatta, P., Drago, D., Bolognin, S. & Sensi, S. L. Alzheimer's disease, metal ions and metal homeostatic therapy. *Trends Pharmacol Sci* **30,** 346–55 (2009).
16. Duce, J. A. & Bush, A. I. Biological metals and Alzheimer's disease: implications for therapeutics and diagnostics. *Prog Neurobiol* **92,** 1–18 (2010).

17. Amadoruge, P. C. & Barnham, K. J. Alzheimer's disease and metals: a review of the involvement of cellular membrane receptors in metallosignalling. *Int J Alzheimers Dis* **2011,** 542043 (2011).
18. Roberts, B. R., Ryan, T. M., Bush, A. I., Masters, C. L. & Duce, J. A. The role of metallobiology and amyloid-beta peptides in Alzheimer's disease. *J Neurochem* **120 Suppl 1,** 149–66 (2012).
19. Lovell, M. ., Robertson, J. ., Teesdale, W. ., Campbell, J. . & Markesbery, W. . Copper, iron and zinc in Alzheimer's disease senile plaques. *Journal of the Neurological Sciences* **158,** 47–52 (1998).
20. Kepp, K. P. Bioinorganic Chemistry of Alzheimer's Disease. *Chem. Rev.* **112,** 5193–5239 (2012).
21. Ballard, C. *et al.* Alzheimer's disease. *Lancet* **377,** 1019–31 (2011).
22. Lemere, C. A. & Masliah, E. Can Alzheimer disease be prevented by amyloid-β immunotherapy? *Nat Rev Neurol* **6,** 108–119 (2010).
23. Delrieu, J., Ousset, P. J., Caillaud, C. & Vellas, B. 'Clinical trials in Alzheimer's disease': immunotherapy approaches. *J. Neurochem.* **120 Suppl 1,** 186–193 (2012).
24. Ritchie CW, Bush AI, Mackinnon A & et al. Metal-protein attenuation with iodochlorhydroxyquin (clioquinol) targeting aβ amyloid deposition and toxicity in alzheimer disease: A pilot phase 2 clinical trial. *Arch Neurol* **60,** 1685–1691 (2003).
25. Bush, A. I. Drug development based on the metals hypothesis of Alzheimer's disease. *J. Alzheimers Dis.* **15,** 223–240 (2008).
26. Lannfelt, L. *et al.* Safety, efficacy, and biomarker findings of PBT2 in targeting Aβ as a modifying therapy for Alzheimer's disease: a phase IIa, double-blind, randomised, placebo-controlled trial. *The Lancet Neurology* **7,** 779–786 (2008).
27. Bulic, B. *et al.* Development of tau aggregation inhibitors for Alzheimer's disease. *Angew. Chem. Int. Ed. Engl.* **48,** 1740–1752 (2009).
28. Wischik, C. M., Harrington, C. R. & Storey, J. M. D. Tau-aggregation inhibitor therapy for Alzheimer's disease. *Biochem. Pharmacol.* **88,** 529–539 (2014).
29. Sunde, M. *et al.* Common core structure of amyloid fibrils by synchrotron X-ray diffraction. *Journal of Molecular Biology* **273,** 729–739 (1997).
30. Klunk, W. E., Jacob, R. F. & Mason, R. P. in *Methods in Enzymology* (ed. Ronald Wetzel) **Volume 309,** 285–305 (Academic Press, 1999).
31. Naiki, H., Higuchi, K., Hosokawa, M. & Takeda, T. Fluorometric determination of amyloid fibrils in vitro using the fluorescent dye, thioflavine T. *Analytical Biochemistry* **177,** 244–249 (1989).
32. Tycko, R. & Wickner, R. B. Molecular Structures of Amyloid and Prion Fibrils: Consensus versus Controversy. *Acc. Chem. Res.* **46,** 1487–1496 (2013).

33. Hardy, J. & Allsop, D. Amyloid deposition as the central event in the aetiology of Alzheimer's disease. *Trends Pharmacol. Sci.* **12,** 383–388 (1991).
34. Huang, X., Moir, R. D., Tanzi, R. E., Bush, A. I. & Rogers, J. T. Redox-Active Metals, Oxidative Stress, and Alzheimer's Disease Pathology. *Annals of the New York Academy of Sciences* **1012,** 153–163 (2004).
35. Sofic, E. *et al.* Increased iron (III) and total iron content in post mortem substantia nigra of parkinsonian brain. *J. Neural Transmission* **74,** 199–205 (1988).
36. Schrag, M., Mueller, C., Oyoyo, U., Smith, M. A. & Kirsch, W. M. Iron, zinc and copper in the Alzheimer's disease brain: A quantitative meta-analysis. Some insight on the influence of citation bias on scientific opinion. *Progress in Neurobiology* **94,** 296–306 (2011).
37. Zhu, X., Raina, A. K., Perry, G. & Smith, M. A. Alzheimer's disease: the two-hit hypothesis. *The Lancet Neurology* **3,** 219–226 (2004).
38. Zhu, X., Lee, H., Perry, G. & Smith, M. A. Alzheimer disease, the two-hit hypothesis: An update. *Biochimica et Biophysica Acta (BBA) - Molecular Basis of Disease* **1772,** 494–502 (2007).
39. Shen, J. & Kelleher, R. J., 3rd. The presenilin hypothesis of Alzheimer's disease: evidence for a loss-of-function pathogenic mechanism. *Proc Natl Acad Sci U S A* **104,** 403–9 (2007).
40. Kang, J. *et al.* The precursor of Alzheimer's disease amyloid A4 protein resembles a cell-surface receptor. *Nature* **325,** 733–736 (1987).
41. Thinakaran, G. & Koo, E. H. Amyloid Precursor Protein Trafficking, Processing, and Function. *J. Biol. Chem.* **283,** 29615–29619 (2008).
42. Vingtdeux, V., Sergeant, N. & Buee, L. Potential contribution of exosomes to the prion-like propagation of lesions in Alzheimer's disease. *Front. Physio.* **3,** 229 (2012).
43. Francis, R. *et al.* aph-1 and pen-2 are required for Notch pathway signaling, gamma-secretase cleavage of betaAPP, and presenilin protein accumulation. *Dev. Cell* **3,** 85–97 (2002).
44. Bibl, M. *et al.* Blood-based neurochemical diagnosis of vascular dementia: a pilot study. *Journal of Neurochemistry* **103,** 467–474 (2007).
45. Schoonenboom, N. S. *et al.* Amyloid β 38, 40, and 42 species in cerebrospinal fluid: More of the same? *Ann Neurol.* **58,** 139–142 (2005).
46. Burdick, D. *et al.* Assembly and aggregation properties of synthetic Alzheimer's A4/beta amyloid peptide analogs. *J. Biol. Chem.* **267,** 546–554 (1992).
47. Jarrett, J. T., Berger, E. P. & Lansbury, P. T. The carboxy terminus of the .beta. amyloid protein is critical for the seeding of amyloid formation: Implications for the pathogenesis of Alzheimer's disease. *Biochemistry* **32,** 4693–4697 (1993).

48. Riek, R., Güntert, P., Döbeli, H., Wipf, B. & Wüthrich, K. NMR studies in aqueous solution fail to identify significant conformational differences between the monomeric forms of two Alzheimer peptides with widely different plaque-competence, Aβ(1–40)ox and Aβ(1–42)ox. *European Journal of Biochemistry* **268,** 5930–5936 (2001).
49. Petkova, A. T. *et al.* A structural model for Alzheimer's β-amyloid fibrils based on experimental constraints from solid state NMR. *PNAS* **99,** 16742–16747 (2002).
50. Haass, C. & Selkoe, D. J. Soluble protein oligomers in neurodegeneration: lessons from the Alzheimer's amyloid beta-peptide. *Nat Rev Mol Cell Biol* **8,** 101–12 (2007).
51. Jan, A., Gokce, O., Luthi-Carter, R. & Lashuel, H. A. The Ratio of Monomeric to Aggregated Forms of Aβ40 and Aβ42 Is an Important Determinant of Amyloid-β Aggregation, Fibrillogenesis, and Toxicity. *J. Biol. Chem.* **283,** 28176–28189 (2008).
52. Jin, M. *et al.* Soluble amyloid beta-protein dimers isolated from Alzheimer cortex directly induce Tau hyperphosphorylation and neuritic degeneration. *Proc. Natl. Acad. Sci. U.S.A.* **108,** 5819–5824 (2011).
53. Kayed, R. *et al.* Common Structure of Soluble Amyloid Oligomers Implies Common Mechanism of Pathogenesis. *Science* **300,** 486–489 (2003).
54. Lambert, M. P. *et al.* Diffusible, nonfibrillar ligands derived from Abeta1-42 are potent central nervous system neurotoxins. *Proc. Natl. Acad. Sci. U.S.A.* **95,** 6448–6453 (1998).
55. Barghorn, S. *et al.* Globular amyloid beta-peptide oligomer - a homogenous and stable neuropathological protein in Alzheimer's disease. *J. Neurochem.* **95,** 834–847 (2005).
56. Nimmrich, V. *et al.* Amyloid beta oligomers (A beta(1-42) globulomer) suppress spontaneous synaptic activity by inhibition of P/Q-type calcium currents. *J. Neurosci.* **28,** 788–797 (2008).
57. Lasagna-Reeves, C. A., Glabe, C. G. & Kayed, R. Amyloid-beta Annular Protofibrils Evade Fibrillar Fate in Alzheimer Disease Brain. *J Biol Chem* **286,** 22122–30 (2011).
58. Lesné, S. *et al.* A specific amyloid-β protein assembly in the brain impairs memory. *Nature* **440,** 352–357 (2006).
59. Paranjape, G. S., Gouwens, L. K., Osborn, D. C. & Nichols, M. R. Isolated Amyloid-β(1–42) Protofibrils, But Not Isolated Fibrils, Are Robust Stimulators of Microglia. *ACS Chem. Neurosci.* **3,** 302–311 (2012).
60. Dahlgren, K. N. *et al.* Oligomeric and Fibrillar Species of Amyloid-β Peptides Differentially Affect Neuronal Viability. *J. Biol. Chem.* **277,** 32046–32053 (2002).
61. Petkova, A. T. *et al.* Self-Propagating, Molecular-Level Polymorphism in Alzheimer's ß-Amyloid Fibrils. *Science* **307,** 262–265 (2005).

62. Manna, M. & Mukhopadhyay, C. Binding, Conformational Transition and Dimerization of Amyloid-β Peptide on GM1-Containing Ternary Membrane: Insights from Molecular Dynamics Simulation. *PLoS ONE* **8,** e71308 (2013).
63. Hou, L. *et al.* Solution NMR Studies of the Aβ(1−40) and Aβ(1−42) Peptides Establish that the Met35 Oxidation State Affects the Mechanism of Amyloid Formation. *J. Am. Chem. Soc.* **126,** 1992–2005 (2004).
64. Chen, Y.-R. & Glabe, C. G. Distinct Early Folding and Aggregation Properties of Alzheimer Amyloid-β Peptides Aβ40 and Aβ42 STABLE TRIMER OR TETRAMER FORMATION BY Aβ42. *J. Biol. Chem.* **281,** 24414–24422 (2006).
65. Ni, C.-L., Shi, H.-P., Yu, H.-M., Chang, Y.-C. & Chen, Y.-R. Folding stability of amyloid-β 40 monomer is an important determinant of the nucleation kinetics in fibrillization. *FASEB J* **25,** 1390–1401 (2011).
66. Lazo, N. D., Grant, M. A., Condron, M. C., Rigby, A. C. & Teplow, D. B. On the nucleation of amyloid β-protein monomer folding. *Protein Science* **14,** 1581–1596 (2005).
67. Grant, M. A. *et al.* Familial Alzheimer's disease mutations alter the stability of the amyloid β-protein monomer folding nucleus. *PNAS* **104,** 16522–16527 (2007).
68. Harper, J. D. & Lansbury, P. T., Jr. Models of amyloid seeding in Alzheimer's disease and scrapie: mechanistic truths and physiological consequences of the time-dependent solubility of amyloid proteins. *Annu. Rev. Biochem.* **66,** 385–407 (1997).
69. Roychaudhuri, R., Yang, M., Hoshi, M. M. & Teplow, D. B. Amyloid beta-protein assembly and Alzheimer disease. *J Biol Chem* **284,** 4749–53 (2009).
70. Luhrs, T. *et al.* 3D structure of Alzheimer's amyloid-beta(1-42) fibrils. *Proc Natl Acad Sci U S A* **102,** 17342–7 (2005).
71. Tycko, R. Molecular structure of amyloid fibrils: insights from solid-state NMR. *Quarterly Reviews of Biophysics* **39,** 1–55 (2006).
72. Petkova, A. T., Yau, W.-M. & Tycko, R. Experimental constraints on quaternary structure in Alzheimer's beta-amyloid fibrils. *Biochemistry* **45,** 498–512 (2006).
73. Bonda, D. J. *et al.* Role of metal dyshomeostasis in Alzheimer's disease. *Metallomics* **3,** 267–270 (2011).
74. Lovell, M. A., Robertson, J. D., Teesdale, W. J., Campbell, J. L. & Markesbery, W. R. Copper, iron and zinc in Alzheimer's disease senile plaques. *Journal of the Neurological Sciences* **158,** 47–52 (1998).
75. Bush, A. I. The metallobiology of Alzheimer's disease. *Trends in Neurosciences* **26,** 207–214 (2003).
76. Faller, P., Hureau, C. & Berthoumieu, O. Role of Metal Ions in the Self-assembly of the Alzheimer's Amyloid-β Peptide. *Inorg. Chem.* **52,** 12193–12206 (2013).

77. Stellato, F. *et al.* Metal binding in amyloid β-peptides shows intra- and inter-peptide coordination modes. *Eur Biophys J* **35,** 340–351 (2006).
78. Sarell, C. J., Syme, C. D., Rigby, S. E. J. & Viles, J. H. Copper(II) Binding to Amyloid-β Fibrils of Alzheimer's Disease Reveals a Picomolar Affinity: Stoichiometry and Coordination Geometry Are Independent of Aβ Oligomeric Form. *Biochemistry* **48,** 4388–4402 (2009).
79. Shin, B. & Saxena, S. Direct Evidence That All Three Histidine Residues Coordinate to Cu(II) in Amyloid-β1−16†. *Biochemistry* **47,** 9117–9123 (2008).
80. Dorlet, P., Gambarelli, S., Faller, P. & Hureau, C. Pulse EPR Spectroscopy Reveals the Coordination Sphere of Copper(II) Ions in the 1–16 Amyloid-β Peptide: A Key Role of the First Two N-Terminus Residues. *Angewandte Chemie International Edition* **48,** 9273–9276 (2009).
81. Smith, D. P. *et al.* Copper-mediated Amyloid-β Toxicity Is Associated with an Intermolecular Histidine Bridge. *J. Biol. Chem.* **281,** 15145–15154 (2006).
82. Syme, C. D. & Viles, J. H. Solution 1H NMR investigation of Zn^{2+} and Cd^{2+} binding to amyloid-beta peptide (Aβ) of Alzheimer's disease. *Biochimica et Biophysica Acta (BBA) - Proteins and Proteomics* **1764,** 246–256 (2006).
83. Curtain, C. C. *et al.* Alzheimer's Disease Amyloid-β Binds Copper and Zinc to Generate an Allosterically Ordered Membrane-penetrating Structure Containing Superoxide Dismutase-like Subunits. *J. Biol. Chem.* **276,** 20466–20473 (2001).
84. Minicozzi, V. *et al.* Identifying the Minimal Copper- and Zinc-binding Site Sequence in Amyloid-β Peptides. *J. Biol. Chem.* **283,** 10784–10792 (2008).
85. Tsvetkov, P. O. *et al.* Minimal Zn^{2+} Binding Site of Amyloid-β. *Biophysical Journal* **99,** L84–L86 (2010).
86. Nair, N. G., Perry, G., Smith, M. A. & Reddy, V. P. NMR Studies of Zinc, Copper, and Iron Binding to Histidine, the Principal Metal Ion Complexing Site of Amyloid-β Peptide. *Journal of Alzheimer's Disease* **20,** 57–66 (2010).
87. Bertram, L. The genetic epidemiology of neurodegenerative disease. *Journal of Clinical Investigation* **115,** 1449–1457 (2005).
88. Benilova, I., Karran, E. & De Strooper, B. The toxic Aβ oligomer and Alzheimer's disease: an emperor in need of clothes. *Nat Neurosci* **15,** 349–357 (2012).
89. Xu, L., Shan, S. & Wang, X. Single Point Mutation Alters the Microstate Dynamics of Amyloid β-Protein Aβ42 as Revealed by Dihedral Dynamics Analyses. *J. Phys. Chem. B* **117,** 6206–6216 (2013).
90. Baumketner, A., Krone, M. G. & Shea, J.-E. Role of the familial Dutch mutation E22Q in the folding and aggregation of the 15–28 fragment of the Alzheimer amyloid-β protein. *PNAS* **105,** 6027–6032 (2008).

91. Hori, Y. *et al.* The Tottori (D7N) and English (H6R) Familial Alzheimer Disease Mutations Accelerate Aβ Fibril Formation without Increasing Protofibril Formation. *J. Biol. Chem.* **282,** 4916–4923 (2007).
92. Chen, W.-T. *et al.* Amyloid-Beta (Aβ) D7H Mutation Increases Oligomeric Aβ42 and Alters Properties of Aβ-Zinc/Copper Assemblies. *PLoS ONE* **7,** e35807 (2012).
93. Alies, B. *et al.* pH-Dependent Cu(II) Coordination to Amyloid-β Peptide: Impact of Sequence Alterations, Including the H6R and D7N Familial Mutations. *Inorg. Chem.* **50,** 11192–11201 (2011).
94. Jonsson, T. *et al.* A mutation in APP protects against Alzheimer's disease and age-related cognitive decline. *Nature* **488,** 96–99 (2012).
95. Fede, G. D. *et al.* A Recessive Mutation in the APP Gene with Dominant-Negative Effect on Amyloidogenesis. *Science* **323,** 1473–1477 (2009).
96. Drew, S. C., Masters, C. L. & Barnham, K. J. Alzheimer's Aβ Peptides with Disease-Associated N-Terminal Modifications: Influence of Isomerisation, Truncation and Mutation on Cu^{2+} Coordination. *PLoS ONE* **5,** e15875 (2010).
97. Mout, R., Moyano, D. F., Rana, S. & Rotello, V. M. Surface functionalization of nanoparticles for nanomedicine. *Chem Soc Rev* **41,** 2539–44 (2012).
98. Kim, S. T., Saha, K., Kim, C. & Rotello, V. M. The Role of Surface Functionality in Determining Nanoparticle Cytotoxicity. *Acc. Chem. Res.* **46,** 681–691 (2013).
99. Sapsford, K. E. *et al.* Functionalizing Nanoparticles with Biological Molecules: Developing Chemistries that Facilitate Nanotechnology. *Chem. Rev.* **113,** 1904–2074 (2013).
100. Mirkin, C. A. *et al.* Gold Nanoparticles for Biology and Medicine. *Angewandte Chemie-International Edition* **49,** 3280–3294 (2010).
101. Kumar, A., Zhang, X. & Liang, X.-J. Gold nanoparticles: emerging paradigm for targeted drug delivery system. *Biotechnol. Adv.* **31,** 593–606 (2013).
102. Parveen, S., Misra, R. & Sahoo, S. K. Nanoparticles: a boon to drug delivery, therapeutics, diagnostics and imaging. *Nanomedicine: Nanotechnology, Biology and Medicine* **8,** 147–166 (2012).
103. Doane, T. L. & Burda, C. The unique role of nanoparticles in nanomedicine: imaging, drug delivery and therapy. *Chem Soc Rev* **41,** 2885–2911 (2012).
104. Khandelia, R., Jaiswal, A., Ghosh, S. S. & Chattopadhyay, A. Nanocarriers: Gold Nanoparticle–Protein Agglomerates as Versatile Nanocarriers for Drug Delivery (Small 20/2013). *Small* **9,** 3493–3493 (2013).
105. Murphy, C. J. *et al.* Gold nanoparticles in biology: beyond toxicity to cellular imaging. *Acc Chem Res* **41,** 1721–30 (2008).

106. Psarros, C., Lee, R., Margaritis, M. & Antoniades, C. Nanomedicine for the prevention, treatment and imaging of atherosclerosis. *Nanomedicine* **8 Suppl 1,** S59–68 (2012).
107. Doll, T. A. P. F., Raman, S., Dey, R. & Burkhard, P. Nanoscale assemblies and their biomedical applications. *J. R. Soc. Interface* **10,** (2013).
108. Brambilla, D. *et al.* Nanotechnologies for Alzheimer's disease: diagnosis, therapy, and safety issues. *Nanomedicine: Nanotechnology, Biology and Medicine* **7,** 521–540 (2011).
109. Boer, D. A. G. de & Gaillard, P. J. Strategies to Improve Drug Delivery Across the Blood-Brain Barrier. *Clin Pharmacokinet* **46,** 553–576 (2007).
110. Jain, K. K. Nanobiotechnology-based drug delivery to the central nervous system. *Neurodegener Dis* **4,** 287–291 (2007).
111. Modi, G. *et al.* Nanotechnological applications for the treatment of neurodegenerative disorders. *Prog Neurobiol* **88,** 272–85 (2009).
112. Sahni, J. K. *et al.* Neurotherapeutic applications of nanoparticles in Alzheimer's disease. *J Control Release* **152,** 208–31 (2011).
113. Goldsmith, M., Abramovitz, L. & Peer, D. Precision Nanomedicine in Neurodegenerative Diseases. *ACS Nano* **8,** 1958–1965 (2014).
114. Cherny, R. A. *et al.* Treatment with a Copper-Zinc Chelator Markedly and Rapidly Inhibits β-Amyloid Accumulation in Alzheimer's Disease Transgenic Mice. *Neuron* **30,** 665–676 (2001).
115. Härtig, W. *et al.* Electron microscopic analysis of nanoparticles delivering thioflavin-T after intrahippocampal injection in mouse: implications for targeting β-amyloid in Alzheimer's disease. *Neuroscience Letters* **338,** 174–176 (2003).
116. Kogan, M. J. *et al.* Nanoparticle-Mediated Local and Remote Manipulation of Protein Aggregation. *Nano Lett.* **6,** 110–115 (2006).
117. Song, Q. *et al.* Lipoprotein-Based Nanoparticles Rescue the Memory Loss of Mice with Alzheimer's Disease by Accelerating the Clearance of Amyloid-Beta. *ACS Nano* (2014). doi:10.1021/nn4058215
118. Edelhoch, H. Spectroscopic determination of tryptophan and tyrosine in proteins. *Biochemistry* **6,** 1948–54 (1967).
119. Cabaleiro-Lago, C. *et al.* Inhibition of amyloid beta protein fibrillation by polymeric nanoparticles. *J Am Chem Soc* **130,** 15437–43 (2008).
120. Yoo, S. I. *et al.* Inhibition of Amyloid Peptide Fibrillation by Inorganic Nanoparticles: Functional Similarities with Proteins. *Angew. Chem. Int. Ed.* **50,** 5110–5115 (2011).
121. Brambilla, D. *et al.* Colloidal properties of biodegradable nanoparticles influence interaction with amyloid-β peptide. *Journal of Biotechnology* **156,** 338–340 (2011).

122. Zhang, D. *et al.* Gold nanoparticles can induce the formation of protein-based aggregates at physiological pH. *Nano Letters* **9,** 666–71 (2009).
123. LeVine III, H. in *Methods in Enzymology* (ed. Ronald Wetzel) **Volume 309,** 274–284 (Academic Press, 1999).
124. Biancalana, M. & Koide, S. Molecular mechanism of Thioflavin-T binding to amyloid fibrils. *Biochim. Biophys. Acta* **1804,** 1405–1412 (2010).
125. Nilsson, M. R. Techniques to study amyloid fibril formation in vitro. *Methods* **34,** 151–160 (2004).
126. Krebs, M. R. H., Morozova-Roche, L. A., Daniel, K., Robinson, C. V. & Dobson, C. M. Observation of sequence specificity in the seeding of protein amyloid fibrils. *Protein Science* **13,** 1933–1938 (2004).
127. Johan, K. *et al.* Acceleration of amyloid protein A amyloidosis by amyloid-like synthetic fibrils. *PNAS* **95,** 2558–2563 (1998).
128. Suzuki, N. *et al.* An increased percentage of long amyloid beta protein secreted by familial amyloid beta protein precursor (beta APP717) mutants. *Science* **264,** 1336–1340 (1994).
129. Frost, D., Gorman, P. M., Yip, C. M. & Chakrabartty, A. Co-incorporation of Aβ40 and Aβ42 to form mixed pre-fibrillar aggregates. *European Journal of Biochemistry* **270,** 654–663 (2003).
130. Kulic, L. *et al.* Early accumulation of intracellular fibrillar oligomers and late congophilic amyloid angiopathy in mice expressing the Osaka intra-Aβ APP mutation. *Transl Psychiatry* **2,** e183 (2012).
131. Natalello, A., Ami, D. & Doglia, S. M. in *Intrinsically Disordered Protein Analysis* (eds. Uversky, V. N., Dunker, A. K. & Walker, J. M.) **895,** 229–244 (Humana Press, 2012).
132. Mohanty, J., Choudhury, S. D., Pal, H. & Bhasikuttan, A. C. Early detection of insulin fibrillation: a fluorescence lifetime assay to probe the pre-fibrillar regime. *Chem. Commun.* **48,** 2403–2405 (2012).
133. Chen, W.-T., Liao, Y.-H., Yu, H.-M., Cheng, I. H. & Chen, Y.-R. Distinct Effects of Zn^{2+}, Cu^{2+}, Fe^{3+}, and Al^{3+} on Amyloid-β Stability, Oligomerization, and Aggregation AMYLOID-β DESTABILIZATION PROMOTES ANNULAR PROTOFIBRIL FORMATION. *J. Biol. Chem.* **286,** 9646–9656 (2011).
134. Alies, B. *et al.* Cu(II) Affinity for the Alzheimer's Peptide: Tyrosine Fluorescence Studies Revisited. *Anal. Chem.* **85,** 1501–1508 (2013).
135. Kremer, J. J., Pallitto, M. M., Sklansky, D. J. & Murphy, R. M. Correlation of β-Amyloid Aggregate Size and Hydrophobicity with Decreased Bilayer Fluidity of Model Membranes†. *Biochemistry* **39,** 10309–10318 (2000).

136. Bolognesi, B. *et al.* ANS Binding Reveals Common Features of Cytotoxic Amyloid Species. *ACS Chem. Biol.* **5,** 735–740 (2010).
137. Teplow, D. B. Preparation of amyloid beta-protein for structural and functional studies. *Methods Enzymol* **413,** 20–33 (2006).
138. Syme, C. D., Nadal, R. C., Rigby, S. E. J. & Viles, J. H. Copper Binding to the Amyloid-β (Aβ) Peptide Associated with Alzheimer's Disease FOLDING, COORDINATION GEOMETRY, pH DEPENDENCE, STOICHIOMETRY, AND AFFINITY OF Aβ-(1–28): INSIGHTS FROM A RANGE OF COMPLEMENTARY SPECTROSCOPIC TECHNIQUES. *J. Biol. Chem.* **279,** 18169–18177 (2004).
139. Hou, L. & Zagorski, M. G. NMR Reveals Anomalous Copper(II) Binding to the Amyloid Aβ Peptide of Alzheimer's Disease. *J. Am. Chem. Soc.* **128,** 9260–9261 (2006).
140. Biancalana, M. & Koide, S. Molecular mechanism of Thioflavin-T binding to amyloid fibrils. *Biochim Biophys Acta* **1804,** 1405–12 (2010).
141. Cabaleiro-Lago, C., Quinlan-Pluck, F., Lynch, I., Dawson, K. A. & Linse, S. Dual Effect of Amino Modified Polystyrene Nanoparticles on Amyloid beta Protein Fibrillation. *Acs Chemical Neuroscience* **1,** 279–287 (2010).
142. Kim, J. E. & Lee, M. Fullerene inhibits beta-amyloid peptide aggregation. *Biochem Biophys Res Commun* **303,** 576–9 (2003).
143. Wagner, S. C. *et al.* Nanoparticle-induced folding and fibril formation of coiled-coil-based model peptides. *Small* **6,** 1321–8 (2010).
144. Linse, S. *et al.* Nucleation of protein fibrillation by nanoparticles. *Proc Natl Acad Sci U S A* **104,** 8691–6 (2007).
145. Alvarez-Puebla, R. A., Arceo, E., Goulet, P. J., Garrido, J. J. & Aroca, R. F. Role of nanoparticle surface charge in surface-enhanced Raman scattering. *J Phys Chem B* **109,** 3787–92 (2005).
146. Olmedo, I. *et al.* How changes in the sequence of the peptide CLPFFD-NH2 can modify the conjugation and stability of gold nanoparticles and their affinity for beta-amyloid fibrils. *Bioconjug Chem* **19,** 1154–63 (2008).
147. Yoshiike, Y., Akagi, T. & Takashima, A. Surface Structure of Amyloid-β Fibrils Contributes to Cytotoxicity. *Biochemistry* **46,** 9805–9812 (2007).
148. Ehrnhoefer, D. E. *et al.* EGCG redirects amyloidogenic polypeptides into unstructured, off-pathway oligomers. *Nat Struct Mol Biol* **15,** 558–566 (2008).
149. Sonavane, G., Tomoda, K. & Makino, K. Biodistribution of colloidal gold nanoparticles after intravenous administration: effect of particle size. *Colloids Surf B Biointerfaces* **66,** 274–80 (2008).

150. Stsiapura, V. I. *et al.* Thioflavin T as a Molecular Rotor: Fluorescent Properties of Thioflavin T in Solvents with Different Viscosity. *J. Phys. Chem. B* **112,** 15893–15902 (2008).
151. Mohanty, J., Choudhury, S. D., Pal, H. & Bhasikuttan, A. C. Early detection of insulin fibrillation: a fluorescence lifetime assay to probe the pre-fibrillar regime. *Chem. Commun.* **48,** 2403–2405 (2012).
152. Danielsson, J., Pierattelli, R., Banci, L. & Gräslund, A. High-resolution NMR studies of the zinc-binding site of the Alzheimer's amyloid β-peptide. *FEBS Journal* **274,** 46–59 (2007).

Supplementary data

Negatively charged AuNPs reduce the neurotoxicity induced by Aβ

This experiment was carried out by Mr. Yu-Jen Chang in our lab. To assess the neurotoxicity effect of the AuNP-induced Aβ species, we performed MTT assays that examined the activity of mitochondrial alcohol dehydragenase by treating human neuroblastoma cells, BE-(2)-C, with the end-point products specified in Chapter 3.2 and 3.3. Neurotoxicity was demonstrated by the reduction of cell viability and the viability was normalized to the ones treated with the buffer controls. Aβ fibril alone contributed to ~24-30 % of cytotoxicity to the neuroblastoma cells (Figure S1). For the end-point products obtained from Aβ monomers incubated with various concentrations of bare AuNPs, the neurotoxicity decreased in a AuNP dose-dependent manner. When AuNP concentration was at 1.36 nM, the toxicity was significantly reduced to ~16 % (Figure S1a). The difference was statistically significant (p-value = 0.0404 using two-tailed Student's t-test). Similar toxicity reduction and AuNP dose-dependence were observed for treatment of the end-point Aβ products incubated with carboxyl-conjugated AuNPs. In contrast, the toxicity did not reduce but rather slightly increased in the ones incubated with amine-conjugated AuNPs. These results suggested that only bare and carboxyl-conjugated AuNPs are capable of redirecting Aβ fibrillization pathways to form less toxic

species. When treating the end-point products of preformed fibrils incubated with bare AuNPs, we did not observe significant changes in cytotoxicity level (Figure S1b). The data implicated that although bare AuNPs also altered the preformed Aβ fibrils and produced rough fibrils and some small oligomers as well as amorphous aggregates at higher AuNP concentrations, the end-point products did not change the toxicity level significantly. For a brief summary, only the bare and carboxyl-conjugated AuNPs incubated during Aβ fibrillization contribute to noticeable reduction of neurotoxicity.

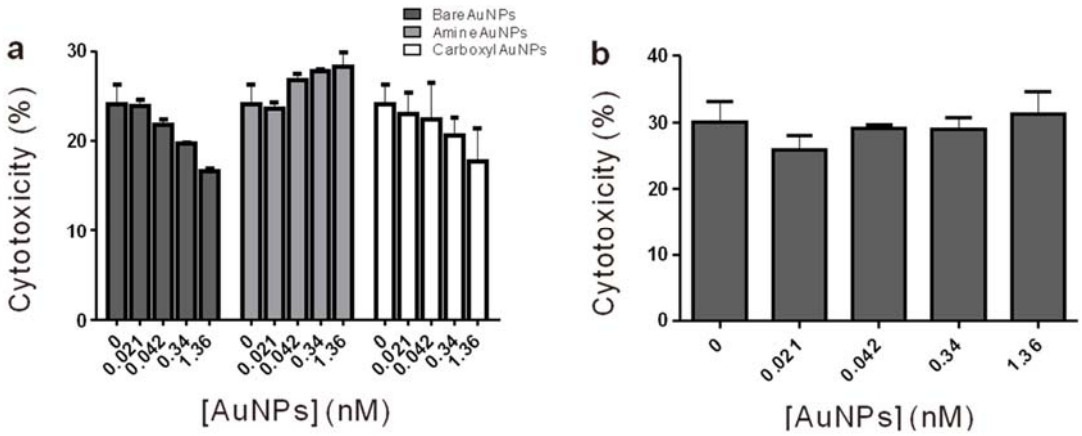

Figure S1. Neurotoxicity of the Aβ species induced with bare, amine-conjugated, and carboxyl-conjugated AuNPs. (performed by Yu-Jen Chang)